LINEARIZATION OF ANALOG PHOTONIC LINKS

by

Fuquan Wang

A dissertation submitted to the Faculty of the University of Delaware in partial fulfillment of the requirements for the degree of Doctor of Philosophy in Electrical and Computer Engineering

Fall 2019

LINEARIZATION OF ANALOG PHOTONIC LINKS

by

Fuquan Wang

Approved: _____
Kenneth E. Barner, Ph.D.
Chair of the Department of Electrical and Computer Engineering

Approved: _____
Levi T. Thompson, Ph.D.
Dean of the College of Engineering

Approved: _____
Douglas J. Doren, Ph.D.
Interim Vice Provost for Graduate & Professional Education
and Dean of the Graduate College

I certify that I have read this dissertation and that in my opinion it meets the academic and professional standard required by the University as a dissertation for the degree of Doctor of Philosophy.

Signed: _____

Dennis W. Prather, Ph.D.
Professor in charge of dissertation

I certify that I have read this dissertation and that in my opinion it meets the academic and professional standard required by the University as a dissertation for the degree of Doctor of Philosophy.

Signed: _____

Tingyi Gu, Ph.D.
Member of dissertation committee

I certify that I have read this dissertation and that in my opinion it meets the academic and professional standard required by the University as a dissertation for the degree of Doctor of Philosophy.

Signed: _____

Shouyuan Shi, Ph.D.
Member of dissertation committee

I certify that I have read this dissertation and that in my opinion it meets the academic and professional standard required by the University as a dissertation for the degree of Doctor of Philosophy.

Signed: _____

Christopher Schuetz, Ph.D.
Member of dissertation committee

ACKNOWLEDGMENTS

First, I would like to show my appreciation to my advisor, Dr. Dennis Prather, for his support and guidance during the last a few years. His challenges, inspirations, and encouragements have enlightened the direction of my research. He has celebrated my every small achievement and helped me to set long-term goals. Under his guidance, I have become a better researcher and, more importantly, a better person.

Secondly, I feel extremely lucky to have worked with Dr. Shouyuan Shi, who is a good friend and mentor to me. I cannot forget the days and nights when we worked together to finish a handful of interesting projects. I cherish the hard work and accomplishments we have achieved. He is an extremely smart and patient person who explains complex concepts in simple words, helps with my paper writing, and more importantly, teaches me his troubleshooting skills on system integration and programming.

I also want to thank all the colleagues who have offered help in my research work. Dr. Peng Yao has helped me with high-power photodetectors and EDFAs, without which none of my research work would be possible. I would also like to thank Dr. Garrett Schneider and Dr. Janusz Murakowski who have helped me to troubleshoot experiments, to review my journal papers and dissertation. Dr. Yifei Zhang has helped me to get started in antenna design and fabrication. Jie Zhang has helped me with many experiments and he is a very interesting guy to work with. I also want to give special thanks to Dr. Andrew Mercante and Kaitlyn Lawrence who have put great efforts to review my dissertation. Additionally, I would like to thank all the graduate students and

researchers in Dr. Prather's group. It has been a great pleasure and honor for me to be here working, learning, and growing.

Finally, I would like to thank my parents, Yonglin Wang and Shengxiu Chen, who are always patient and supportive of my decision to pursue a doctoral degree. Last but not the least, I would like to express my deep love and gratitude to my wife, Hongxia Ma, who has been very cheerful and encouraging in the past six years. Overall, I am very happy and satisfied with my study and research experience at UD which has been the most wonderful part of my life so far.

Portions of Chapter 2 appear in "Photonic Generation of High Fidelity RF Sources for Mobile Communications" published in Journal of Lightwave Technology, vol. 35, no. 18, pp. 3901-3908, 15 Sept.15, 2017. The author would like to acknowledge the insight and guidance from Dr. Shouyuan Shi, and the funding and technical support from Futurewei. The author of this dissertation is the primary author of this work.

Portions of Chapter 3 appear in "LTE Signal Transmission Over a Linearized Analog Photonic Link with High Fidelity" published in IEEE Photonics Journal, in press, 2019. The author would like to thank Dr. Dennis Prather and Dr. Shouyuan Shi for guidance on the design of experiments and the efforts to publish the work. The author of this dissertation is the primary author of this work.

TABLE OF CONTENTS

LIST OF TABLES

LIST OF FIGURES

ABSTRACT

Analog photonic links are of great importance in future high data-rate telecommunications. However, their performance has been limited by the nonlinearities arising from the link components, such as lasers, optical fibers, modulators, optical amplifiers, and photodetectors. In this dissertation, the nonlinearities of these components, and corresponding linearization techniques are discussed and investigated.

First, an arcsine-predistortion technique is used in a dual-electrode Mach-Zehnder modulator (DE-MZM) to demonstrate a link with suppressed third-order intermodulation distortion (IMD3). As examples, telecommunications industry standard 5 MHz and 20 MHz Long-term Evolution (LTE) signals are digitally predistorted and delivered by the DE-MZM link. The recovered radio frequency (RF) signal on the photodetector maintains high fidelity compared to the original signal, as quantified in terms of adjacent channel leakage ratio (ACLR). Later, this arcsine-predistortion technique is implemented in a photonic transceiver based on tunable optical paired sources (TOPS) and single sideband (SSB) modulation. LTE signals are recovered with high fidelity at a carrier frequency up to 17 GHz.

Besides digital predistortion, optically coherent and incoherent modulator linearization techniques are also investigated. Two optically incoherent modulator linearization techniques are proposed: dual-wavelength linearization and dual-polarization linearization.

In the dual-wavelength linearization approach, two lasers are used to drive two parallel MZMs. A primary MZM is used to deliver data while a secondary MZM is used

to cancel the IMD3 generated by the primary MZM. The overall IMD3 can be fully suppressed by tuning RF/optical power ratio and maintaining 180-degree phase between the two parallel MZMs. LTE signals of various bandwidths are delivered using this link. Compared to a conventional single-MZM link, ACLR is improved by 9-19 dB in this linearized link for LTE signals with 10-97 MHz bandwidth at the cost of 2 dB power penalty.

In the dual-polarization approach, a single laser is used to drive two parallel MZMs while the two outputs are orthogonally coupled into a polarization-maintaining fiber with the help of a polarization beam combiner (PBC). Similar to the two-wavelength linearization technique, the IMD3 can be fully suppressed by controlling RF/optical power ratio and maintaining 180-degree phase between the two parallel MZMs. Using a standard two-tone test method, the link is characterized in terms of conventional key link performance parameters, namely gain, noise figure, third-order output intercept point (OIP3), and spur-free dynamic range (SFDR), and compared to a conventional photonic link based on intensity-modulation direct-detection (IMDD). Again, LTE signals with 10-97 MHz bandwidth are tested, where 11.8~19.6 dB ACLR improvement is achieved at the cost of 2 dB power penalty. While the performance results are comparable to the dual-wavelength approach, this technology uses only single laser and is thus, easier to implement.

In addition to those modulator linearization techniques, various approaches to measure the photodetector nonlinearity are discussed, including a preferred three-tone test scheme using external modulation. The proposed three-tone system is analyzed and simulated, and the predicted IMD3 levels generated by two-tone mixing and three-tone mixing are compared. A three-tone photodetector nonlinearity measurement setup

capable of measuring OIP3 up to 20 GHz is built and tested. Lastly, the dependence of photodetector OIP3 on photocurrent, frequency, and bias voltage is investigated.

Chapter 1

INTRODUCTION

This chapter reviews the development of analog photonic links and discusses their nonlinear distortions attributed to the laser, modulator, fiber, optical amplifier, and photodetector. In addition, the nonlinearity considerations pertinent to telecommunications (*e.g.*, adjacent channel leakage ratio) are introduced. Lastly, the scope, contributions, and innovations of this dissertation are summarized.

1.1 Analog photonic link

The term ‘photonics’ has become increasingly popular ever since the first laser was constructed by Theodore H. Maiman in 1960. Photonics deals with the generation, manipulation, and detection of photons, and has a wide range of applications in telecommunications, computing, space, and defense, such as radio over fiber [1], light fidelity (Li-Fi) [2], photonic signal processing [3], silicon photonics [4], and photonic phased arrays [5].

Microwave photonics, which deals with wavelengths from one millimeter to one meter, corresponding to frequencies from 300 MHz to 300 GHz, has been researched extensively over the last fifty years [6]. The focus of microwave photonics is the generation, processing, distribution, and detection of microwave RF signals using photonic technologies. Among various applications of microwave photonics, analog photonic links stand out as some of the most important approaches to meeting the high data-rate demands arising in the telecommunications industry.

Analog photonic links are used to deliver an RF signal via optical fibers, which include modulation, processing, distribution, and demodulation of optical signals. A typical analog photonic link is shown in Figure 1.1, where light is generated by a laser, modulated by an RF input signal using an electro-optic modulator, transmitted by optical fibers, (optionally) amplified by an Erbium-doped fiber amplifier (EDFA), and demodulated by a photodetector. The output of the photodetector is usually attached to a transimpedance amplifier to convert the current signal to voltage signal, which can then be used for further (electrical) signal transmission or data recovery.

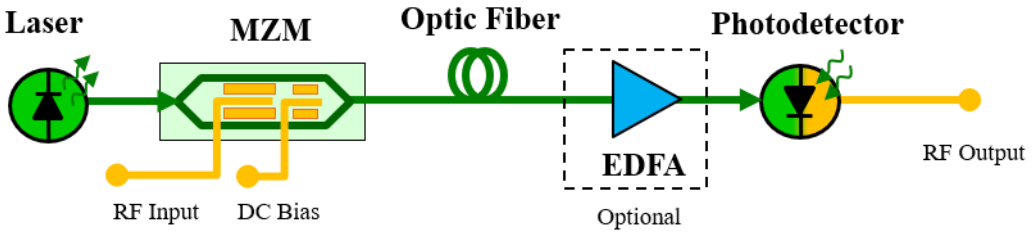

Figure 1.1: A typical analog photonic link using a Mach-Zehnder modulator.

The analog photonic link is an attractive method for the delivery of RF signals from a central location to base stations because optical fibers offer incomparable bandwidth and ultra-low propagation loss. The radio-over-fiber concept was introduced as soon as optical fibers were invented in the 1970s. With the development of the internet and cellular communications, the bandwidth requirement of data transmission has increased dramatically, and optical fibers have thus become one of the best candidates to meet this demand. The data rate of radio-over-fiber links now exceeds 100 Gb/s with the help of multiple-input multiple-output (MIMO) technology [7]–[9].

1.2 Nonlinearity in analog photonic links

Although analog photonic links have advantages such as low loss, reduced cost, and immunity to electronic interference, their nonlinear performance has limited the increase of data rates. Such nonlinear distortions are mainly caused by the modulation and amplification process, i.e., electric-to-optical (EO) modulation in the modulator or laser, optical-to-electric (OE) demodulation in the photodetector, and amplification in the optical amplifier. In addition, nonlinear distortions also arise from the thermal drift of the laser and the dispersion of the fiber. Much work has been done to improve the linearity of those nonlinear components, using spurious free dynamic range (SFDR), third-order intercept point (OIP3), and adjacent channel leakage/power ratio (ACLR/ACPR) as the figures of merit. In the following sections, a brief analysis of nonlinearities from the laser, EO modulator, fiber, EDFA, and photodetector is covered, while a handful of linearization techniques are discussed.

1.2.1 Laser

In analog photonic links, the laser first generates the optical carrier which can be modulated either directly by the laser's current, or externally by an electro-optic modulator. Direct laser modulation is frequently used because of its low cost and system simplicity. However, the transfer function of direct laser modulation is nonlinear and causes signal distortion. In addition, thermal drift in the laser, which leads to power and wavelength drift, adds complexity to its nonlinear behavior. In this section, those nonlinear effects are discussed and summarized.

Of the several types of lasers, such as gas lasers, liquid lasers, and solid-state lasers, semiconductor lasers are the best fit for the analog photonic link. Unlike the other

laser types, semiconductor lasers offer ease of integration, design simplicity, low power consumption, low cost, and tunability.

1.2.1.1 Nonlinearity in directly modulated lasers

Semiconductor lasers offer the ability to directly modulate RF signals into optical signals using the laser's drive current, which has the advantage of lower cost and reduced system complexity compared to an externally modulated link. There are generally four types of semiconductor lasers: Fabry-Perot (FP) laser, Vertical Cavity Surface Emitting Laser (VCSEL), Distributed Feedback (DFB) laser, and Distributed Reflector (DBR) laser. The FP laser is generally used for modulation bandwidth of several gigahertz, the VCSEL is used for a modulation data rate up to tens of Gbps, and DFB lasers are used for long-haul applications with a modulation bandwidth up to about 20 GHz [10]. Recently, modulation bandwidth up to 55 GHz has been reported, which used direct modulation in a short-cavity DBR laser [11].

Although semiconductor lasers have the above-mentioned advantages, their optical output wavelength is affected by temperature. As a result, temperature controllers must be used to maintain the laser junction temperature in order to achieve a stable output. The laser wavelength instability contributes to laser distortion. The laser output power also drifts over a period of time, adding amplitude distortion to the output.

A typical current-to-optical transfer function of a semiconductor laser used in intensity modulation is illustrated in Figure 1.2. In between the threshold and saturation drive currents, there is a linear region. Ideally, it is this region that is used to modulate the RF signal superimposed on a bias current. The bias current should be selected at the middle of the linear region to enable a maximum modulation range. However, the linear region can be distorted by the laser's relaxation resonance, especially in a frequency-

modulated laser [12]. A resonance-like peak of the output power occurs when the laser operates at the relaxation resonance frequency, which also puts a limit on the frequency bandwidth of direct laser modulation. In addition, several other mechanisms can add signal distortions in the linear region, such as spontaneous emission, spatial hole burning, carrier diffusion, spectral hole burning, and nonlinear (two-photon) absorption [13]. The frequency oscillation of the optical carrier causes an undesirable frequency chirp [14], which is not desired in most applications.

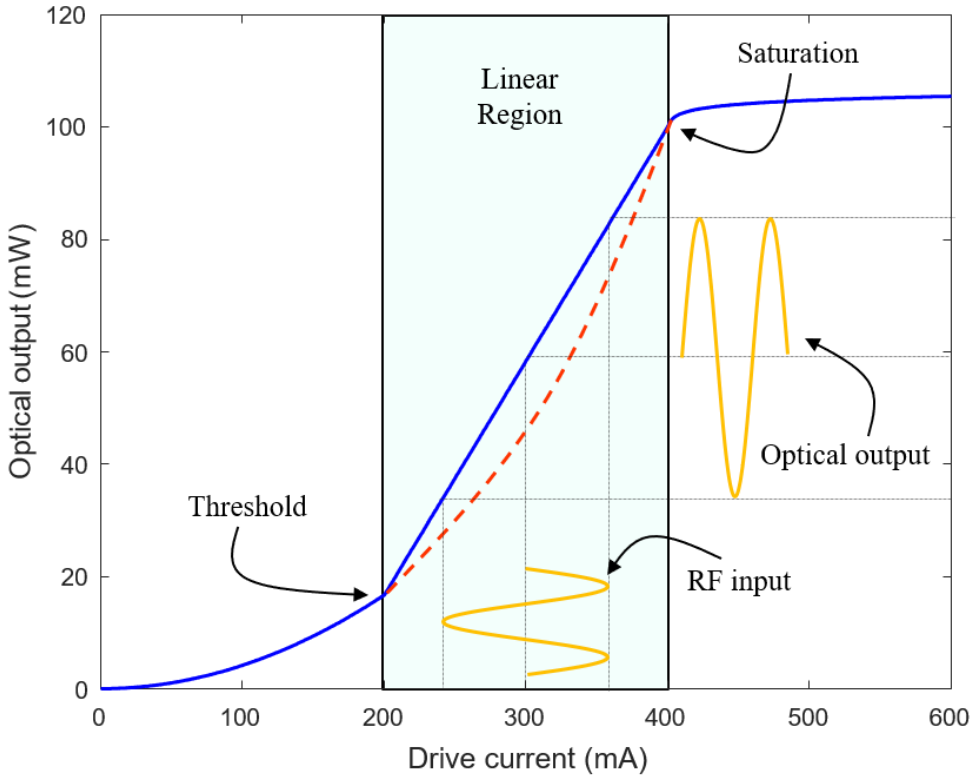

Figure 1.2: Transfer function of a direct-modulated semiconductor lasers using intensity modulation. The blue line represents an ideal linear region while the red dashed curve illustrates the nonlinearities introduced by mechanisms discussed in the text.

1.2.1.2 Thermal drift

It is widely known that the wavelength and output power of a semiconductor laser drift over time, which is mainly caused by the change of junction temperature, *i.e.*, thermal drift. Thermal drift is critical in wavelength sensitive applications, such as dense wavelength division multiplexing (DWDM) or photonic receivers. As wavelength of the laser is determined by temperature at the active layer, various temperature control techniques can be employed to resolve this issue [15]–[20].

In a single-wavelength application, long-term wavelength drift is the main concern. The simplest approach to stabilize the wavelength is to warm up the laser before use over a period of several minutes or hours [21]. However, the warm-up process is very basic and can only stabilize the wavelength for a short period of time, because it is expected that ambient conditions fluctuate and change the equilibrium operating conditions after warm-up. When a stable wavelength is required in long-term applications, the laser wavelength must be adjusted continuously with the help of a feedback control loop, where the junction temperature or output wavelength is monitored. There are two general methods to stabilize the laser wavelength: by tuning the temperature control unit or by adjusting the laser drive current. As shown in Figure 1.3, a thermo-electric cooler (TEC) is used as the temperature control unit, where a thermo-electric device is used as a ‘thermal pump’ to transfer heat from one side to the other. Whenever there is a difference between the measured temperature and set temperature, heat pumping is adjusted. The switching time of TEC-controlled laser is limited to tens of milliseconds because of the large heat resistance at the thermal interface and the heat capacity of the device.

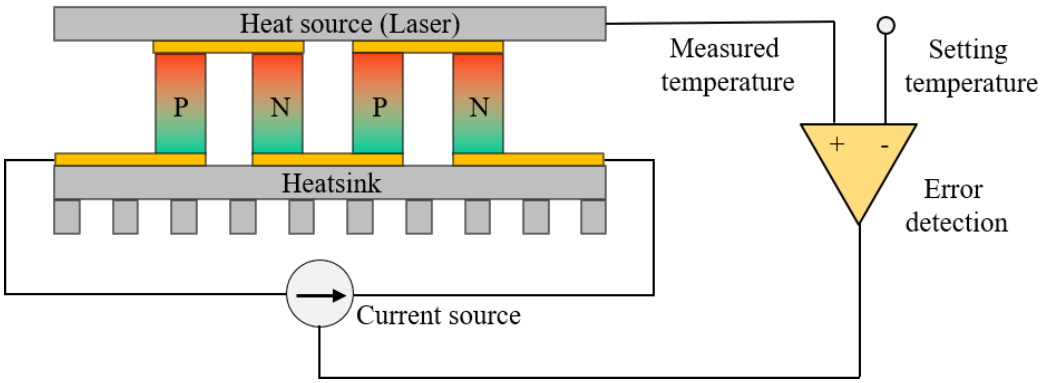

Figure 1.3: A thermo-electric cooler in a feedback control loop used to stabilize junction temperature of the laser.

In multi-wavelength applications such as DWDM, a tunable laser with ultra-fast switching speed is required. A distributed Bragg reflector (DBR) laser is the most promising candidate because of its wide wavelength tunability (>40 nm) and fast tuning speed (a few nanoseconds) [15]. However, there is a wavelength drift caused by the junction temperature change that arises from injection current fluctuations, and this drift can last for serval hundred milliseconds [16]. There are several techniques that can be used, such as two-laser [17] or four-laser [18] source integrated with optical switches, thermal drift compensators on chip [16], [17], [19], or pre-compensatory current injected into the gain medium sections [20].

1.2.2 Electro-optic Modulator

Although direct laser modulation is popular in commercial applications, because of the low cost, it has two disadvantages as compared to external modulation. First, the modulation frequency is limited by the relaxation resonance of the laser. Second, the link gain, which represents the RF power ratio between the link's output and input, is usually less than one and is independent of the laser power. In contrast, the link gain of

an external-modulation link is proportional to the square of input optical power, which allows the external-modulation link to achieve positive link gain, suppress noise figure, and increase the modulation efficiency up to several orders of magnitude above that of a directly modulated link [22]. In addition, external modulation can support much higher frequencies. For example, a thin-film $LiNbO_3$ phase modulators can operate up to 500 GHz [23]. Accordingly, external modulation is a preferred approach in high-frequency applications.

There are two types of electro-optic modulators: phase modulator and intensity modulator. The modulation scheme of a phase modulator is illustrated in Figure 1.4, where two electrodes are used to generate an electric field which is used to modulate the optical signal. A phase modulator can impose a time-dependent phase change on the optical carrier and generate sidebands in the frequency domain. The polarizer helps to maintain the polarization state of the input optical signal in order to minimize the cross-polarization interference. Two such phase modulators can be integrated in parallel to make an MZM, which is the focus of this section. The transfer function, bias condition, and thermal drift of MZM are discussed and summarized below.

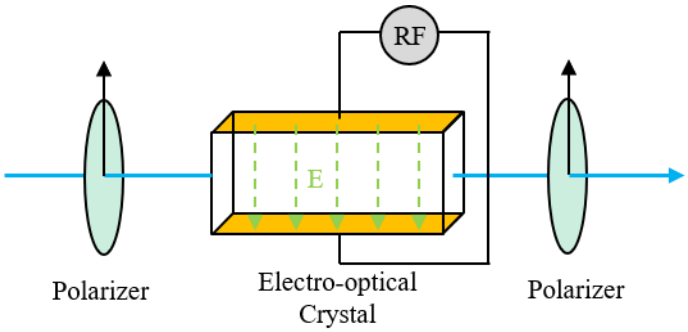

Figure 1.4: Schematic diagram of a phase modulator.

1.2.2.1 Sinusoidal transfer function of MZM

Mach-Zehnder modulator (MZM) has been widely adopted for external modulation where RF signals are up-converted to optical domain. A typical MZM employs a push-pull configuration with two phase modulators arranged in parallel. As shown in Figure 1.5, the input optical beam is divided by a 50/50 splitter and feed to two parallel waveguides. The two beams are modulated by the electric fields between three electrodes, where the top and bottom are the ground electrodes, and the middle electrode is the "hot" electrode to deliver RF/DC signals. The two modulated optical beams are then combined by a 50/50 combiner. As the two optical beams are coherent and have different phases due to applied electric fields, they may combine destructively or constructively, which converts phase modulation in the two arms of the MZM into intensity modulation.

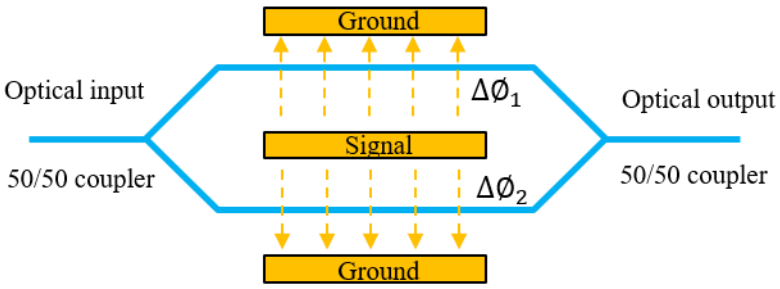

Figure 1.5: Mach-Zehnder modulator in a push-pull configuration.

1.2.2.2 Bias condition of MZM

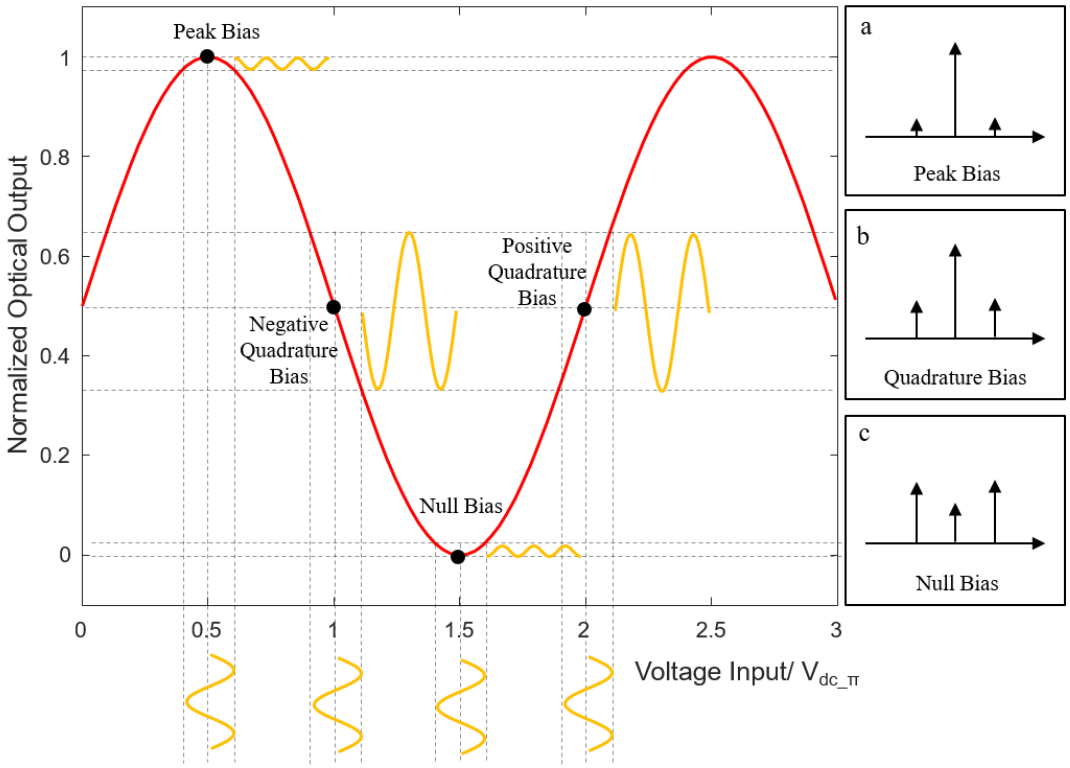

Figure 1.6: Transfer function and different bias conditions of MZM are shown in the left plot. Panels a, b, and c on the right are the optical spectra corresponding to different bias conditions.

The typical transfer function of an MZM is shown in Figure 1.6. At null bias, the MZM has the minimized optical output power but maximized sideband power relative to the carrier, which is preferred in applications where the input RF signal is weak, such as photonic receivers. The benefits of null bias are the low noise figure and high spurious-free dynamic range SFDR [24]. However, second-order nonlinear distortion is strong at null bias, which limits the link's bandwidth to one octave. Also, more optical power is required at the MZM input to generate the same amount of RF

power. As an alternative, null biased MZM can be used with a parallel optical local oscillator to increase the generated RF power.

Quadrature bias with either positive or negative slope is widely used in data modulation because it yields the best modulation linearity with moderate optical power. As shown in Figure 1.6, quadrature bias is at the most linear portion of the sinusoidal transfer function. The other advantage of quadrature bias is the minimized second order distortion, which enables ultra-wideband applications.

The output of MZM is maximized at peak bias. However, the optical sideband power is very weak, and the modulation efficiency is extremely low. As shown in Figure 1.6, data modulation at peak bias has a higher chance of clipping distortion. Furthermore, the high optical power can increase the link noise floor significantly due to higher shot noise and relative intensity noise (RIN). Peak bias is not widely used because most applications require both high linearity and low noise levels.

The relationship between bias voltage and high-order responses of MZM is shown in Figure 1.7. At quadrature bias, the modulation efficiency is highest because the fundamental signal is maximized. In addition, the bandwidth is above one octave because the second order distortion is minimized. However, the third-order distortion is so strong that compensation techniques must be used if wide dynamic range is desired. For peak and null bias, the modulation efficiency is very low because the power of the fundamental response is minimized. The strong second order distortion also limits the bandwidth of the link. As a result, quadrature bias is the most power efficient and broadband configuration in a single MZM photonic link.

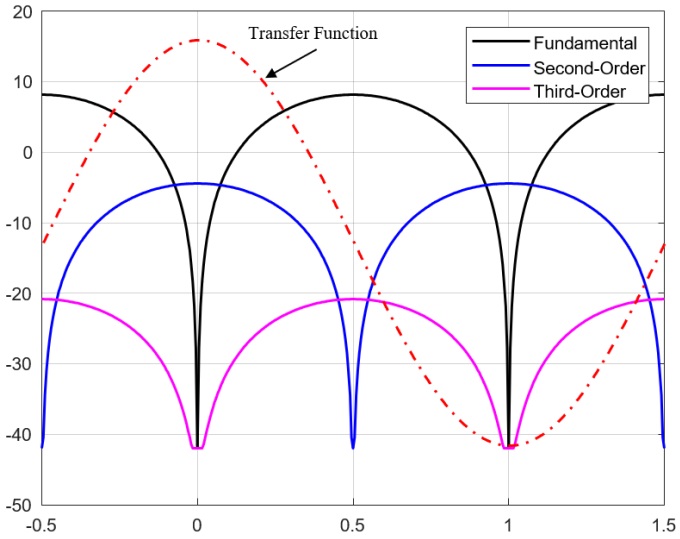

Figure 1.7: Transfer function of MZM, fundamental, second order, and third order response at different bias voltages, this figure is reproduced according to [25], © IEEE.

1.2.2.3 Thermal drift of MZM

The MZM is affected by a serious problem known as thermal drift. As shown in Figure 1.8, there are two types of MZMs using lithium niobate (LN or $LiNbO_3$): x-cut and z-cut MZM. In the x-cut MZM, two optical waveguides are located symmetrically in between the electrodes where a buffer layer is optional. With the buffer layer removed, more of the electrical field can penetrate through the waveguide and enhance electrooptic modulation, resulting in reduced drive voltage. In a z-cut modulator, two optical waveguides are located under the electrodes where the buffer layer provides an improved impedance match.[26] A comparison between z-cut and x-cut LN modulators has been performed using finite element method in [26], and is summarized in Table 1.1.

Table 1.1: Comparison of x-cut and z-cut Mach-Zehnder modulator

	z-cut	x-cut
Bandwidth	High bandwidth	narrow bandwidth
Impedance matching	easy	hard
Chirp	high	low
Buffer layer	Mandatory	optional
Drive Voltage	low	high[26]
Waveguide position	Under electrode	Between electrodes
Activation Energy	1.0 eV [27]	1.2 eV [28]

The x-cut modulator requires higher drive voltage than the z-cut modulator because the electric field needs to penetrate through the buffer layer, whereas the travel distance is smaller in a z-cut modulator. The thermal drift is due to the pyroelectrically induced charge, which can be reduced by adding a silicon coating on the substrate surface.

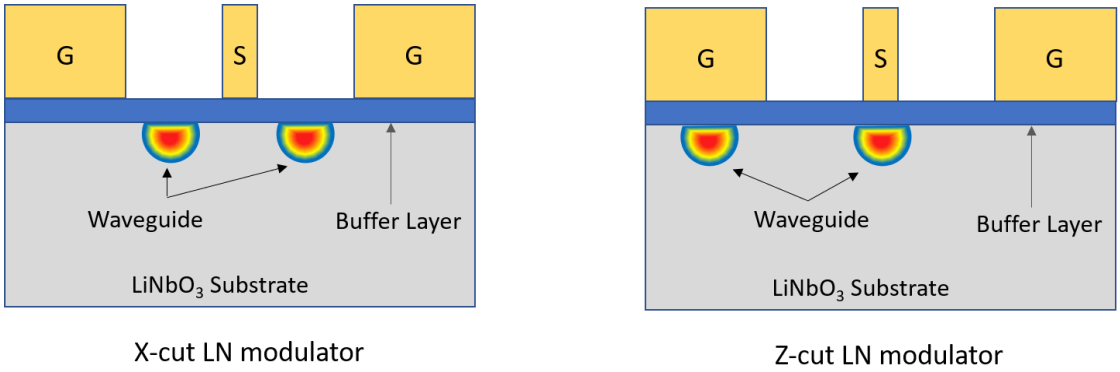

Figure 1.8: Illustration of x-cut and z-cut modulators.

In a Z-cut $LiNbO_3$ modulator, half-wave drive voltage is smaller which enables them to work better for high-speed applications, but they suffer from stronger thermal drift where a silicon coating on the substrate surface can help to mitigate optical

absorption from the metal electrodes. Alternatively, x-cut $LiNbO_3$ modulators have a smaller thermal drift even without a silicon coating [29]. Both x-cut and z-cut $LiNbO_3$ modulators suffer from long-term DC bias drift and usually require external bias control circuitry. According to [28], the thermal drift speed depends on the bias voltage and environment temperature, where a higher voltage or temperature gives a higher drift speed. For example, the DC drift rate is 10^{-5} V/hr at 1 V and 70 ℃, whereas it is 0.1 V/hr at 8 V and 145 ℃.

1.2.3 Optical fiber

Optical fiber has become the dominant method to deliver optical signals because it has ultra-low propagation loss, low cost, and immunity to electromagnetic interference. Over time, the preferred wavelength of optical signals has shifted from 850 nm to 1300 nm, and then to 1550 nm, while single-mode fiber is used more frequently than multimode fiber because of its low chromatic dispersion.

As shown Figure 1.9, there are different types of optical fibers, such as single-mode fiber and multimode fiber. They have the same 125 μm cladding diameter, but the core diameter is quite different. Single mode fiber only supports one mode and is suitable for long-haul applications, whereas multimode fiber is usually used in short distance applications. As most optical components are polarization sensitive, some single mode fibers are designed to maintain the polarization state, which are called polarization-maintaining (PM) fibers. The second row of Figure 1.9 illustrates PM fiber with different shapes of stress rods, such as PANDA fiber, bowtie fiber, and elliptical-clad fiber.

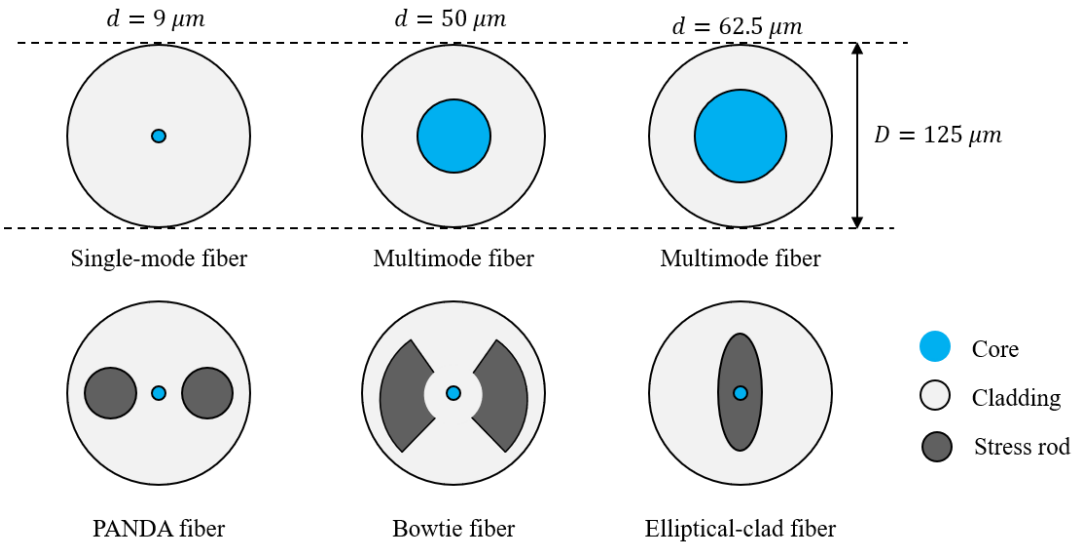

Figure 1.9: Single-mode fiber, multimode fiber, and different types of polarization-maintaining single-mode fiber, depicted in cross-section.

As shown in Figure 1.10, There are four types of dispersion in optical fibers including modal dispersion, chromatic dispersion, waveguide dispersion, and polarization mode dispersion.

Modal dispersion is the major form of distortion in multimode fiber when many different optical modes are supported. As shown Figure 1.10 (a), different optical modes travel in different paths and arrive at the fiber output at different times, which can lead to signal blurring, such as filling-in between peaks or depolarization at the output [30]. With the proper design of the multimode fiber, modal dispersion can be used to compensate chromatic dispersion, which allows for better system performance [31].

Chromatic dispersion is caused by the light of different wavelengths traveling in the optical fiber at different speeds. Although laser sources have very small linewidths, usually a few hundred kilohertz, they are not monochromatic. The chromatic dispersion can be found in both multimode fibers [32] and single-mode fibers [33]. In long-haul

applications, where single-mode fibers are used, chromatic dispersion occurs when the optical signal propagates though tens or even hundreds of kilometers. To overcome chromatic dispersion, external modulation with a dual-electrode MZM can be used to generate single-sideband (SSB) modulation. Using this technique, 10^{-9} bit-error-rate (BER) with 0.5 dB power penalty was achieved in a 80 km single-mode fiber link at 12 GHz [33]. In addition, a modulation-diversity receiver was proposed to compensate for the arbitrary chromatic dispersion generated by amplitude modulation and phase modulation [34].

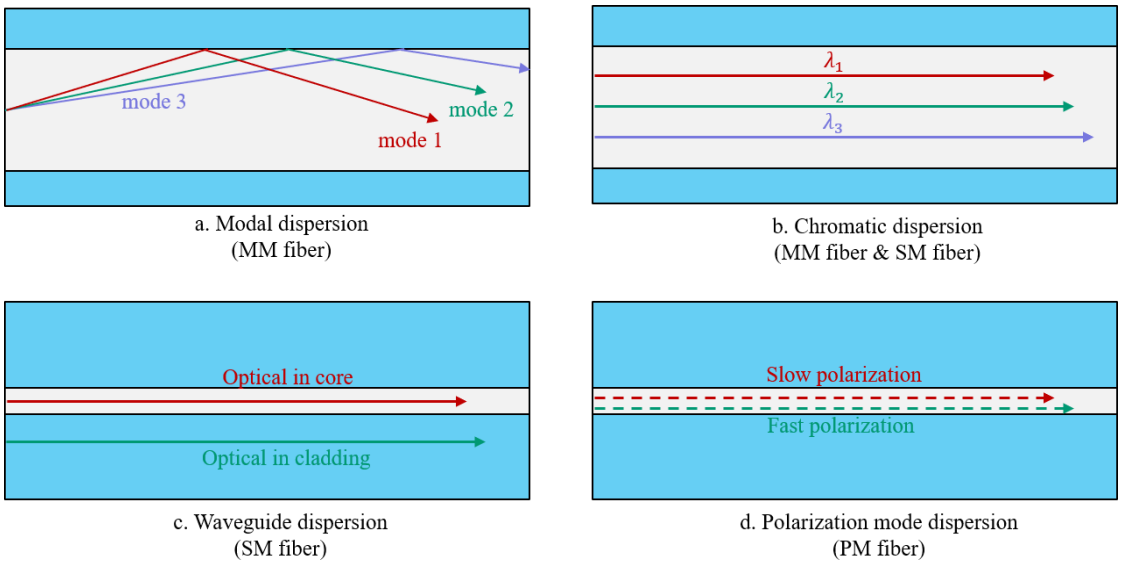

Figure 1.10: Different types of dispersion in optical fiber (MM: multimode, SM: single-mode).

Although most optical power travels in the core, some optical power travels in the cladding material, especially for single-mode fibers. As the refractive index of the cladding material is smaller than the core, the light travels faster in the cladding material

causing waveguide dispersion [35]. In long-haul applications that use single-mode fiber, waveguide dispersion becomes worse and degrades the link performance on top of the chromatic dispersion.

Optical signals can travel separately in two orthogonal polarizations of single-mode fibers. In ideal single-mode fibers, they travel at the same speed. However, there are random imperfections that can limit the ideal circular polarization. Consequently, the orthogonal optical signals propagate at different speeds and cause polarization dispersion, which can lead to spread and overlap of the input signals. These polarization cross-coupling effects are summarized in [36], where different types of polarization maintaining fibers are proposed, such as Elliptical-clad fiber [37], PANDA fiber [38], and Bowtie fiber [39], which are illustrated in Figure 1.9.

1.2.4 EDFA

Although the loss of optical fibers is trivial over short distances, it becomes significant after tens-of-kilometers propagation. Then, optical amplifiers must be used, such as semiconductor amplifiers, fiber Raman amplifiers, and doped fiber amplifiers. An erbium-doped fiber amplifier (EDFA) is the most widely used optical amplifier mainly because of its useful gain bandwidth (around 1.5 μm), low intrinsic noise, and high pumping efficiency [40].

However, an EDFA also introduces unwanted distortion to the link, such as increased noise floor from amplified spontaneous emission (ASE) or the nonlinear amplification on different wavelengths due to gain tilt. The gain tilt of EDFAs can be defined as the slope of the linear fit to the dependence of gain on wavelength, where the unit is dB/nm. When gain-tilt EDFAs are used in wavelength-division multiplexing, different wavelengths receive different gains, which can introduce distortions and lead

to the degradation of signal-to-noise ratio (SNR). Research has been conducted to model the EDFA [41] and analyze the distortion due to gain tilt [42]–[44], where the composite second-order (CSO) distortion from an EDFA is experimentally and theoretically analyzed. For example, when a chirped optical signal with frequency modulation goes through the EDFA, unwanted amplitude modulation occurs because of gain tilt. Numerous approaches have been investigated to compensate the gain tilt, such as optical gain control using a saturable absorber [45], optical fibers designed with inherent filtering capabilities [46], tunable Mach-Zehnder filter [47], and $LiNbO_3$ polarization transformer [48]. With those techniques, the gain error can be reduced from 1.3 dB to 0.4 dB in [45], the gain variation can be maintained less than 1 dB over 50 nm [46], and the maximum gain ripple value can be as low as 0.36 dB [48].

1.2.5 Photodetector

The optical-to-electrical conversion is completed at the photodetector, which is a nonlinear device as well. According to [49], the first harmonic distortion measurement on photodetectors was reported in 1976 [50], where the second order distortions of an avalanche photodetector, reach-through avalanche photodetector, and p-i-n photodetector were measured at 6 MHz. The measured nonlinear distortion was very small at low frequencies, and therefore it was not a big concern. Two high-speed rear-illuminated InGaAs/InP photodetector were measured in 1990 at a few GHz [51], where substantial high-order harmonics were monitored up to the 40^{th} order. The nonlinearity of photodetectors has become an important problem with the fast development of high-power high-speed photodetectors.

With the development of analog photonic links, high-power high-speed photodetectors are developed where the chip size is greatly reduced. This causes space-

charge effects, such as carrier velocity reduction, depletion capacitance increase, and carrier collection time increase. Those effects are power-dependent and can contribute nonlinearities to the photodetector output. To understand the nonlinear behavior of photodetectors, an equivalent circuit model to calculate harmonics of a p-i-n photodetector is proposed in [52], where an RC circuit is used. There are other factors that contribute to the photodetector nonlinearities, such as the carrier recombination nonlinearity at high photocurrent [53] or bias voltage-dependent responsivity [54]. The mechanisms of photodetector nonlinearity are very complicated and most research works are based on empirical models.

While the reason behind the photodetector nonlinearities is hard to investigate, the nonlinear behaviors are easy to measure. Although there are many high-order distortions, the second and third order distortion are the most important. They can be measured using a two-tone or three-tone method, where the second-order intercept point (OIP2) and the third-order intercept point (OIP3) are used as the figure of merit. As shown in Figure 1.11, OIP2 is the output power point where the fundamental and second-order lines intercept, whereas OIP3 is the output power point where the fundamental and third-order lines intercept. Efforts have been made to develop high-power high-speed photodetectors with high linearities, such as the uni-traveling-carrier photodetector with an OIP3 of 35 dBm at 20 GHz [55], the modified uni-traveling-carrier photodetector with an OIP3 of 36 dBm at 20 GHz [56], or the partially depleted absorber photodetectors with an OIP3 of 39 dBm at 20 GHz [57].

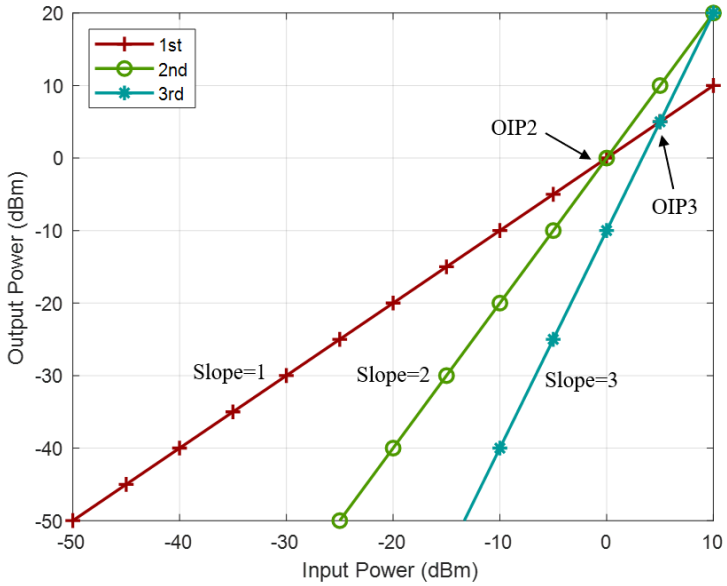

Figure 1.11: Illustration of OIP2 and OIP3.

In addition, approaches to suppress the nonlinearity of a photodetector are also proposed, such as the balanced photodetector to suppress the even-order nonlinearities, where four photodetectors [58] or two photodetectors [59], [60] are used or cryogenic temperature operation wherein the amplitude-to-phase conversion nonlinearity is reduced by up to 10 dB [61].

1.3 Nonlinearity consideration in telecommunications

The nonlinearity of an analog photonic link can be characterized in a traditional way using link gain, noise figure, and SFDR or it can be characterized from the perspective of telecommunications, where the data rate can be increased by using different types of multiplexing techniques, such as frequency division multiplexing (FDM), time division multiplexing (TDM), wavelength division multiplexing (WDM), and spatial division multiplexing (SDM). In the case of FDM, the RF spectrum is

divided into many channels where each channel is occupied by a user. The nonlinear distortion can cause spectrum regrowth, which enables distortion to penetrate through adjacent channels. The power leakage into adjacent channels can interfere with the transmissions in the neighboring channels and impair system performance. According to the conformance testing standard of Long-Term Evolution (LTE) base stations [62], one can use adjacent channel leakage ratio (ACLR) as the figure of merit to evaluate the link's linear performance.

As illustrated in Figure 1.12, there are five adjacent channels, where the frequency offset is 20 MHz. In order to calculate the ACLR, the total power of each channel needs to be calculated using a band pass filter that has a bandwidth equal to 90% of the channel offset, i.e., 18 MHz is used in Figure 1.12. The amplitude of each channel is illustrated in Figure 1.12 as yellow bars. The ACLR can be calculated by dividing the center channel power with the adjacent channel power, and then convert it to decibel scale. According to the requirement listed in [62], the ACLR needs to be maintained higher than 44.2 dB, or lower than -44.2 dBc, which has the same meaning but in a different format.

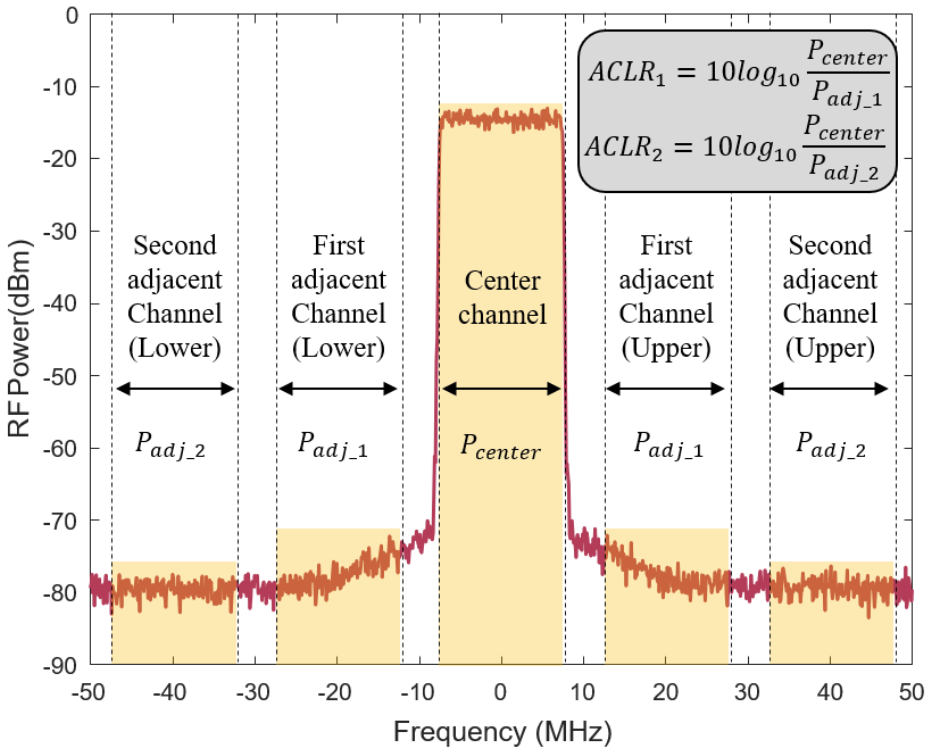

Figure 1.12: An example of adjacent channel leakage ratio.

1.4 Scope of Dissertation

This work can be divided into two parts. The first part focuses on linearization techniques for MZMs. The second part focuses on the characterization and modeling of high-power photodetectors. Accordingly, the dissertation is organized as follows:

Chapter 2 proposes a digital predistortion technique based on arcsine function to compensate for the sinusoidal transfer function of MZMs. This linearization technique is verified in a DE-MZM link by transmitting high-fidelity 5 MHz and 20 MHz LTE signals. The digital linearization is then used in another DE-MZM link where SSB modulation and tunable optical paired sources (TOPS) are used. Similarly, high fidelity quadrature amplitude modulation (QAM) signal transmission is demonstrated.

Chapter 3 compares optically coherent and incoherent MZM linearization techniques. An optically incoherent MZM linearization using two wavelengths is proposed. After theoretical analysis and simulation, an experiment is conducted using LTE signals of various bandwidth generated using the link, where significant ACLR improvement is achieved.

Chapter 4 proposes another optically incoherent MZM linearization technique, where two orthogonal polarizations are used. As only one laser is required, this approach reduces system complexity and cost. Link parameters such as gain, noise figure, OIP3, and SFDR are tested using a two-tone method. Then LTE signals are generated using this linearized link, where similar ACLR improved is maintained as to the two-wavelength approach.

Chapter 5 focuses on the measurement of photodetector nonlinearity where two-tone and three-tone method are compared. A three-tone system is analyzed, simulated, integrated and tested. The dependence of photodetector OIP3 on the frequency, photocurrent and bias voltage is measured and discussed.

Lastly, Chapter 6 summarizes the contributions of this dissertation and points to future research opportunities.

1.5 Contribution and Innovation

Three different types of MZM linearization techniques are proposed, analyzed, and validated. Using those techniques, LTE signals or QAM signals are generated with ultra-high fidelity where significant ACLR improvement is found. Those techniques are useful to implement analog photonic link in telecommunication without significant data degradation.

The first MZM linearization technique is arcsine digital predistortion, where the predistortion is implemented in digital domain before the analog waveform is generated. The nonlinearity of MZM is compensated by changing the waveform. This technique is adopted in a DE-MZM link where one MZM is used to generate linearized data, whereas the other MZM is used to generate a tunable optical carrier. In this link, the carrier-to-sideband ratio (CSR) can be used to optimize the nonlinearity attributed to the high-power photodetector. In addition, this technique is used in a DE-MZM link where SSB modulation and TOPS are used. High-fidelity QAM signals are delivered by the link up to 17 GHz.

The second MZM linearization technique is a two-wavelength MZM linearization technique, which is based on optically incoherent combination. With proper RF/optical power ratio and 180-degree phase difference, the IMD3 generated by primary MZM can be fully cancelled by the secondary MZM. LTE signals with bandwidth from 10 MHz to 97 MHz are tested, and 9-19 dB ACLR improvement is achieved.

The third MZM linearization technique is a two-polarization MZM linearization technique, where a polarization beam combiner is used. Similar to the two-wavelength approach, significant ACLR improvement can be achieved if RF/optical power ratio and the 180-degree phase difference are maintained. Using this approach, the SFDR of the link is improved by about 17 dB at the cost of 1.1~1.7 dB gain penalty.

Besides the MZM linearization techniques, a three-tone photodetector nonlinearity test system is analyzed, simulated, integrated, and tested. The nonlinear performance of the MUTC photodetectors is characterized using OIP3. Lastly, the

dependence of OIP3 on frequency, bias voltage, and photocurrent are measured and analyzed.

Peer Reviewed Journal Publications:

1. **F. Wang**, S. Shi, G. J. Schneider, P. Yao, C. Schuetz, J. Murakowski, X. Qi, M. Kermalli, X. Liu, and D. W. Prather, "Photonic Generation of High Fidelity RF Sources for Mobile Communications," in Journal of Lightwave Technology, vol. 35, no. 18, pp. 3901-3908, 15 Sept.15, 2017.
2. **F. Wang**, S. Shi, D. W. Prather, "LTE Signal Transmission Over a Linearized Analog Photonic Link with High Fidelity," IEEE Photonics Journal (in press), 2019.
3. **F. Wang**, S. Shi, D. W. Prather, "Microwave Photonic Link with Improved Linearity Using Parallel MZMs and Polarization Beam Combiner," submitted to Journal of Lightwave Technology.
4. Y. Zhang, **F. Wang**, S. Shi, R. D. Martin, P. Yao and D. W. Prather, "Ultra-Wideband Microstrip Line-to-Microstrip Line Transition in Multilayer LCP Substrate at Millimeter-Wave Frequencies," in IEEE Microwave and Wireless Components Letters, vol. 27, no. 10, pp. 873-875, Oct. 2017.
5. Y. Zhang, S. Shi, R. D. Martin, P. Yao, **F. Wang** and D. W. Prather, "Ultra-Wideband Vialess Microstrip Line-to-Stripline Transition in Multilayer LCP Substrate for E- and W- Band Applications," in IEEE Microwave and Wireless Components Letters, vol. 27, no. 12, pp. 1101-1103, Dec. 2017.
6. D. W. Prather, S. Shi, G. J. Schneider, P. Yao, C. Schuetz, J. Murakowski, J. C. Deroba, **F. Wang**, M. R. Konkol, and D. D. Ross, "Optically Upconverted, Spatially Coherent Phased-Array-Antenna Feed Networks for Beam-Space MIMO in 5G Cellular Communications," in IEEE Transactions on Antennas and Propagation, vol. 65, no. 12, pp. 6432-6443, Dec. 2017.

Chapter 2

DIGITAL PREDISTORTION OF MZM

As discussed in the previous chapter, electro-optic modulators have an intrinsically nonlinear transfer function that must be compensated to support high-fidelity data modulation. In this chapter, principles and applications of digital predistortion are discussed, while the implementation of digital predistortion techniques on analog photonic links is analyzed, simulated, and tested. Lastly, this digital predistortion technique is used in a photonic transmitter that can work up to 17 GHz.

2.1 Introduction

Although there are numerous techniques to linearize analog photonic links, digital predistortion is still one of the most popular approaches. The main advantages of digital predistortion are low cost and simplicity, where no change is required to the optical components.

Before digital predistortion was used in analog photonic links, it was used in RF high-power amplifiers (HPAs) dating back to 1980 [63]. Behavior models of HPAs are usually estimated first based on their amplitude-modulation-to-amplitude-modulation (AM-AM) and amplitude-modulation-to-phase-modulation (AM-PM) curves [64], where the gain is represented by a complex polynomial function of the input power [65]. There are two concerns in HPA digital predistortion design. First, the transfer function changes because of variations of both the input signal and environment temperature. Second, the memory effect from HPAs changes the transfer function as well. To resolve

those problems, many predistortion approaches have been developed, such as real-time estimation and adaptive predistortion [65], predistortion with memory [66]–[68], and predistortion using direct learning algorithms [69]. In those applications, the third-order distortion as measured by the adjacent channel power ratio (ACPR) can be improved by 8-15 dB.

Table 2.1: Comparison of different applications using digital predistortion techniques. CATV: Cable television, EAM: electro-absorption modulator, CTB: composite-triple-beat, Ka band:26.5-40 GHz, X band:8-12 GHz, C/I: carrier-to-intermodulation ratio, EML: electro-absorption modulated laser, OMI: optical modulation index.

Year	Author	Application	Object	Frequency	Performance	Ref
1984	Bertelsmeier	Optical transmission	Laser	300 MHz	15 dB IMD2 reduction	[70]
1997	G.C. Wilson	CATV	EAM	50-550 MHz	22.6 dB CTB reduction	[71]
2000	V. Magoon	External modulated Link	MZM	1.3 GHz	24 dB IMD3 suppression	[72]
2003	A. Katz	General purpose	MZM	Ku band X band	15 dB C/I improvement	[73]
2003	L. Roselli	Cellular	Laser	Cellular band	8-10 dB IMD3 suppression	[74]
2006	V.j. Urick	Long-haul analog fiber link	MZM	6-12 GHz	6dB SFDR improvement	[75]
2010	Yiming Shen	Multiband OFDM	EAM	3.1-4.8 GHz	7 dB IMD3 suppression	[76]
2013	Yuan Bao	OFDM transmitters	EML MZM	6-12 GHz	7-16.5% OMI improvement	[77]

Various digital predistortion approaches used in the linearization of analog photonic links are summarized in Table 2.1, where the linearization object, operation frequency, and performance improvement are compared. The first digital predistortion

in an analog photonic link was applied to a direct-modulated laser in 1984, where the second-order distortion was reduced by 15 dB at frequencies up to 300 MHz [70]. Digital predistortion techniques were then used on both Mach-Zehnder modulators (MZMs) and electro-absorption modulators (EAMs) to compensate their nonlinear transfer functions. According to Table 2.1, the second-order or the third-order distortion has been improved by 7-24 dB using these techniques.

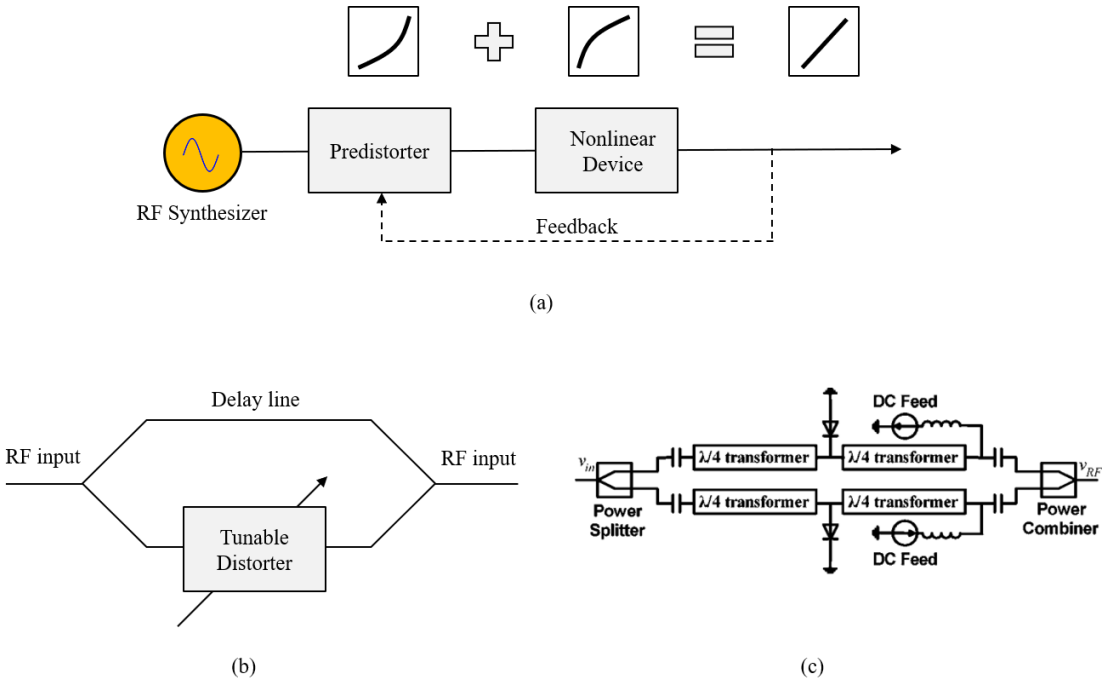

Figure 2.1: a) A typical process of digital predistortion techniques, b) a common configuration using digital predistorter designs, c) a novel digital predistorter design for EAM [76], © 2010 IEEE.

Although the transfer functions of MZM, EAM, and laser are different, the digital predistortion process is very similar as depicted in Figure 2.1 (a). Usually the nonlinear transfer function is measured first and then a compensating circuit is designed

to cancel the distortion. Furthermore, the second-order or the third-order distortion can be filtered, monitored, and used as additional criteria to tune the distorter. Notably, a real-time adaptive control on the predistorter may be required to minimize distortions since the nonlinear transfer function may drift over time or with temperature. For example, in order to compensate the bias drift of MZMs, a low-frequency pilot tone can be used to monitor the even-order harmonics [72]. When a feedback loop is used, a computer [78] or a digital signal processor [72] is needed to control the predistorter continuously.

A typical configuration of predistortion circuits is given in Figure 2.1 (b). The input RF signals split and travel in two paths, where the majority of signals passes through a delay line undistorted while a small portion of signals is coupled into a path with odd-order distorter [71], which is labeled in Fig 2.1 (b) as a tunable distorter. The RF signals are then combined as predistorted signals to feed optical nonlinear devices where the distortions of the optical devices are cancelled. In addition, another type of predistorter is shown in Figure 2.1 (c), where a reflective diode pair is used for the linearization of EAMs [76].

All of the digital predistortion techniques discussed above are applied after the RF signals are generated, where an electrical predistorter is placed before the input of an analog photonic link. However, in some applications, the RF signals are known and can be modified before they are generated. For example, in telecommunications, the central office has the data to be delivered, which can be modified before they are fed to a digital-to-analog converter (DAC). In this case, the digital predistortion is completed computationally as illustrated in Figure 2.2. In this approach, no changes are made to

the optical or electrical components resulting in an ultra-low-cost linearization technique.

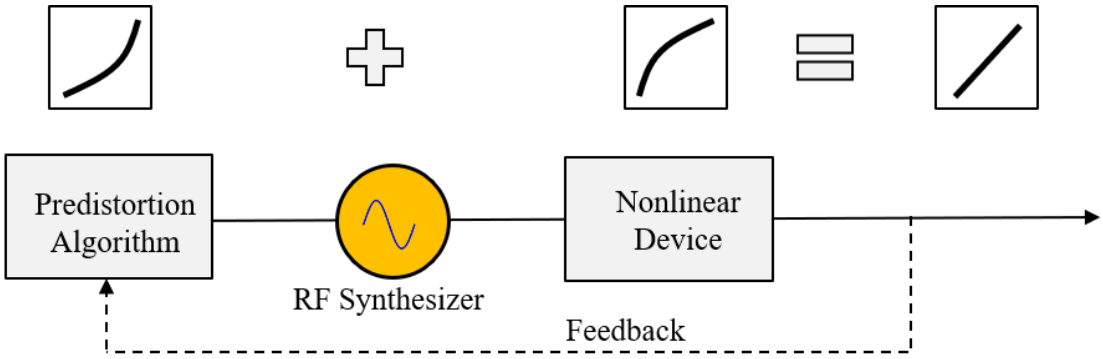

Figure 2.2: The illustration of a digital predistortion technique where the digital predistortion is performed computationally on a signal before the analog signal is generated.

2.2 Digital predistortion on a dual-electrode Mach-Zehnder modulator

In this section, a dual-electrode Mach-Zehnder modulator (DE-MZM) is used to build an analog photonic link that can deliver high-fidelity LTE signals. The DE-MZM has two parallel MZMs, where one MZM is used for data modulation and the other MZM is used to provide optical carrier. The data-modulation MZM is linearized using the digital predistortion approach as shown in Figure 2.2, whereas the carrier-tuning MZM is used as an attenuator to control the carrier-to-sideband ratio (CSR). This linearized link is then characterized in terms of ACLR to evaluate the nonlinearities from the digital-to-analog converters (DACs), RF amplifier, MZMs, EDFAs, and photodetectors (PDs).

The linearized analog photonic link studied herein is constructed with a laser, a DE-MZM, an EDFA, and a PD, as illustrated in Figure 2.3. The DE-MZM is an

integrated modulator on a lithium niobate ($LiNbO_3$) chip, where a splitter, two parallel MZMs, a phase shifter, and an optical coupler are arranged in series. The optical signal is generated by a distributed feedback (DFB) laser, and then splits and feeds the two parallel MZMs, which are driven separately by the RF and DC bias voltages. In this application, the lower MZM is null biased to suppress the carrier and driven by an LTE data signal, while the upper MZM can be arbitrarily biased but no RF input is provided. At the end of the DE-MZM, the lower MZM has two optical sidebands and minimal optical carrier, while the upper MZM has an adjustable-amplitude carrier with no sidebands. With proper phase shifting, the two optical signals are combined and fed to an EDFA. The EDFA is used to amplify the optical signal so sufficient RF power can be generated by the PD to feed the transmit antennas. The advantages in this linearized link include: 1) the MZM nonlinearity can be removed by digital predistortion, 2) the CSR can be tuned either to minimize the PD nonlinearity, or to increase the efficiency.

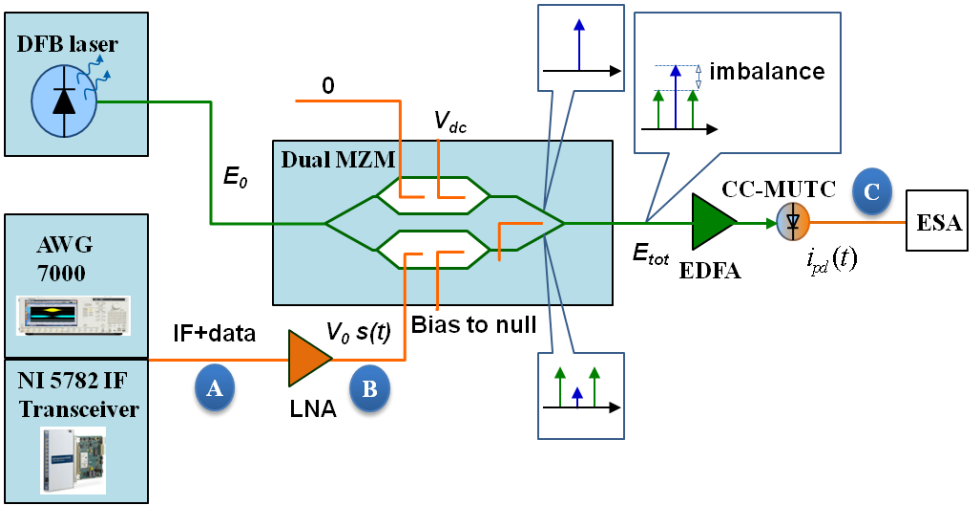

Figure 2.3: Characterization setup based on dual-electrode Mach-Zehnder modulator (MZM) and a charge-compensated modified uni-traveling carrier (CC-MUTC) photodetector. Circled labels A, B, and C indicate various points in the source chain where the signal is analyzed. AWG: arbitrary waveform generator, DFB: distributed feedback, LNA: low noise amplifier, EDFA: Erbium-doped fiber amplifier, ESA: electrical spectrum analyzer.

The electric field E_{tot} at the output of the modulator is given by

$$E_{tot}(t) = \frac{E_0}{\sqrt{2}}\sqrt{L_{MZM}}exp(j\omega_1 t)\left[sin\left(\frac{\pi}{2V_{\pi,dc}}V_{dc}\right) + sin\left(\frac{\pi}{2V_\pi}V_0 s(t)\right)\right] \quad , \quad (2.1)$$

where L_{MZM} is the insertion loss of the MZM, E_0 is the amplitude of the electric field generated by the input optical signal, $V_{\pi,dc}$ and V_π are the voltage values to achieve a π-phase shift in the MZMs for DC and RF, respectively. V_{dc} is the bias voltage at the upper MZM to control the CSR, V_0 is the amplitude of the RF waveform driving the lower MZM, and $s(t)$ is the normalized drive waveform. Equation 2.1 shows the output electrical field that includes two terms: $sin\left(\frac{\pi}{2V_{\pi,dc}}V_{dc}\right)$, which is introduced by the DC bias from the upper MZM, and $sin\left(\frac{\pi}{2V_\pi}V_0 s(t)\right)$, which is generated from the lower

MZM. After the optical signals are amplified by an EDFA and mixed at a photodetector, the corresponding photocurrent can be calculated as follows

$$i_{pd} = \frac{\Re P_0 L_{MZM} g_{EDFA}}{2}\left[sin\left(\frac{\pi}{2V_{\pi,dc}}V_{dc}\right) + sin\left(\frac{\pi}{2V_{\pi}}V_0\, s(t)\right)\right]^2, \quad (2.2)$$

where $\Re$ is the responsivity of the photodetector, g_{EDFA} is the gain of the EDFA, and P_0 is the optical power at the DE-MZM input. With small signal approximation where $V_{dc} << V_{\pi,dc}$, the DC photocurrent can be calculated by

$$i_{dc} = \frac{\Re L_{MZM} g_{EDFA} P_0}{2}\left(\frac{\pi}{2V_{\pi,dc}}V_{dc}\right)^2, \quad (2.3)$$

and the fundamental RF current is

$$i_{rf}(t) = \Re L_{MZM} g_{EDFA} P_0 \left(\frac{\pi}{2V_{\pi,dc}}V_{dc}\right) sin\left(\frac{\pi}{2V_{\pi}}V_0\, s(t)\right) . \quad (2.4)$$

The generated RF current at the photodetector is proportional to both the optical carrier and sideband amplitudes, which are related to the input RF signal. There is also a term that includes $sin^2\left(\frac{\pi}{2V_{\pi}}V_0\, s(t)\right)$, which corresponds to the second-order response of the MZM. As it is far away from the fundamental frequency, it can be suppressed using an RF filter.

To characterize the performance of the link, a time-domain LTE downlink waveform is used as the test signal. The signal has a 5 MHz data bandwidth, 122.88 MHz sampling rate, and an 8-dB peak-to-average power ratio (PAPR). As shown in Figure 2.4, the spectrum is filtered with five adjacent rectangular filters of the same bandwidth, which equals 90% of the signal bandwidth. The frequency offset between two adjacent filters is the same as the signal bandwidth. The ACLR is defined as the ratio of the filtered mean power at the center channel to the filtered mean power at an

adjacent channel. For example, ACLR1 and ACLR2 are the power ratios between the center channel and the first and the second adjacent channels, respectively [79]. Although IMD3 and ACLR are two closely related metrics to characterize device nonlinearities, ACLR is chosen to characterize the link according to 3GPP standards. Analyzed using MATLAB, the spectrum of a 5 MHz LTE signal is shown in Figure 2.4, where the ACLR1 is computed to be -100.3 dBc, and ACLR2 is -104 dBc, respectively.

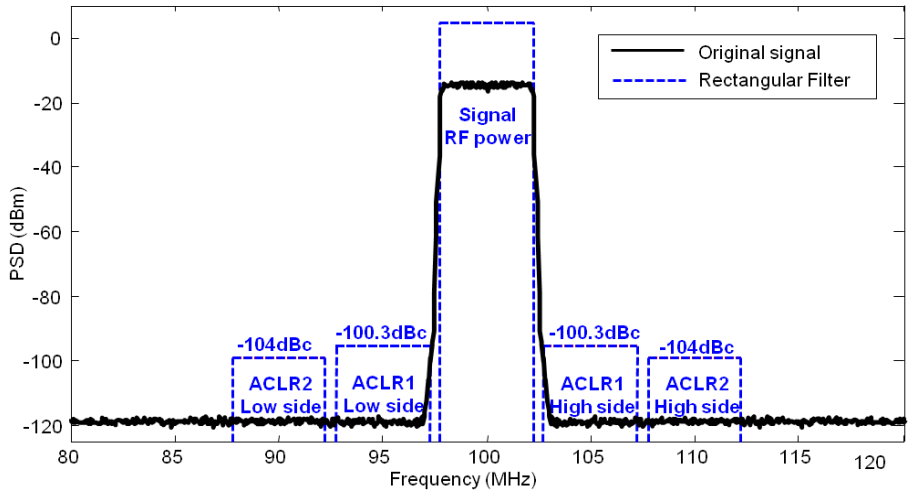

Figure 2.4: Spectrum of a 5 MHz LTE signal with 100-MHz intermediate frequency. Rectangular filters with 4.5 MHz bandwidth are used for ACLR calculation.

To suppress spectral regrowth, the drive signal can be predistorted to pre-compensate for anticipated nonlinearities. Since the transfer function of MZMs is known to be sinusoidal, the waveform can be digitally predistorted using an arcsine function. If the sine function is pre-compensated, the output can be linearized.

To achieve this, the drive voltage (V_{in}) is adjusted via the arcsine function as shown in Figure 2.5. In this case, consider that the output is expected to be at the point L if the response is linear, but the actual output is at the point M due to the modulator's sinusoidal transfer function. To compensate this compression, a higher driving voltage of V_{pred}, as indicated at the point P, is required to obtain a linear response. As a result, the input signal can be predistorted to be V_{pred}, using the arcsine function. Thus, the predistorted signal can be expressed as:

$$V_{Pred} = \frac{2V_\pi}{\pi} arcsin\left(\frac{\pi}{2V_\pi} \cdot V_{in}\right) \ . \tag{2.5}$$

In so doing, we have compensated for the nonlinearities introduced by the MZM, and thereby significantly suppress spectral regrowth. As this technique is based on the inverse transfer function of MZMs, it can be used for different types of input signals. However, this method is limited to the domain of the arcsine function, where the absolute value of $\pi V_{pred}/2V_\pi$ needs to be less than or equal to 1. As a result, the maximum voltage of the RF signal feeding the MZM is $2V_\pi/\pi$. The dark green dashed lines in Figure 2.5 show the upper and the lower limit where the predistortion is valid.

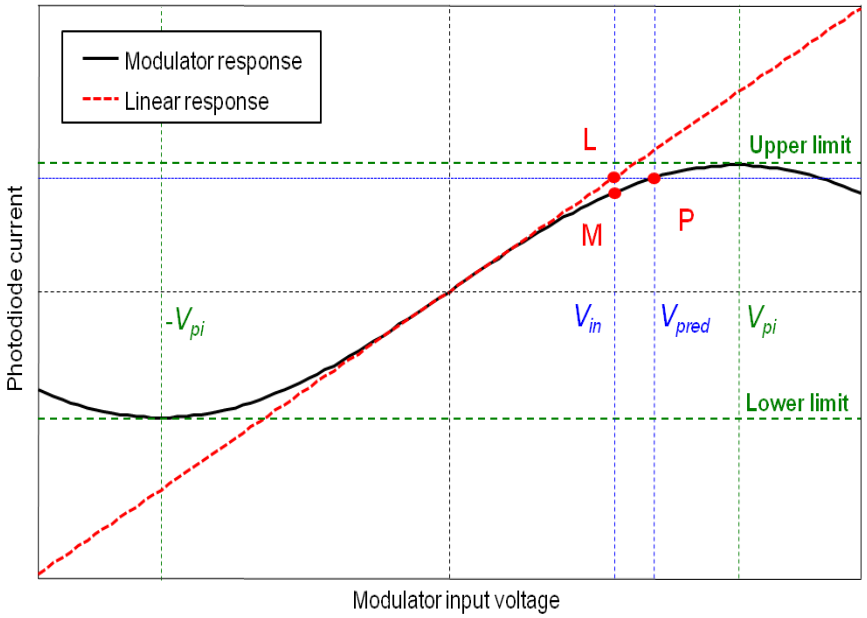

Figure 2.5: Illustration of arcsine digital predistortion on a Mach-Zehnder modulator.

In a transmitting system, high RF output and low out-of-band spurious emissions are required. To achieve the former, a higher drive voltage to the MZM is required, while the latter requires minimizing the nonlinearities that grow rapidly with increasing drive signal. Based on the mathematical model of Equation 2.1-2.5, a simulation has been conducted using MATLAB. As shown in Figure 2.6, a 5 MHz LTE signal is used as the test signal, where the peak-to-peak voltage (V_0) is set to 0.5 V, 1.0 V, and 2.0 V, where the Vπ is 3.5 V. The response is normalized to its peak value for the convenience of comparison. At higher V_0, the spectral regrowth is stronger and the ACLR1 gets worse, indicated in the table inset in Fig. 2.6. However, when the digital predistortion technique is used, the spectral regrowth is removed and the ACLR1 of the undistorted signal (see Fig. 2.6) is fully recovered.

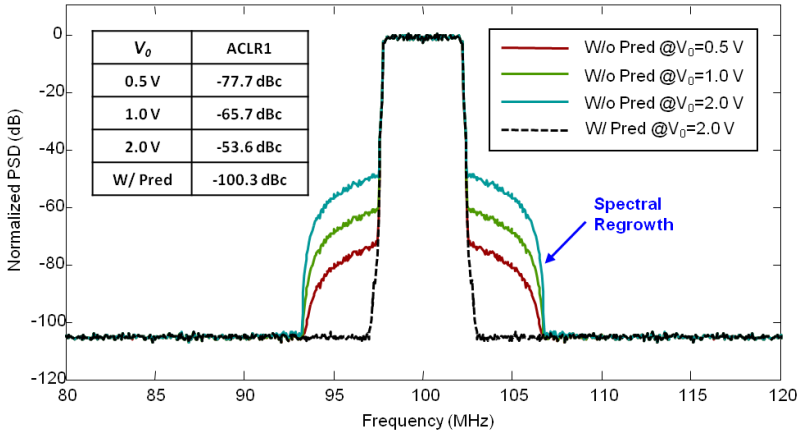

Figure 2.6: LTE signals of different power levels (V_0) show increasing spectral regrowth as characterized by the ACLR1 values shown in the table inset at the upper left. When the same are predistorted with the arcsine function, the recovered signals have no spectral regrowth.

2.3 High fidelity signal transmission on a DE-MZM link with DSB modulation

In this section, signal degradation is minimized using a DE-MZM link with double sideband (DSB) modulation as illustrated in Figure 2.3. An arcsine digital predistortion technique is used to compensate the MZM nonlinearities and the impact of CSR on the link's linearity is studied.

2.3.1 Experiment description

The modulator used in the digital predistortion test is a model LN86S-FC from Thorlabs, which is a dual-parallel, Titanium-Indiffused, and x-cut lithium niobate modulator. This modulator has two MZMs in parallel and can be controlled separately with an external DC bias. It is designed for quadrature modulation such as quadrature phase-shift keying (QPSK, a.k.a. 4QAM) and single-sideband suppressed carrier (SSB-SC) transmission. However, the modulator is used differently for this test, which is illustrated in Figure 2.3.

To characterize the efficacy of this technique, test signals based on an LTE base station standard [79] were used. The available channel bandwidth can be set to 1.4 MHz, 3.0 MHz, 5.0 MHz, 10.0 MHz, 15.0 MHz, and 20 MHz. For convenience, the same LTE waveform analyzed in the previous section, with 5 MHz bandwidth, 122.88 MHz sampling rate, and 1-millisecond duration, is used. To test this link, the waveform is loaded into two signal generators: a Tektronix arbitrary waveform generator (AWG) 7122B and a National Instruments NI-5782 transceiver. The AWG has a maximum sampling rate of 12 Giga-Sample Per Second (GSPS) and a 10-bit digital-to-analog converter (DAC), whereas the NI-5782 has a sampling rate of 500 Mega-Sample Per Second (MSPS) and a 16-bit DAC. For measurement convenience, an intermediate frequency (IF) is introduced according to the operational bandwidth of the RF filters and amplifiers, which are used within the link. The LTE waveforms are processed in MATLAB, where the baseband waveform is mixed with the IF. The IFs of the AWG and the NI-5782 transceiver are set to 1060 MHz and 100 MHz, respectively. Although the LTE waveform is optimized to have an ACLR of around -100 dBc, the actual waveforms generated from the AWG and NI-5782 are degraded due to their limited DAC bit depths and system noise.

To recover the RF signal, a 34-μm InGaAs/InP CC-MUTC photodetector is used to downconvert the optical signal into the requisite RF signal. The photodetector has a responsivity of 0.75 A/W, a 3-dB bandwidth of 17 GHz, and a saturation photocurrent of 100 mA [80]. However, for the measurements, the input illumination is intentionally defocused, thus enabling it to handle more optical power by the virtue of a more uniform illumination over the active area, resulting in a lower responsivity of 0.33 A/W.

When discussing link performance, returning to Figure 2.3, we note the various points that were probed during signal transmission. To begin, we measured the RF signal before and after the low-noise amplifier (LNA) at labels A and B, which considered the data signal delivery, and subsequently, at the data recovery at the photodetector, which is labeled as C.

In the first test, the Tektronix AWG is used as the data source. As shown in Table 2.2, the output waveform from the AWG has an ACLR1 of only -52.7 dBc, which is about 47 dB worse than the theoretical ACLR. The main reason for this degradation is that the DAC in the AWG has only 10-bits resolution. Such low resolution is detrimental in accurately converting a digital data to an analog signal, as the quantization errors from insufficient bit depth can lead to dramatic degradation in the link performance before the signal is fed into the analog photonic link.

To minimize quantization errors and improve ACLR, the DAC bit depth is increased to 16-bit, using a NI-5782 transceiver, which significantly improves the ACLRs compared to the 10-bit AWG. As shown in Table 2.2, the 16-bit DAC offers an ACLR1 of -67.8 dBc, which is ~15 dB better than that from the AWG.

Table 2.2: ACLR measurement at points A and B (see Figure 2.3)

Data Rate (MHz)	Source	A (Output from Source)			B (Output after LNA)		
		Power (dBm)	ACLR1 (dBc)	ACLR2 (dBc)	Power (dBm)	ACLR1 (dBc)	ACLR2 (dBc)
5.0	AWG	-6.1	-52.7	-54.2	4.80	-52.8	-54.1
5.0	NI-5782	-14.1	-67.8	-67.5	0.76	-67.8	-67.7

To this point, we have generated two signals with relatively high ACLR from the waveform generators. The transmitted signal from the source can maintain linearity

with minimal distortion, if the source-signal amplitude is adjusted appropriately, along with proper optical and electronic amplifier gains, and optimal biasing for both modulators and photodetectors.

In this link, the MZM modulation is preferably operated at a high input RF power and a high optical carrier in order to produce a high optical power in the modulated sideband. As a result, the input from the signal generators has to be amplified before being fed into the electro-optic modulator. To preserve signal linearity, an LNA with a high third-order output intercept point (OIP3) is used.

It is well known that the output of RF amplifiers saturates at high input power, an effect referred to as gain compression. Gain compression can be minimized if the amplifier is fed with a low RF input. As the intermediate frequencies of the two test signals are different, two different LNAs are used. For the Tektronix AWG 7000, an LNA with an OIP3 of 36.5 dBm and P1dB of 22 dBm is used. With this LNA inserted, the 5 MHz LTE signal generated by AWG 7000 is tested. The first row in Table 2.2 shows that the measured ACLRs after the LNA at point B is almost identical to the input signal at point A. For the NI-5782 transceiver, an LNA with an OIP3 of 39 dBm is used to boost the RF signal before it feeds the electro-optic modulator. As shown in Table 2.2, the waveform at A and B are in good agreement with each other.

As discussed previously, there is an optimal RF input power to the MZM. First, the power cannot be too high because the arcsine predistortion technique would not be able to compensate for modulator nonlinearity if V_0 is higher than $2V_\pi/\pi$. On the other hand, if the RF input is reduced, the modulated sideband power at the modulator becomes too weak to feed an EDFA, leading to degraded source performance due to increased EDFA ASE noise. The modulator used in this experiment has a V_π of 3.5 V,

hence V_{0_max} is 2.23 V. Thus, an ideal drive voltage should be close to V_{0_max} in order to maximize the optical sidebands, while still being compatible with the digital predistortion.

2.3.2 Digital Predistortion on 5 MHz and 20 MHz LTE signals

To validate the arcsine predistortion technique, a 5 MHz LTE waveform generated by the AWG is used, and ACLR1 and ACLR2 are measured to characterize the efficacy of the predistortion. The measured ACLRs of the LTE signal from the Tektronix AWG, with and without predistortion, are shown in the first row of Table 2.3. The input RF power to the modulator is 4.8 dBm, which corresponds to a peak-to-peak voltage of 2.8 V. Such a high drive voltage supplied to the electro-optic modulator introduces high order nonlinearities. Without the use of predistortion, ACLR degradation is clearly observed at point C, as shown in Table 2.3. In contrast, with the use of predistortion, the recovered signal on the photodetector shows a significant suppression of nonlinearity induced spectral regrowth, with 6 dB improvement in ACLR1. This technique also allows for a larger RF drive signal that produces higher optical sideband power, which is helpful in reducing the amplified spontaneous emission (ASE) noise contribution from the EDFA.

The LTE signal with an intermediate frequency of 100 MHz generated by the NI-5782 transceiver has also been investigated. The recovered data at the photodetector is shown in Table 2.3, which indicates that the ACLR1 is degraded significantly by modulator nonlinearities if digital predistortion is not used. To mitigate the nonlinearities, the arcsine predistortion technique is used. The recovered ACLR1 and ACLR2 are -63.5 dBc and -65.0 dBc, respectively, showing a 9-dB improvement in ACLR compared to those without predistortion.

Table 2.3 ACLR measurement at point C (with and without predistortion).

Data Rate (MHz)	Source	C (Without Predistortion)			C (With Predistortion)		
		Power (dBm)	ACLR1 (dBc)	ACLR2 (dBc)	Power (dBm)	ACLR1 (dBc)	ACLR2 (dBc)
5.0	AWG	12.1	-44.4	-53.2	12.2	-50.3	-53.4
5.0	NI-5782	12.5	-54.2	-65.1	12.6	-63.5	-65.0

In addition to the commercial 5 MHz LTE signal, a 20 MHz LTE signal has also been measured. The 20 MHz LTE signal is generated by AWG and NI-5782 separately with different intermediate frequencies, i.e., 1.06 GHz for AWG and 100 MHz for NI-5782. When the bandwidth of the LTE signal is increased from 5 MHz to 20 MHz, both signal-to-noise ratio (SNR) and ACLR get degraded, where a 7-dB drop in ACLR is observed. As listed in Table 2.4, ACLR1 only drops about 3-4 dB from B to C, which is contributed from the linearized DE-MZM link. From the measured data, we observe that the increased signal bandwidth does not introduce additional ACLR degradation in optical processing.

Table 2.4 ACLR measurement of 20 MHz LTE signal.

Data Rate (MHz)	Source	B (Output after LNA)			C (With Predistortion)		
		Power (dBm)	ACLR1 (dBc)	ACLR2 (dBc)	Power (dBm)	ACLR1 (dBc)	ACLR2 (dBc)
20.0	AWG	4.80	-53.3	-55.2	13.0	-50.3	-51.9
20.0	NI-5782	0.04	-60.4	-61.0	10.59	-56.5	-56.7

2.3.3 ALCR dependence on carrier to sideband ratio

Besides the nonlinearities attributed to the RF LNA and the MZM, the remaining components in the link, such as an EDFA and a high-power photodetector, can also contribute to the degradation of ACLRs. In the proposed DE-MZM link, the EDFA has

a minimum optical input requirement at -10 dBm and the output from the DE-MZM is around -8 dBm, which is close to the boundary value where the signal fidelity can be harmed. Without sufficient optical input power, the spontaneous emission is amplified, thus generating a higher noise floor in the recovered data at the photodetector. To increase the output power of the MZMs, the MZMs can be over driven and compensated according the aforementioned arcsine predistortion technique.

The photodetector can also introduce nonlinearities, depending on the biasing condition, input optical power, and the CSR. These parameters are extensively investigated in this work. To characterize the carrier to sideband ratio (CSR) effect on the ACLR, the incident optical power onto the CC-MUTC photodetector has been increased from 60 mW to 180 mW, which produced increased RF output powers accordingly. In these tests, the CSR is tuned from 6 to 16 dB, the photocurrent varies from 20 to 60 mA using a photodetector with a responsivity of 0.33 A/W.

The generated RF power as a function of input optical power, or generated photocurrent, is shown in Figure 2.7 (a), for several different levels of CSR. As the input optical power increases, the RF power generated on the photodetector also increases with the DC photodetector current. However, a decrease in generated RF power is observed with increasing CSR. In this case, the CSR has an impact on the recovered RF power mainly due to the mixing mechanism on the photodetector.

When both the upper and lower sidebands are mixed with the carrier, they produce output at the same RF frequency, thus doubling the electric field in the optical carrier compared with that of the sideband is shown to generate the maximum RF output. This corresponds to an CSR of 6 dB in power between the optical carrier and

the sidebands. Increasing the CSR for a fixed input optical power is found to reduce the RF output power.

Limited by the OIP3 of the CC-MUTC photodetector, the linearity degrades as the photodetector current increases. The measured ACLR1 and ACLR2 are shown in Figure 2.7 (b) and (c), respectively. As illustrated in the figure, both ACLR1 and ACLR2 degrade as the photodetector current increases. For a constant input optical power or a constant DC photocurrent, a higher CSR reduces the generated RF power. However, a smaller RF photocurrent at a fixed DC photocurrent helps to improve the linearity. Hence, the larger the CSR, the better the ACLRs; however, it also yields lower RF output power. To maintain good ACLR performance, the RF photodetector current should be as low as possible, while the CSR should be as high as possible; however, the requirements for maximum RF power generation are just the opposite.

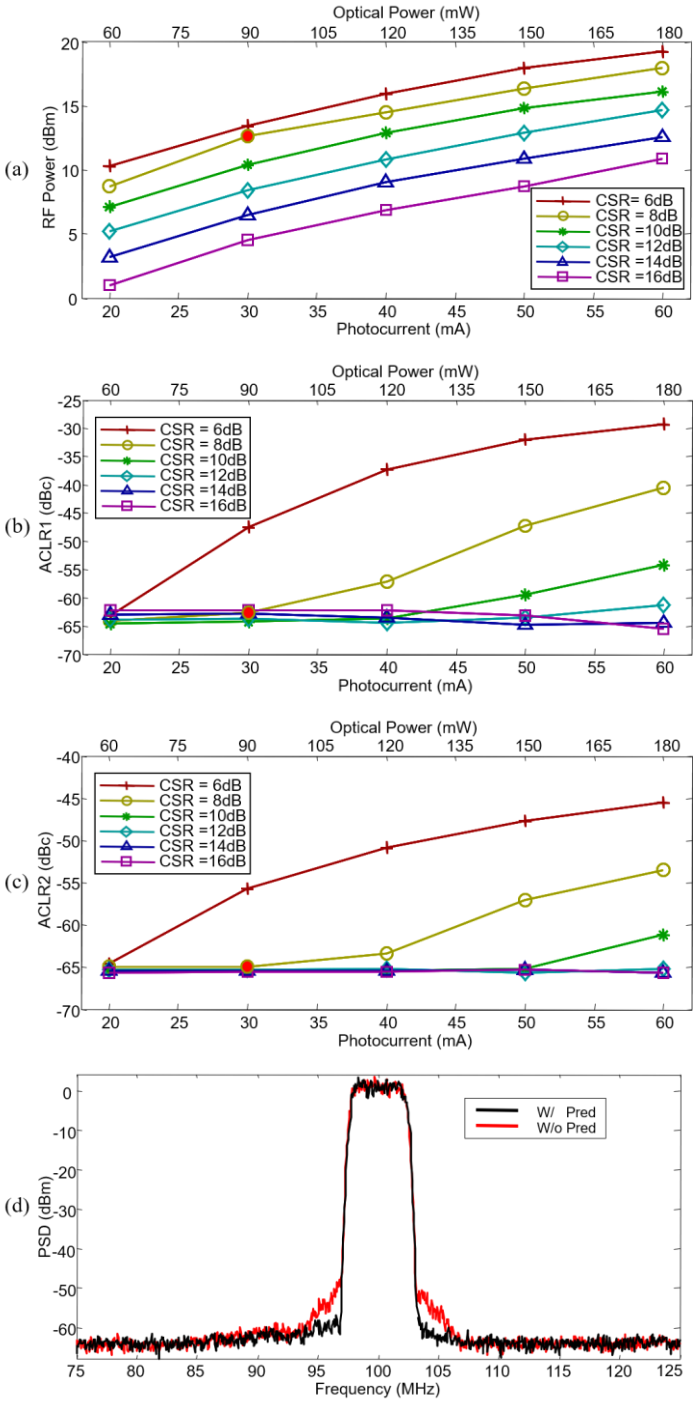

Figure 2.7: Measurement results from the LTE signals recovered at a CC-MUTC photodetector with different PD currents and CSRs. (a) RF power, (b) ACLR1, (c) ACLR2, (d) Measured spectra with and without predistortion at the optimal point.

Hence, there is a tradeoff between RF power and ACLR. As such, the photodetector current and the CSR should be optimized based on application requirements. One candidate optimal point is selected as an example and marked with a red dot in Figures 2.7 (a)-(c), where the photodetector current is 30 mA and the carrier-to-sideband ratio is 8 dB. The spectra at this optimal point, with and without predistortion, are shown in Figure 2.7 (d), where the significance of the predistortion is apparent, as it yields a 9.3-dB ACLR1 improvement.

2.3.4 ALCR dependence on the bias voltage of photodetectors

Lastly, the bias voltage of photodetectors also plays an important role in the link's nonlinearity. It has been reported that the OIP3 of MUTC photodetectors changes with the photocurrent and the maximum OIP3 changes with the reverse bias voltage [81]. In this measurement, the reverse voltage is varied from 4 V to 8 V and two different CSR settings are used. The total DC current is set to be 20 mA, 40 mA, and 60 mA. The dependence of ACLRs on different bias voltages is illustrated in Figure 2.8. The plots show that the ACLRs gradually improve when the reverse bias voltage is increased from 4 V to 8 V. In order to minimize photodetector nonlinearities, we optimized the reverse bias voltage to 8 V and increased the CSR to 14 dB.

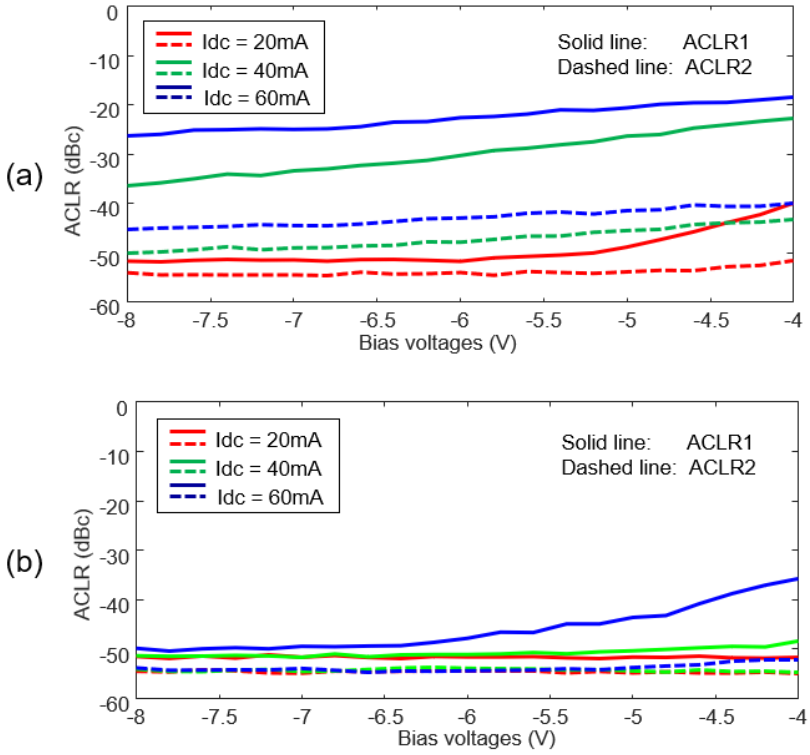

Figure 2.8: ACLRs as a function of the photodetector bias voltage (a) with an CSR of 8 dB, (b) with an CSR of 14 dB.

2.4 High fidelity signal transmission on a DE-MZM link with SSB modulation

The approach described in section 2.3 is based on the double-sideband (DSB) modulation, where optical signals can be distorted in long-distance transmission because of fiber chromatic dispersion. In order to mitigate the chromatic dispersion, single-sideband (SSB) modulation can be used [33]. With this consideration, we propose an SSB modulated link as shown in Figure 2.9, where a DE-MZM is used to modulate data into a single optical sideband. In addition, a tunable optical paired source (TOPS) [82] is used as an optical local oscillator (LO) to control the carrier frequency at the photodetector. Using this approach, the fiber chromatic dispersion can be suppressed. The digital predistortion approach is used to modify the I and Q waveform

components of a QAM signal, where both ACLR and EVM are compared to the one without digital predistortion. Lastly, an EDFA amplifies the optical signal and a photodetector recovers the data.

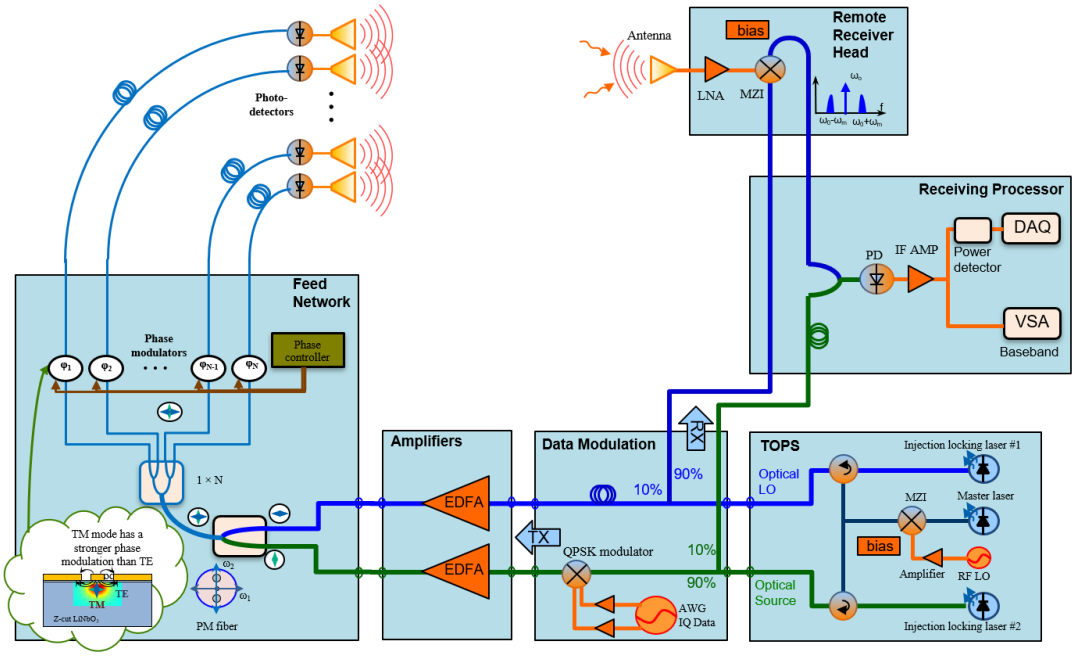

Figure 2.9: A photonic phased array transceiver where the digital predistortion technique is used.

2.4.1 RF signal generation

The digital waveform is generated by RFXpress software, which is used for waveform generation provided by Tektronix. QAM signals with different bandwidths are generated at the same intermediate frequency of 1.06 GHz. The waveform is then predistorted with arcsine function using MATLAB and generated by a Tektronix arbitrary waveform generator that has a 10-bit DAC.

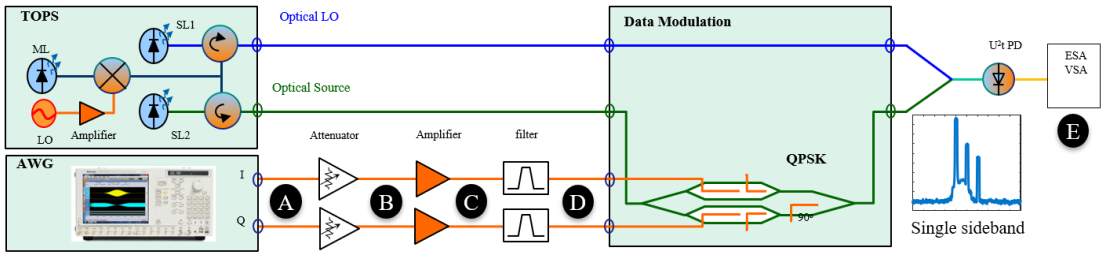

Figure 2.10: A simplified photonic transmitter configuration to verify the SSB operation of DE-MZM and data recovery.

As the optical feed network, the phased array, and the photonic receiver illustrated in Figure 2.9 are not the main concern in high fidelity signal transmission, a simplified link configuration is proposed, which is illustrated in Figure 2.10. The labels A,B,C,D, and E represent different positions of the link where the RF spectra are tested. An electrical spectrum analyzer is used to capture the spectra at labels A to D, so the out-of-band spurs and ACLR can be measured. As shown in Figure 2.11, the out-of-band spurs are observed. At the output of the AWG (point A), there are numerous high-order harmonics where the 8^{th}-order and 10^{th}-order harmonics are strongest. To get rid of those undesired harmonics, a bandpass filter is used to pick up the frequency of interest and a clean spectrum is monitored at the MZM input (Point D). The other issue of the AWG is the RF output power is too low, which leads to reduced modulation efficiency. To resolve this problem, a low noise amplifier (LNA) with ~25 dB gain is used. In order to ensure the LNA is working within its linear region, the RF power at point A needs attenuation, which can be achieved by either an external attenuator or by a decrease of peak-to-peak voltage at the AWG output.

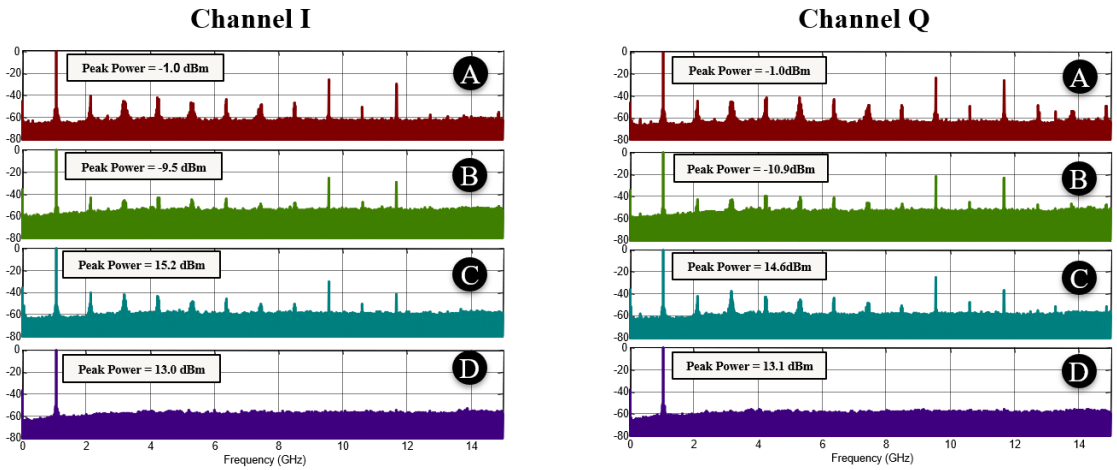

Figure 2.11: The out-of-band spurs generated by the AWG at channel I and Q.

2.4.2 Optical source and LO

The optical source and the optical LO are based on the tunable optical paired source (TOPS) as described in [82]. As shown in Figure 2.10, there are two injection locking lasers (slave laser) and one master laser in the TOPS. The master laser is modulated on an MZM by an RF local oscillator, where the RF signal is intentionally over amplified to generate strong high order harmonics. The output at the MZM has an optical spectrum that contains all the high order sidebands. The modulated master laser output is then coupled through optical circulators into the two injection locking lasers, which are tuned to frequencies near the desired sidebands. By tuning the frequency offset between each injection locking laser and the master laser to match one of the harmonics, the injection locking lasers will be locked. Thus, the optical noise of all the lasers becomes correlated. As such, the output from injection locking laser #1 is used as the optical LO while the output from injection locking laser #2 is used as the optical source, where the frequency offset between them is determined by the RF LO and the order of the injected harmonics. The RF signal can be recovered on a 20-GHz bandwidth

MUTC photodetector by mixing the modulated optical source and the optical LO. The generated RF signals at different frequencies are illustrated in Figure 2.12, which depicts 24 overlaid spectra obtained when the frequency is locked every 1 GHz above 5 GHz, or every 500 MHz below 5GHz.

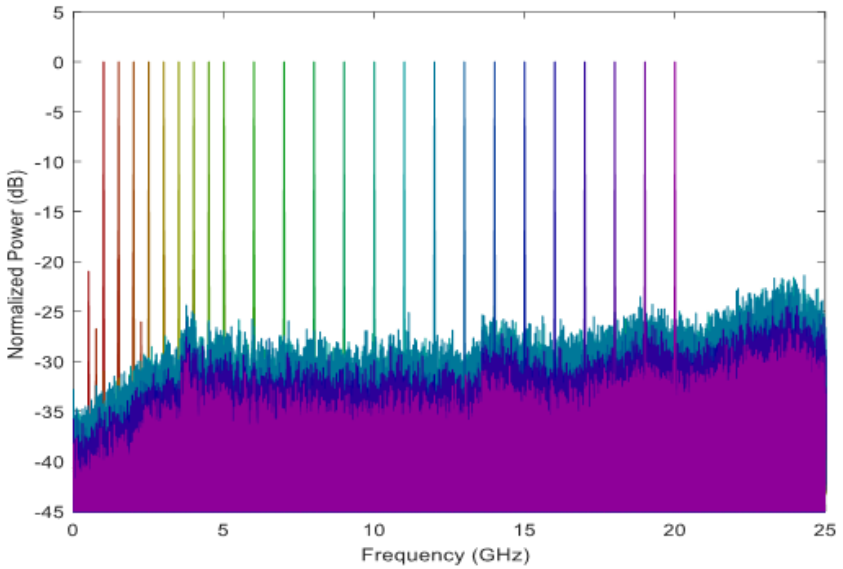

Figure 2.12: Normalized RF power spectrum of the TOPS measured with a 20-GHz MUTC photodetector.

2.4.3 Single sideband modulation

A detailed description on optical SSB modulation can be found in [83], where two RF signals with π/2 phase shift are applied to a dual-electrode MZM. In this link, we use the same approach. However, the π/2 RF phase shift is not generated by an electrical phase shifter, instead it is generated digitally by manipulating the waveform, namely signal I and Q. The configuration is illustrated in Figure 2.10, where I and Q signal are generated at the two output ports of the AWG. In order to maintain SSB

modulation, the phase of the DE-MZM has to be maintained accurately, where two parallel MZMs should be biased to null. The SSB modulation can be completed by using a commercial bias controller, or more simply by a DAC voltage controller. We investigated the stability of SSB modulation using a Thorlabs 40 Gb/s DQPSK modulator (LN86S-FC) at 1 GHz. As shown in Figure 2.13, the SSB modulation is maintained for over 210 minutes even without a bias controller to compensate the thermal drift. This test is done after the modulator is warmed up for a few hours. It is worthwhile to point out that the modulator is more stable if a lower bias voltage is used, as mentioned in Chapter 1.

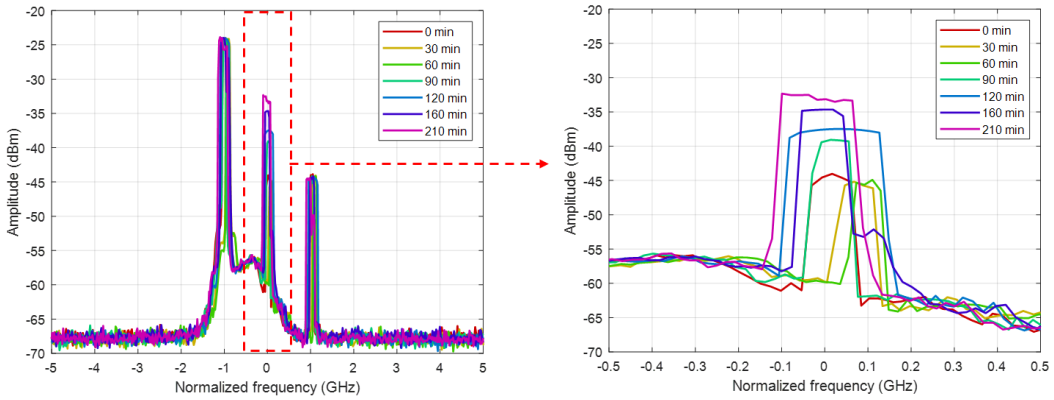

Figure 2.13: The SSB modulation stability test on a Thorlabs DQPSK modulator.

2.4.4 Optical amplification and detection

After the SSB modulated optical source and optical LO are combined, they are amplified by an EDFA, suppressed by an optical attenuator and detected by an MUTC photodetector. A typical spectrum acquired at the photodetector is shown in Figure 2.14

where a 20 MHz LTE signal with 1.06 GHz intermediate frequency is used. The digital predistortion has improved the ACLR by 7.3 dB with 0.8 dB power penalty.

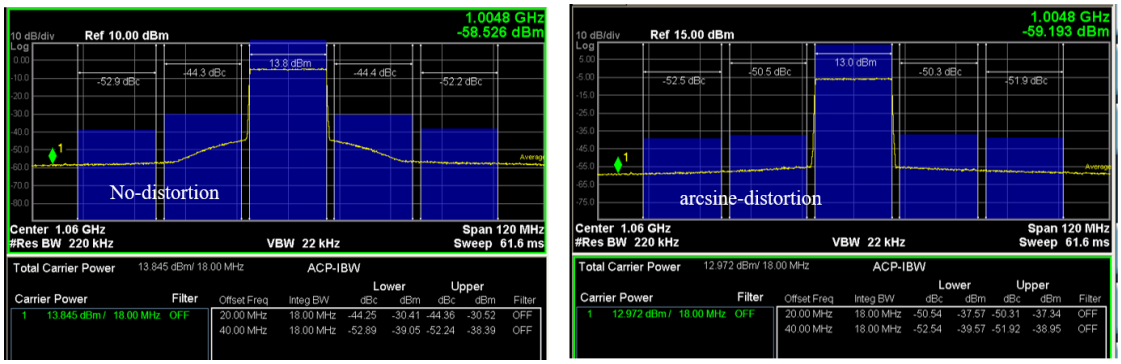

Figure 2.14: The RF spectrum detected on the photodetector without (left) and with (right) digital predistortion.

To compare the nonlinear contributions from an EDFA and a photodetector, we designed two experiments, one with fixed EDFA output power and the other with fixed photocurrent. As shown in Table 2.5, the PD nonlinearity is tested by maintaining the EDFA output at 180 mW and an optical attenuator is used before the photodetector to adjust the photocurrent. When photocurrent is increased from 25 mA to 60 mA, the nonlinear distortion from the photodiod has degraded the ACLR1 by 20.7 dB because the optical attenuator is a passive and linear device. As for the EDFA nonlinearity test, the EDFA output power and optical attenuator are used simultaneously to maintain the photocurrent at 25 mA. The nonlinearity from the EDFA has trivial contribution to the ACLR degradation, which is below 0.5 dB.

Table 2.5: Nonlinearity study on PD and EDFA.

Study	EDFA Power (mW)	Optical Power to PD (mW)	PD current (mA)	Measured RF Power (dBm)	ACLR1 (dBc)	ACLR2 (dBc)	Noise floor (dBm)
PD	180	180	60	19.92	-30.40	-47.06	-52.18
	180	165	55	19.34	-31.87	-48.07	-51.99
	180	150	50	18.43	-35.23	-48.96	-52.61
	180	135	45	17.66	-38.72	-50.14	-54.72
	180	120	40	16.74	-43.76	-51.52	-56.44
	180	105	35	15.63	-48.87	-52.84	-58.06
	180	90	30	14.42	-50.57	-53.03	-59.79
	180	75	25	12.73	-51.19	-53.01	-59.63
EDFA	180	75	25	12.10	-50.07	-51.50	-59.94
	165	75	25	11.90	-49.59	-50.13	-56.87
	150	75	25	11.77	-48.91	-50.10	-56.55
	135	75	25	12.29	-48.72	-49.81	-56.40
	120	75	25	12.43	-49.45	-50.80	-56.39
	105	75	25	12.53	-49.72	-50.96	-59.91
	90	75	25	12.45	-49.73	-51.07	-56.46
	75	75	25	12.37	-49.66	-50.75	-56.42

In order to investigate the frequency tunability and the linearity performance of those frequencies, a 5 MHz 4QAM signal with 1.06-GHz intermediate frequency is used as the test signal. As shown in Table 2.6, the frequency offset on TOPS is set to 1.7 GHz, 2 GHz, 7GHz, 12 GHz, and 17 GHz, where the RF signal recovered on the photodetector are 1.06 GHz lower (because the lower sideband selected in the SSB modulator). The photocurrent is set to 30 mA at those frequencies, where both RF power and ACLR are slightly better at lower frequencies. In general, the ACLR1s at those frequencies can meet the -44.2 dBc requirement of the telecommunications industry standard [62].

Lastly, the constellation of the 4QAM signal at the photodetector is measured using a digital oscilloscope (Aglient Infiniium DSO-S 204A), where the Keysight 89600 VSA software is used. As the digital oscilloscope supports frequencies up to 2 GHz, the

constellation diagrams at 0.94 GHz, 1.44 GHz, and 1.94 GHz are tested and shown in Figure 2.15, where both spectrum and constellation diagrams are very clean. The last two columns of Table 2.6 contain data characterizing the signal constellations, namely error vector magnitude (EVM) and SNR. In general, SNR should be maintained as high as possible while EVM should be kept as low as possible. Usually, they are corresponded to each other which means higher SNR gives lower (better) EVM.

Table 2.6: QAM signal transmission at different frequencies.

TOPS Offset (GHz)	RF (GHz)	PD current (mA)	RF Power (dBm)	ACLR1 (dBc)	ACLR2 (dBc)	EVM (%)	SNR (dB)
17	15.94	31.8	5.52	-49.82	-57.11	1.36	37.27
12	10.94	29.5	5.93	-48.11	-56.02	1.61	35.84
7	5.94	29.5	5.96	-51.34	-58.43	1.89	34.45
2	0.94	29.2	10.63	-53.72	-58.52	1.89	34.47
1.7	0.64	30.1	8.70	-52.50	-58.13	1.87	34.56

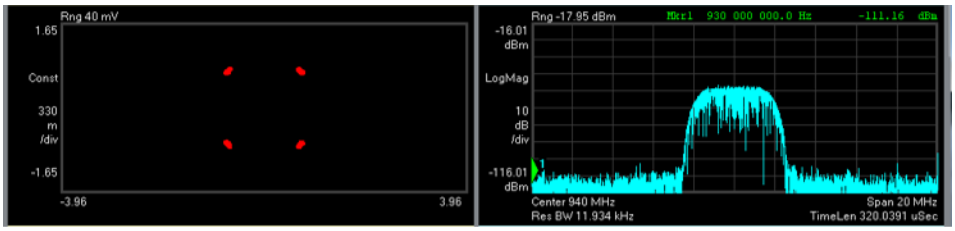

(a) 0.94 GHz

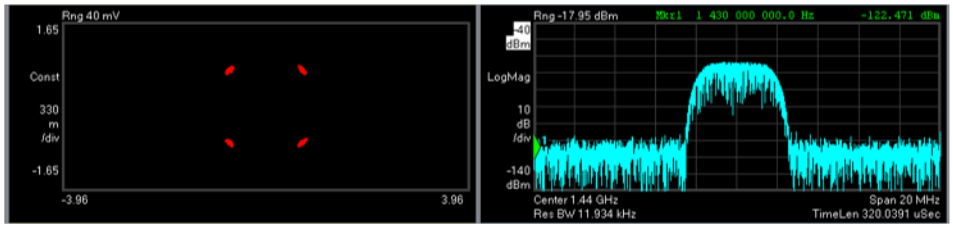

(b) 1.44 GHz

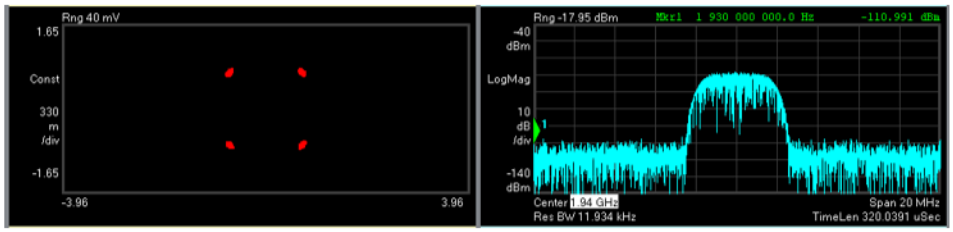

(c) 1.94 GHz

Figure 2.15: Constellation diagrams and spectra of a 5 MHz 4QAM signal acquired at the photodetector of the link at different frequencies.

2.5 Summary

In this chapter, digital predistortion techniques in power amplifiers and optical Mach-Zehnder modulators are summarized. Then the digital predistortion based on modifying the digital waveform is proposed, analyzed, and simulated. With the help of a dual-electrode Mach-Zehnder modulator, the digital predistortion is applied on one of the arms while the other arm is used to provide an adjustable optical carrier. The digital predistortion is validated by comparing the recovered signal on the photodetector where 3-9 dB improvement of ACLR1 is monitored for 5 MHz and 20 MHz LTE signals. Then the digital predistortion is implemented in a photonic transceiver where tunable optical

paired sources (TOPS) and single sideband (SSB) modulation are used. Again, the digital predistortion helps to improve the link's ACLR by 6-8 dB for various frequencies from 1.7 GHz to 17 GHz.

Chapter 3

TWO-WAVELENGTH MZM LINEARIZATION

3.1 Introduction

Digital predistortion techniques require use of an electrical predistorter or knowledge of input signals, which are less competitive to optical linearization techniques that can fit for different types of input signals. In this chapter, a two-wavelength Mach-Zehnder modulator (MZM) linearization technique is discussed.

MZMs are inherently nonlinear because of their sinusoidal transfer function, which is the dependence of the output light intensity on the electrical input signal. In electro-optic phase modulator, phase detection requires conversion of phase to intensity, which similarly yields a sinusoidal transfer function. Accordingly, considerable research efforts have been devoted to developing linearized modulators [84]–[86] or assistive techniques [87]–[89] that effectively yield linear response. In general, compensation can be performed electronically, by using analog circuitry or digital signal processing, or optically. However, the electronic approaches are often limited by the frequency response of the employed devices or by digital signal processor capacity. In the optical domain, linearization is obtained by adding a compensation MZM in parallel or in series to the main MZM, so that the third-order intermodulation (IMD3) generated by the compensation MZM has the same amplitude and opposite phase to the IMD3 from the main MZM, and therefore the two IMD3 signals cancel each other.

Among the optical linearization techniques, the dual-parallel modulator linearization method has garnered significant attention and is widely used in linearized

analog photonic links [90]–[92]. In this case, there are two general schemes with either coherent or incoherent optical sources. In the coherent mode when one laser is used [84], [90], [91], the IMD3 cancellation is obtained in the optical domain, whereas in the incoherent mode when two lasers are used [93]–[95], the IMD3 cancellation happens in the RF domain. Notably, accurate control of tunable-ratio optical splitters [90] and/or multiple phase shifters [91] are needed in the coherent one-laser approach. Alternatively, two-laser mode is limited by the tunability of RF power ratio, which is determined by V_π [93]–[95], bandwidth and phase deviation of the RF hybrid coupler [93], [95], suppression ratio, and bandwidth accuracy of fiber Bragg grating (FBG) filters [96].

To summarize, most of the existing modulator linearization techniques need an additional path and asymmetric feed to generate equal and opposite IMD3 signals. The asymmetric feed can be realized using RF attenuators/amplifiers, optical attenuators/amplifiers [97], wavelength dependent V_π [93], or polarization dependent V_π [95], [98]. The π-phase difference between the main and secondary channels can be realized by using an additional phase modulator [84], [90], [91], [99], biasing two MZMs at opposite quadratures, adding a 180-degree RF hybrid coupler [93], using push-pull modulation [94], using lower and upper sideband modulation assisted by an FBG [96], or employing RF phase shifters [100]. Besides, modulators are biased at quadrature to eliminate even-order intermodulation in multi-octave applications [94] or biased around null for high SFDR and low noise figure in sub-octave applications [90].

3.2 Optically coherent and incoherent linearization techniques

As mentioned in the previous section, there are two schemes to cancel the MZM IMD3 using optical methods, i.e., optically coherent linearization and optically

incoherent linearization. Their main difference is whether there is optical intermodulation between two optical channels, where one channel is used to deliver data and the other is used as an IMD3 compensator.

3.2.1 Optically coherent linearization

In optically coherent linearization technique, a laser output is split to feed two parallel MZMs. The outputs of the two MZMs have IMD3s of the same amplitude and 180-degree phase shift. As the two optical outputs are coherent, the IMD3 is minimized in optical domain on an optical power coupler. Based on the illustration of this optically coherent linearization, as shown in Figure 3.1, the DC and RF current on the photodetector are calculated using a two-tone test to investigate how IMD3 can be fully suppressed.

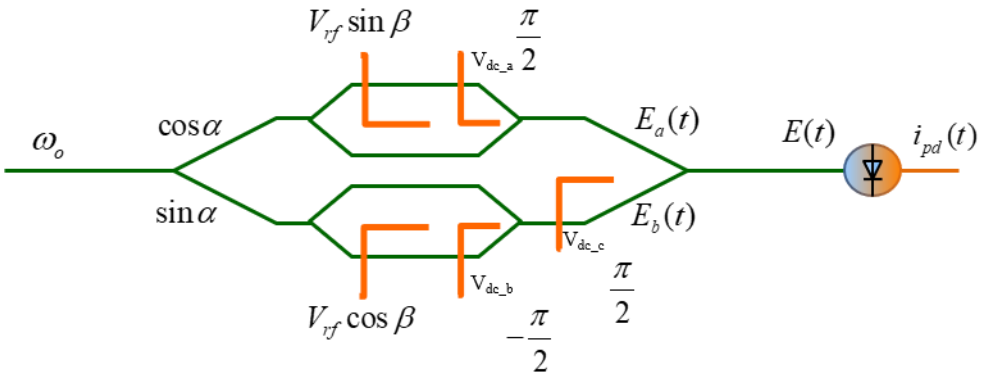

Figure 3.1: An illustration of optically coherent linearization techniques.

The amplitude of the RF signals fed to two MZMs are:

$$\begin{cases} V_{rf\_a}(t) = V_{rf}\sin\beta\,[\sin(\omega_1 t) + \sin(\omega_2 t)] \\ V_{rf\_b}(t) = V_{rf}\cos\beta\,[\sin(\omega_1 t) + \sin(\omega_2 t)]\,, \end{cases} \tag{3.1}$$

where V_{rf} is amplitude of the RF signal before the RF splitter, $\sin\beta$ and $\cos\beta$ determine the RF power split ratio, ω_1 and ω_2 are the two frequencies included in the RF signal. The phases introduced by those RF signals are:

$$\begin{cases} \varphi_{rf\_a}(t) = \frac{\pi V_{rf}\sin\beta}{V_{\pi rf}}[\sin(\omega_1 t) + \sin(\omega_2 t)] \\ \varphi_{rf\_b}(t) = \frac{\pi V_{rf}\cos\beta}{V_{\pi rf}}[\sin(\omega_1 t) + \sin(\omega_2 t)] \end{cases}, \tag{3.2}$$

where $V_{\pi rf}$ is the halfwave voltage of the MZM around frequency ω_1 and ω_2. For convenience, we define the modulation index as:

$$\begin{cases} m_a = \frac{\pi V_{rf}\sin\beta}{V_{\pi rf}} \\ m_b = \frac{\pi V_{rf}\cos\beta}{V_{\pi rf}} \end{cases}. \tag{3.3}$$

The phases introduce by the three DC bias voltages are:

$$\begin{cases} \varphi_{dc\_a} = \frac{\pi V_{dc\_a}}{V_{\pi dc}} \\ \varphi_{dc\_b} = \frac{\pi V_{dc\_b}}{V_{\pi dc}} \\ \varphi_{dc\_c} = \frac{\pi V_{dc\_c}}{V_{\pi dc}} \end{cases}. \tag{3.4}$$

The total phase generated by the MZMs can be calculated by adding the DC and RF components:

$$\begin{cases} \varphi_a = \varphi_{rf\_a} + \varphi_{dc\_a} \\ \varphi_b = \varphi_{rf\_b} + \varphi_{dc\_b} \end{cases}. \tag{3.5}$$

As both MZMs and the phase modulator have push-pull configuration, each MZM is driven by half of the RF or DC bias voltage. If the input RF signal has an electrical amplitude of E_o, the electrical field at the output of two MZMs are:

$$\begin{cases} E_a(t) = 2E_o\, exp(j\omega_o t) cos\,\alpha\, cos(\varphi_a/2)\, exp(j\varphi_{dc\_c}/2) \\ E_b(t) = 2E_o\, exp(j\omega_o t) sin\,\alpha\, cos(\varphi_b/2)\, exp(-j\varphi_{dc\_c}/2) \end{cases}, \tag{3.6}$$

where ω_o is angular frequency of the optical carrier, α determines the optical split ratio, $cos(\varphi_a/2)$ and $cos(\varphi_b/2)$ represent the sinusoidal amplitude modulation of MZM and $exp(j\varphi_{dc\_c})$ is the phase due to the phase modulator after the lower MZM. The total electrical field after the optical combiner is:

$$\begin{cases} E(t) = E_a(t) + E_b(t) = 2E_o \exp(j\omega_o t)\tilde{E}(t) \\ \tilde{E}(t) = \cos\alpha \cos(\varphi_a/2)\, exp(j\varphi_{dc_c}/2) \\ \quad + sin\,\alpha\, cos(\varphi_b/2)\, exp(-j\varphi_{dc_c}/2)\,. \end{cases} \tag{3.7}$$

The optical power on the photodetector can be estimated based on the electrical field and the responsivity of the photodetector, which is given by:

$$\begin{cases} I(t) = \mathcal{R}P(t) \\ P(t) = \frac{E(t)\cdot E(t)^*}{Z_0} = \frac{4E_0^2}{Z_0}\tilde{E}(t)\cdot\tilde{E}(t)^* \\ \tilde{E}(t)\cdot\tilde{E}(t)^* = cos^2\alpha\cdot cos^2\left(\frac{\varphi_a}{2}\right) + sin^2\alpha\cdot cos^2\left(\frac{\varphi_b}{2}\right) \\ +\sin(2\alpha) cos\left(\frac{\varphi_a}{2}\right) cos\left(\frac{\varphi_b}{2}\right) cos\varphi_{dc\_c}\,. \end{cases} \tag{3.8}$$

Given φ_{dc_c} = π/2 and $cos^2\left(\frac{\varphi_a}{2}\right) = \frac{1+\cos(\varphi_a)}{2}$, the photocurrent can be written as:

$$I(t) = \mathcal{R}\cdot\frac{4E_0^2}{Z_0}\left(cos^2\alpha\,\frac{1+\cos(\varphi_a)}{2} + sin^2\alpha\cdot\frac{1+\cos(\varphi_b)}{2}\right)\,. \tag{3.9}$$

If two MZMs are biased at positive and negative quadrature bias, where $\varphi_{dc\_a} = \frac{\pi}{2}$ and $\varphi_{dc\_b} = -\frac{\pi}{2}$, the photocurrent is:

$$I(t) = \mathcal{R}\cdot\frac{2E_0^2}{Z_0}\left(1 - cos^2\alpha\,\sin\left(\varphi_{rf_a}\right) + sin^2\alpha\sin\left(\varphi_{rf_b}\right)\right)\,. \tag{3.10}$$

There are three parts in the photocurrent, which includes the DC photocurrent, the RF photocurrent from the primary MZM, and the RF photocurrent from the secondary MZM is:

$$\begin{cases} I_{\mathrm{dc}} = \mathcal{R} \cdot \frac{2E_0^2}{Z_0} \\ I_{\mathrm{rf\_p}} = -\mathcal{R} \cdot \frac{2E_0^2}{Z_0} cos^2\alpha \sin(\varphi_{rf\_a}) \\ I_{\mathrm{rf\_s}} = \mathcal{R} \cdot \frac{2E_0^2}{Z_0} sin^2\alpha \sin(\varphi_{rf\_b}) \ . \end{cases} \tag{3.11}$$

Using Taylor expansion and keeping the first and third order, the RF photocurrent can be written as:

$$\begin{cases} I_{\mathrm{rf\_p}} = -\mathcal{R} \cdot \frac{2E_0^2}{Z_0} cos^2\alpha \left[m_a (sin\,\omega_1 t + sin\,\omega_2 t) - \frac{m_a^3}{6} (sin\,\omega_1 t + sin\,\omega_2 t)^3 \right] \\ I_{\mathrm{rf\_s}} = \mathcal{R} \cdot \frac{2E_0^2}{Z_0} sin^2\alpha \left[m_b (sin\,\omega_1 t + sin\,\omega_2 t) - \frac{m_b^3}{6} (sin\,\omega_1 t + sin\,\omega_2 t)^3 \right] . \end{cases} \tag{3.12}$$

According to the equation, the fundamental and third-order photocurrents are out of phase. If we further expand the third order photocurrent, it can be written as:

$$(sin\,\omega_1 t + sin\,\omega_2 t)^3 = \frac{9}{4}(sin\,\omega_1 t + sin\,\omega_2 t) - \frac{1}{4}(sin\,3\omega_1 t + sin\,3\omega_2 t) + \frac{3}{4}(sin(2\omega_1 - \omega_2)\,t + sin(2\omega_2 - \omega_1)\,t) - \frac{3}{4}(sin(2\omega_1 + \omega_2)\,t + sin(2\omega_2 + \omega_1)\,t) . \tag{3.13}$$

We can see the third-order photocurrent contribute to several RF frequencies, including the third-order intermodulation at $2\omega_1 - \omega_2$ and $2\omega_2 - \omega_1$, so the amplitude of IMD3 photocurrents of two MZMs are:

$$\begin{cases} I_{\mathrm{IMD3\_p}}(t) = \frac{\mathcal{R} \cdot E_0^2 \cdot cos^2\alpha \cdot m_a^3}{4Z_0} [sin(2\omega_1 - \omega_2)\,t + sin(2\omega_2 - \omega_1)\,t] \\ I_{\mathrm{IMD3\_s}}(t) = -\frac{\mathcal{R} \cdot E_0^2 \cdot sin^2\alpha \cdot m_b^3}{4Z_0} [sin(2\omega_1 - \omega_2)\,t + sin(2\omega_2 - \omega_1)\,t] . \end{cases} \tag{3.14}$$

As they have a 180-degree phase difference, the IMD3 photocurrent can be cancelled under the following condition:

$$cos^2\alpha \cdot m_a^3 = sin^2\alpha \cdot m_b^3 \; or \; tan^2\alpha = tan^2\beta \; . \tag{3.15}$$

3.2.2 Optically incoherent detection

In the optically incoherent linearization technique, the outputs of the two MZMs have IMD3s of the same amplitude and 180-degree phase shift. As the two optical outputs are incoherent, the IMD3s are not cancelled optically. Instead, the IMD3 cancellation happens in RF domain on the photodetector where two optical outputs are converted to RF signals. Based on the illustration of this optically incoherent linearization, as shown in Figure 3.2, the DC and RF current on the photodetector are calculated using a two-tone test to investigate how IMD3 can be fully suppressed.

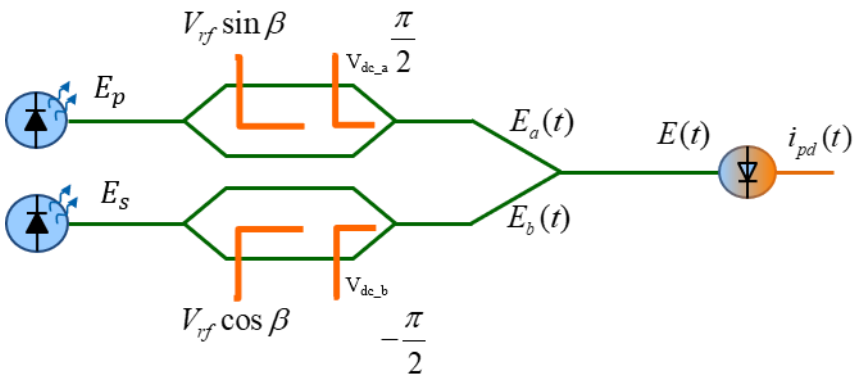

Figure 3.2: An illustration of optically incoherent linearization techniques.

In the case of optically incoherent detection, two MZMs operate in parallel and there is no phase modulator on the secondary channel. The electrical field at the output of the MZMs are:

$$\begin{cases} E_a(t) = 2E_p\, exp(j\omega_p t)\, cos(\varphi_a/2) \\ E_b(t) = 2E_s\, exp(j\omega_s t) cos(\varphi_b/2)\,, \end{cases} \tag{3.16}$$

where E_p and E_s are the amplitude of optical signals from primary and secondary lasers, ω_p and ω_s are the angular frequency of the two lasers. The photocurrents attributed to two MZMs are:

$$\begin{cases} I(t)\_\mathrm{p} = \frac{2\mathcal{R}E_p^2}{Z_0}(1+\cos(\varphi_a)) \\ I(t)\_\mathrm{s} = \frac{2\mathcal{R}E_s^2}{Z_0}(1+\cos(\varphi_b)) \end{cases}, \tag{3.17}$$

where φ_a and φ_b are the total phases generated by RF and DC bias on two parallel MZMs. If those MZMs are biased at positive and negative quadrature bias, where $\varphi_{dc\_a} = \frac{\pi}{2}$ and $\varphi_{dc\_b} = -\frac{\pi}{2}$, the photocurrents become:

$$\begin{cases} I(t)_\mathrm{p} = \frac{2\mathcal{R}E_p^2}{Z_0}\left(1-\sin\left(\varphi_{rf\_a}\right)\right) \\ I(t)_\mathrm{s} = \frac{2\mathcal{R}E_s^2}{Z_0}\left(1+\sin\left(\varphi_{rf\_b}\right)\right) \end{cases}, \tag{3.18}$$

where φ_{rf_a} and φ_{rf_b} are the phases generated by input RF signals. We put the DC photocurrents aside, use Taylor expansion, and only keep the first and third order, then the RF photocurrents can be written as:

$$\begin{cases} I_{\mathrm{rf\_p}} = -\frac{2\mathcal{R}E_p^2}{Z_0}\left[m_a(sin\,\omega_1 t + sin\,\omega_2 t) - \frac{m_a^3}{6}(sin\,\omega_1 t + sin\,\omega_2 t)^3\right] \\ I_{\mathrm{rf\_s}} = \frac{2\mathcal{R}E_S^2}{Z_0}\left[m_b(sin\,\omega_1 t + sin\,\omega_2 t) - \frac{m_b^3}{6}(sin\,\omega_1 t + sin\,\omega_2 t)^3\right] \end{cases}, \tag{3.19}$$

Using similar expansion approach in Equation 3.13, the IMD3 photocurrents from two MZMs can be written as:

$$\begin{cases} I_{\mathrm{IMD3\_p}}(t) = \frac{\mathcal{R}E_p^2 m_a^3}{4Z_0}[sin(2\omega_1-\omega_2)\,t + sin(2\omega_2-\omega_1)\,t] \\ I_{\mathrm{IMD3\_s}}(t) = -\frac{\mathcal{R}E_s^2 m_b^3}{4Z_0}[sin(2\omega_1-\omega_2)\,t + sin(2\omega_2-\omega_1)\,t] \end{cases}. \tag{3.20}$$

As a result, the condition to fully suppress the IMD3 is:

$$E_p^2 \cdot m_a^3 = E_s^2 \cdot m_b^3\,. \tag{3.21}$$

3.3 Principle of two-wavelength linearization on MZMs

In this section, a two-wavelength linearization technique is introduced to suppress IMD3 of MZMs. A theoretical model is analyzed and simulated using MATLAB.

3.3.1 Schematic of two-laser MZM linearization

In this approach, two separate MZMs are driven by different lasers, one for data transmission and the other for IMD3 suppression; the π-phase difference is achieved by biasing two modulators at opposite quadratures. When using two lasers, optical power ratio is easier to control compared to one-laser linearization where a tunable optical splitter is required. It is worth pointing out that the second laser operates at a lower power and generates lower photocurrent, so the relative intensity noise (RIN) of the link attributed to the second laser is less significant. In a RIN limited link, which operates at high photocurrent, it is reasonable to choose a low-cost laser as the assistive laser. Using two separate MZMs allows extending the tunability of RF power ratio to achieve lower link-gain penalty compared to a single or integrated dual parallel MZM, where the RF power ratio is usually limited to 1/3 [95].

The system consists of a primary channel and a secondary channel, as shown in Figure 3.3. The primary channel is configured to maximize the signal of interest, where a strong optical signal and a moderate RF drive signal are used such that the primary channel generates RF power on the photodetector, while minimizing the IMD3 arising from modulator nonlinearity. The secondary channel is intended to cancel the IMD3 of the primary channel by using a weaker optical signal and a stronger RF drive signal. In this way, IMD3 of the same amplitude as in the primary channel is generated; however, with much lower fundamental power. To enable the IMD3 cancellation, a 180-degree

phase difference between the primary and secondary channels is required. This is achieved by biasing the primary channel at positive quadrature and the secondary channel at negative quadrature. Quadrature biasing also ensures that the even-order nonlinearities are suppressed in both channels.

For illustration, a system diagram is provided in Figure 3.3, where two incoherent lasers (LD 1 and LD 2) are used and their optical frequencies are offset by a large span (tens or hundreds of gigahertz), sufficient to ensure the photodetector does not respond to any intermodulation between the two channels in the optical domain. The input RF signal is split into two RF outputs at a certain power ratio and each RF output drives an MZM. After modulation, two parallel channels (links) are combined, amplified by an EDFA and detected on the same photodetector for signal recovery. Since the two channels are driven by the same RF signal, the recovered RF signals are coherent and can beat with each other. As the two recovered RF signals are out of phase with equal IMD3 and asymmetric power, they beat with each other destructively giving a significant IMD3 suppression and a small signal reduction. As a result, by properly tuning the optical/RF power ratios, and maintaining the π-phase difference, the IMD3 can be suppressed while the signal of interest is recovered with enhanced fidelity.

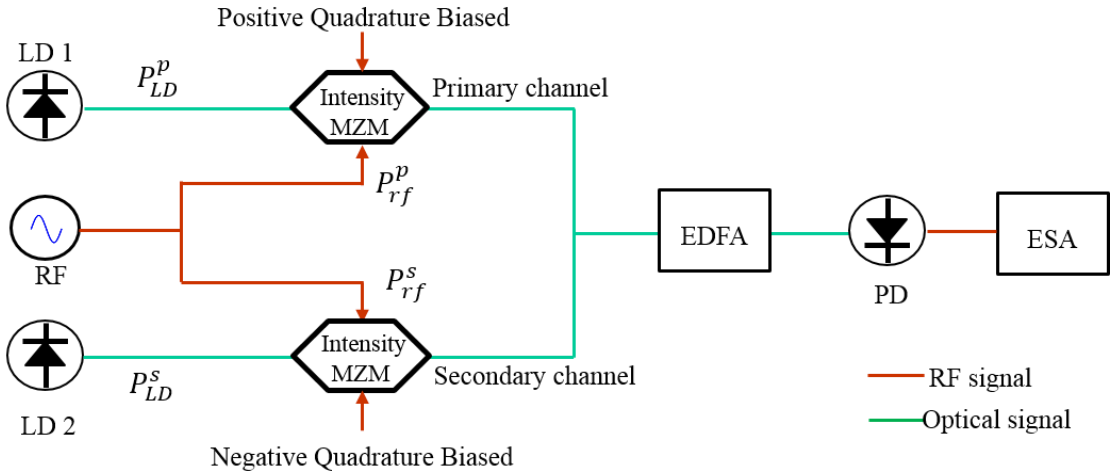

Figure 3.3: Two parallel modulators are fed with two separate lasers and driven by a common RF source. With proper optical and RF power ratios between two optical channels, third order intermodulation (IMD3) on the photodetector is suppressed if the phase difference between two channels is π. LD: laser diode; PD: photodetector; MZM: Mach-Zehnder modulator; EDFA: erbium-doped fiber amplifier; ESA: electrical spectrum analyzer.

To fully suppress the IMD3, an optimum condition should be found. First, the electro-optic modulators have a push-pull configuration, so the electric field at the primary and secondary channel before optical combiner is:

$$\begin{cases} E_p = E_{LD}^{p} \cdot e^{j\omega_p t} \cdot \cos\left(\frac{\varphi_{dc}^{p}+\varphi_{rf}^{p}}{2}\right) \\ E_s = E_{LD}^{s} \cdot e^{j\omega_s t} \cdot \cos\left(\frac{\varphi_{dc}^{s}+\varphi_{rf}^{s}}{2}\right), \end{cases} \tag{3.22}$$

where $E_{LD}^{p} \cdot e^{j\omega_p t}$ and $E_{LD}^{s} \cdot e^{j\omega_s t}$ are the electrical fields of the primary and secondary optical sources, φ_{dc}^{p} and φ_{dc}^{s} are the modulation phases introduced by DC biasing, φ_{rf}^{p} and φ_{rf}^{s} are the modulation phases introduced by the RF drive signals, which can be expressed as:

$$\begin{cases} \varphi_{rf}^{p} = \frac{\pi V_p^p v(t)}{V_{\pi\_rf}}, & V_p^p = k\sqrt{P_{rf}^p/Z_0} \\ \varphi_{rf}^{s} = \frac{\pi V_p^s v(t)}{V_{\pi\_rf}}, & V_p^s = k\sqrt{P_{rf}^s/Z_0}\,. \end{cases} \tag{3.23}$$

P_{rf}^p and P_{rf}^s are the RF drive signal powers at the modulator inputs, $v(t)$ is the normalized time domain waveform, and k is the factor to convert root mean square (RMS) voltage to peak voltage (V_p^p and V_p^s). Using the square law of power detection, the combined optical power before the erbium-doped fiber amplifier (EDFA) is:

$$P_{tot} = \frac{1}{2}\left[P_{LD}^s\left(1+\cos(\varphi_{dc}^s+\varphi_{rf}^s)\right)+P_{LD}^p\left(1+\cos(\varphi_{dc}^p+\varphi_{rf}^p)\right)\right]. \tag{3.24}$$

Given quadrature phase bias conditions $\varphi_{dc}^p = \frac{\pi}{2}$, $\varphi_{dc}^s = -\frac{\pi}{2}$, and that the two optical sources are incoherent, the photocurrent on the PD is:

$$I_{PD} = \frac{1}{2}\Re G_{EDFA}\left(P_{LD}^p + P_{LD}^s - P_{LD}^p \sin\varphi_{rf}^p + P_{LD}^s \sin\varphi_{rf}^s\right). \tag{3.25}$$

Taylor-expanding the sine functions, and keeping only the fundamental and third-order terms, yields the RF photocurrent:

$$I_{RF} = \frac{1}{2}\Re G_{EDFA}\left(P_{LD}^s\left(\varphi_{rf}^s - \frac{(\varphi_{rf}^s)^3}{6}\right) - P_{LD}^p\left(\varphi_{rf}^p - \frac{(\varphi_{rf}^p)^3}{6}\right)\right). \tag{3.26}$$

To completely suppress the third-order terms, $P_{LD}^s \cdot (\varphi_{rf}^s)^3$ and $P_{LD}^p \cdot (\varphi_{rf}^p)^3$ must be equal. As the RF modulation phase is linearly proportional to the square root of the driving RF power, as shown in Equation 3.23, the optimum optical and RF power relationship to completely suppress the IDM3 is:

$$\left(\frac{P_{LD}^p}{P_{LD}^s}\right)^2 = \left(\frac{P_{rf}^s}{P_{rf}^p}\right)^3. \tag{3.27}$$

3.3.2 Numerical simulation

The above model is used to simulate a two-tone intermodulation [91] at 1 GHz in MATLAB. As shown in Figure 3.4, the IMD3, without proper power ratio, ranges

from -60 to -70 dBm, while the IMD3 with proper ratio along the blue line is below -100 dBm. The slope of the line is 2/3, which is consistent with the relationship described in Equation 3.27. While the IMD3 can be effectively suppressed using this approach, a small amount of fundamental power is reduced, which is referred to as the power penalty. We can minimize the power penalty by using a higher RF/optical power splitting ratio, but it is limited in real-world applications because physical devices have limitations, such as the power tuning range of lasers or the maximum output of low-noise amplifiers.

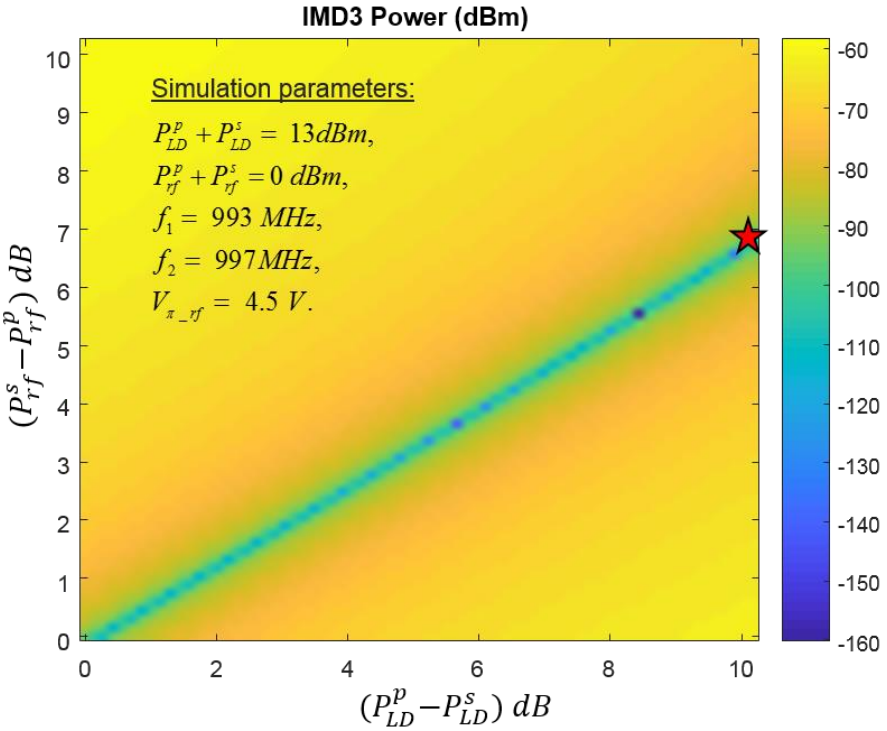

Figure 3.4: Simulated result based on two-wavelength linearization technique. RF and optical power splitting ratios are in a range from 0 to 10 dB. IMD3 is suppressed along the blue line where two channels have IMD3 with same amplitude and 180-degree phase difference. The red star indicates a power ratio with good IMD3 suppression and small power penalty.

3.4 Pathlength match

The 180-degree phase difference between the two parallel MZMs is critical to cancel the IMD3. In the two-laser linearization approach, the 180-degree phase difference is achieved by operating two MZMs at positive and negative quadratures. However, the pathlength before and after the MZMs should be matched to secure the 180-degree phase difference. The pathlength before the MZM is RF pathlength, which includes the pathlength contribution from RF cables, adaptors, attenuators and LNA. The pathlength after the MZM is optical pathlength, which includes the pathlength contribution from optical fiber and true time delay line. The pathlength introduced phase is frequency dependent and can be calculated using the following equation:

$$\varphi = 2\pi \cdot n \cdot \frac{L}{\lambda}, \tag{3.28}$$

where *n* is refractive index of medium, *L* is the length of RF cable or optical fiber, and λ corresponds to the frequency of interest. In order to achieve pathlength match, two calibration tests are conducted with the help of a network analyzer.

3.4.1 RF pathlength match.

The RF assemblies in the two parallel channels are shown in Figure 3.5. The primary channel has an LNA and a variable RF attenuator, while the secondary channel has an LNA and a few RF adaptors to match physical pathlength. Although the physical pathlengths are matched, the RF pathlengths may be different, because the variable RF attenuator has an unknown RF pathlength, depending on its internal design.

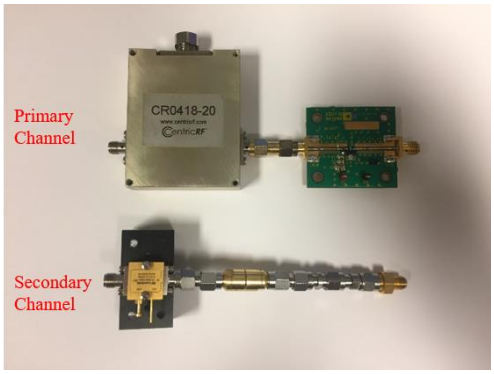

Figure 3.5: The RF assemblies before the input of MZMs.

In order to measure the RF pathlength of those assemblies, a network analyzer is used. As shown in Figure 3.6, port-1 of the network analyzer is connected to the input of the RF assembly, while port-2 of the network analyzer is connected to the output. Continuous sinusoidal waveform is fed through port-1 by the network analyzer and detected at port-2. The signals at two ports are compared to estimate the propagation time through the RF assemblies, then the RF pathlength and the phase are calculated.

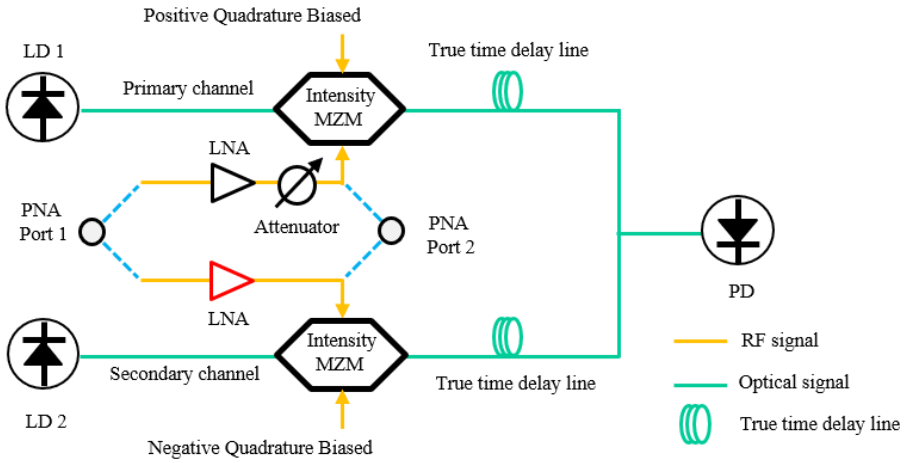

Figure 3.6: The electrical pathlength of two RF assemblies are measured using a PNA network analyzer.

In our experiment, the RF frequency is set around 1 GHz, which is the intermediate frequency of the LTE signal. The result is given in Table 3.1 and Figure 3.7. In the primary channel, the variable attenuator introduces additional pathlength and the measured RF pathlength ranges from 25.2 cm to 33.1 cm. The 7.9 cm difference is the tunable pathlength range of the RF attenuator. In this case, the RF attenuator also serves as a phase shifter. In the secondary channel, the RF assembly has a fixed pathlength of 13.6 cm. In order to match RF pathlength, additional short RF cable is added to the secondary channel.

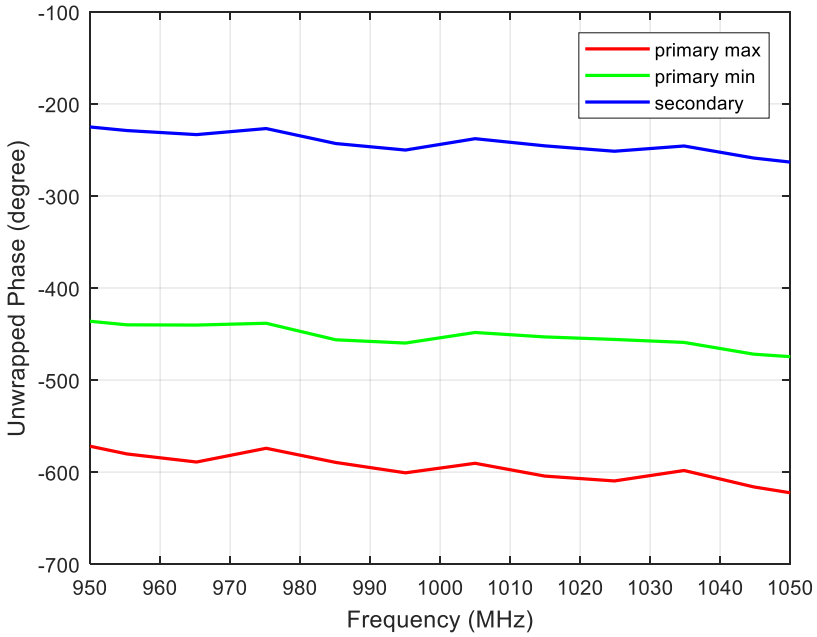

Figure 3.7: The unwrapped phase of two RF assemblies are test around 1 GHz, the primary channel has a variable phase because of the tunable RF attenuator.

Table 3.1: Measured pathlength of two RF assemblies.

	Primary Max	Primary Min	Secondary
Phase delay @ 1GHz	-595.6°	-454.1°	-244.0°
RF length	33.1 cm	25.2 cm	13.6 cm

3.4.2 Optical pathlength match

With accurate RF pathlength match, we can proceed to optical pathlength match. As it is hard to measure the length of an optical fiber directly, the fiber length can be tested in RF domain using a network analyzer. This experiment is illustrated in Figure 3.8, and the propagation time from the input of RF assembly (port 1) to the photodetector (port 2) is measured. The propagation time includes both the RF propagation time and the optical propagation time. Since the RF pathlength is matched, the RF propagation time is the same. Then, the optical pathlength match can be achieved by equalizing the total propagation time.

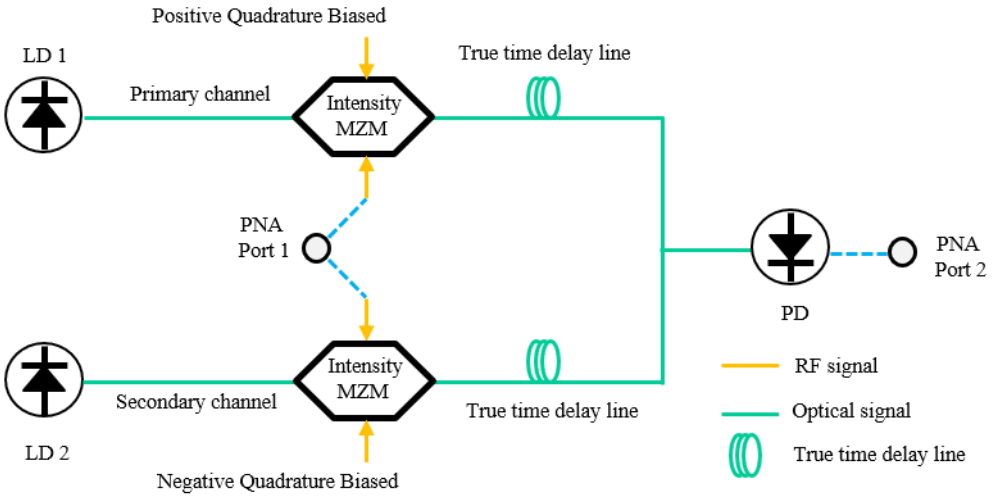

Figure 3.8: The optical pathlength of two channels are measured with a PNA network analyzer.

The experiment result is given in Figure 3.9. As shown in the table, the phase delay can be measured at positive and negative quadrature bias condition. The data confirms that negative and positive quadrate bias has 180-degree offset. According to the data in Table 3.2, the optical pathlength has a difference of 12 mm, which can be compensated by true time delay lines.

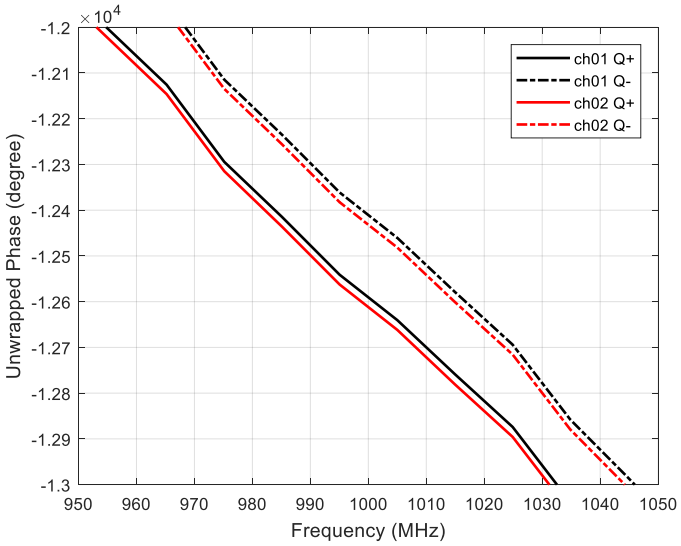

Figure 3.9: The unwrapped phases of two parallel MZMs are measured around 1 GHz when the DC bias is set to positive and negative quadrature bias.

Table 3.2: Measured pathlength of two optical channels.

	CH01 Q+	CH01 Q-	Ch02 Q+	CH02 Q-
Phase delay @ 1GHz	12591°	12411°	12612°	12432°
RF length	7.147 m	7.045 m	7.159 m	7.057 m

With proper RF and optical pathlength match, the phase difference between the primary and the secondary channel is determined by the bias condition of MZMs. With one MZM biased at positive quadrature and the other biased at negative quadrature, the 180-degree is achieved. The stability of the phase difference is maintained by a commercial electro-optic modulator controller which is based on feedback control using a photodetector to monitor the output of the MZM.

To further investigate the influence of improper pathlength match, a comparison test is conducted as shown in Figure 3.10. There are three configurations, i.e., pathlength matched, additional 2π phase added to the primary channel, and additional 2π phase

added to the secondary channel. The corresponding LTE signals detected on the photodetector are shown on the right, where significant spectrum regrowth is monitored when a 2π phase is added. The spectrum regrowth originates from the additional 2π pathlength because the 2π pathlength difference is frequency dependent.

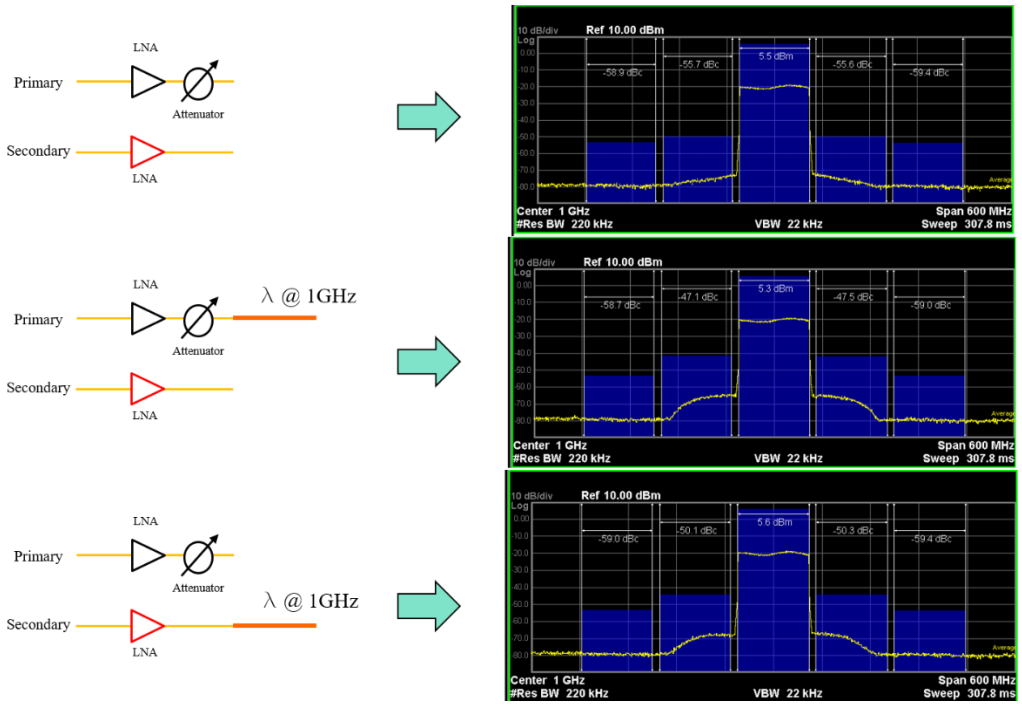

Figure 3.10: Three RF spectra correspond to different phases between the primary and the secondary MZM: a) 0, b) 2π, c) -2π

3.5 LTE signal transmission over linearized link

Significantly, more spectral bands are being opened for 5G wireless communication by the Federal Communications Commission (FCC). As a case in point, 5G is deployed in high-band, mid-band, and low band, which includes frequencies around 28 GHz, 39 GHz, and 64 GHz. The first 5G spectrum auction was held by the

FCC for the 28GHz (27.5-28.35GHz) and 24 GHz (24.15-24.45,24.75-25.25GHz) bands in 2018. The upper 37GHz, 39GHz, and 47 GHz bands could be available in 2019. With balanced coverage and capacity characteristics, mid-band becomes a target for 5G, and 844 MHz available instantaneous bandwidths are deployed at 2.5GHz, 3.5GHz, and 3.7-4.2GHz. The FCC is also acting to improve the use of low-band spectrum for 5G service for wider coverage, with targeted frequencies over a few hundred MHz bands.

In order to validate the approach and investigate its potential application in RF signal transmission for 5G wireless communication systems, which represents the unique contribution of this work, a setup is built and tested using LTE signals with various bandwidths. In this setup, an intermediate frequency of 1 GHz is used to study 5G low-band applications.

3.5.1 Generation of LTE signals

As illustrated in Figure 3.11, optical signals are generated by two continuously tunable lasers with the carrier frequencies set to 193.30 THz and 193.35 THz respectively, for the nominal difference of 50 GHz. The photodetector has a bandwidth of 20 GHz and therefore does not respond to carrier intermodulation in the optical domain. The RF signal is generated by a digital-to-analog converter (DAC) from Texas Instruments (DAC34SH84), which is a 16-bit DAC with a sampling rate of 1.5 Giga-samples per second (GSPS). The DAC is also capable of incorporating an intermediate frequency of up to 4 GHz using onboard RF mixers. However, the output power of the DAC is fixed, and the signal to noise ratio (SNR) drops as signal bandwidth increases.

An LTE signal of 20 MHz bandwidth with 153.6-MHz sampling rate is used as the initial baseband waveform. Based on this waveform, LTE signals with different

bandwidths are generated by changing the sampling rate of the DAC. The onboard sampling rate is set to 153.6 MHz, 307.2 MHz, 614.4 MHz, 1228.8 MHz, and 1489.92 MHz, to yield LTE signals with 10 MHz, 20 MHz, 40 MHz, 80 MHz, and 97 MHz bandwidth, respectively. The maximum bandwidth is limited to 97 MHz because the sampling rate of the DAC cannot exceed 1.5 GSPS.

The RF signal generated by the DAC is then split by an RF power divider to feed the primary and secondary channels, however, in so doing the RF power drops from -7 dBm to -13.5 dBm due to the insertion loss of the RF power divider. To improve the modulation sideband power as well as the link gain, RF low-noise amplifiers are introduced to increase the modulation depth to the required level. For the primary channel, a 20-dB gain, high-linearity low-noise amplifier (LNA) with 40 dBm third-order output intercept point (OIP3) at 1 GHz is used to preserve signal fidelity. For the secondary channel, a similar LNA with 21.5dB gain is used. As the RF inputs of two LNAs are very low, both LNAs work in the linear region and the link's IMD3 is dominated by the MZMs because of the high modulation depth.

The optical power ratio is controlled directly by two lasers (ID Photonics CoBrite-DX1), while the RF power ratio is maintained by inserting a tunable RF attenuator into the primary channel. As shown in the optical spectrum-illustration insets in Figure 3.11, the primary channel has a stronger carrier and a weaker sideband compared with the secondary channel. The parallel MZMs are controlled separately by two external bias controllers, which use feedback loops to ensure the respective positive and negative quadrature biases are maintained. For more precise and easy control on the π-phase shift, a pair of true time delay lines are used. The optical signals are then combined and amplified by an EDFA to improve the link gain and to increase the

generated RF power. In the following experiments, the optical power ratio is set to be 10 dB while the RF power ratio is 6.7 dB, which is consistent with Equation 3.27. Compared to conventional PINs/APDs, the high-speed MUTC photodetector can handle hundreds of milliwatts optical power corresponding to 100 mA photocurrent, therefore producing much higher RF power [101]. With the help of MUTC photodetectors, the DC photocurrent can be set to 60 mA to demonstrate the link's high RF output.

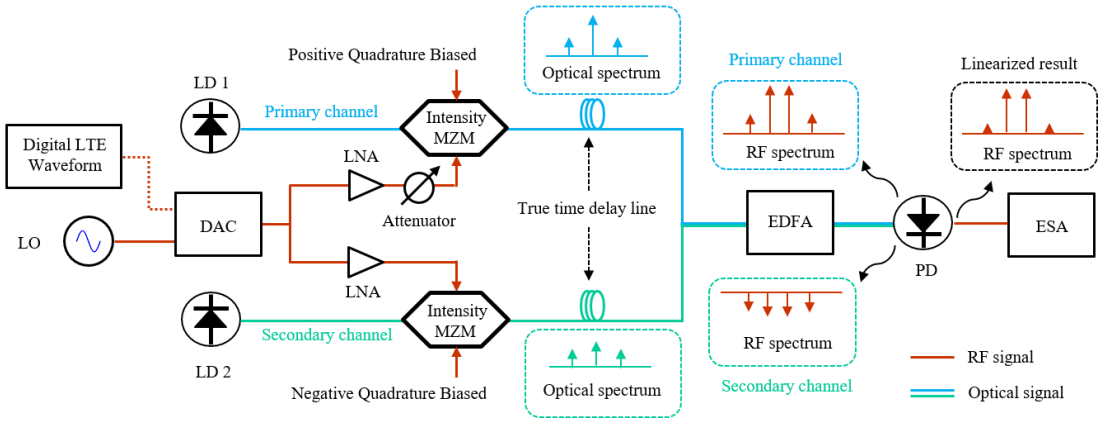

Figure 3.11: Photonic RF generation based on dual parallel modulator configuration. Attenuator is used to control the RF power ratio whereas the true time delay line is used to precisely tune the π-phase difference between the two channels to suppress IMD3 and improve ACLR. DAC: digital to analog convertor, LNA: low noise amplifier, LO: local oscillator.

3.5.2 Experiment result and analysis

Figure 3.12 shows the experimental results in the form of spectrum analyzer traces obtained for 10-MHz and 80-MHz LTE signals with a 1-GHz IF carrier. Without compensation, i.e., using the primary channel only, we can clearly see spectral regrowth in adjacent channels. Measured ACLR1 is around -44 dBc in both (a) and (c), which barely misses the -45 dBc requirement for radio base stations [5]. As seen in (b) and (d),

ACLR1 with compensation is improved by 19.2 dB and 11.8 dB, respectively, for LTE signals with 10-MHz and 80-MHz bandwidths. There is a small 2-dB link gain penalty in both cases, but the total fundamental RF power is maintained at 5 dBm. As the RF input on the primary MZM is 0 dBm, the link gain is 5 dB, which can be further improved by increasing the photocurrent. Notably, ACLR1 is the major concern in that it represents the strongest intermodulation terms that are closest to the channel of interest. The second adjacent channel leakage ratio (ACLR2) indicated in these measurements is attributed to the fifth order intermodulation distortion.

To investigate the linearization technique for broadband applications, LTE signals with various bandwidths are tested. It is worth pointing out that ACLR1 and ACLR2 generally degrade with the increase of signal bandwidth even if there is no IMD3. When generating LTE signals with different bandwidths, the integrated RF power over entire RF spectrum remains the same because the DAC has a fixed output power. Thus, when the bandwidth of LTE signal increases, the power spectrum density (PSD) decreases accordingly, resulting in a degradation of SNR or ACLR. This phenomenon adds complexity to the result, so the ACLR1 at MZM input is used as the baseline which is illustrated as a green dashed line in Figure 3.13.

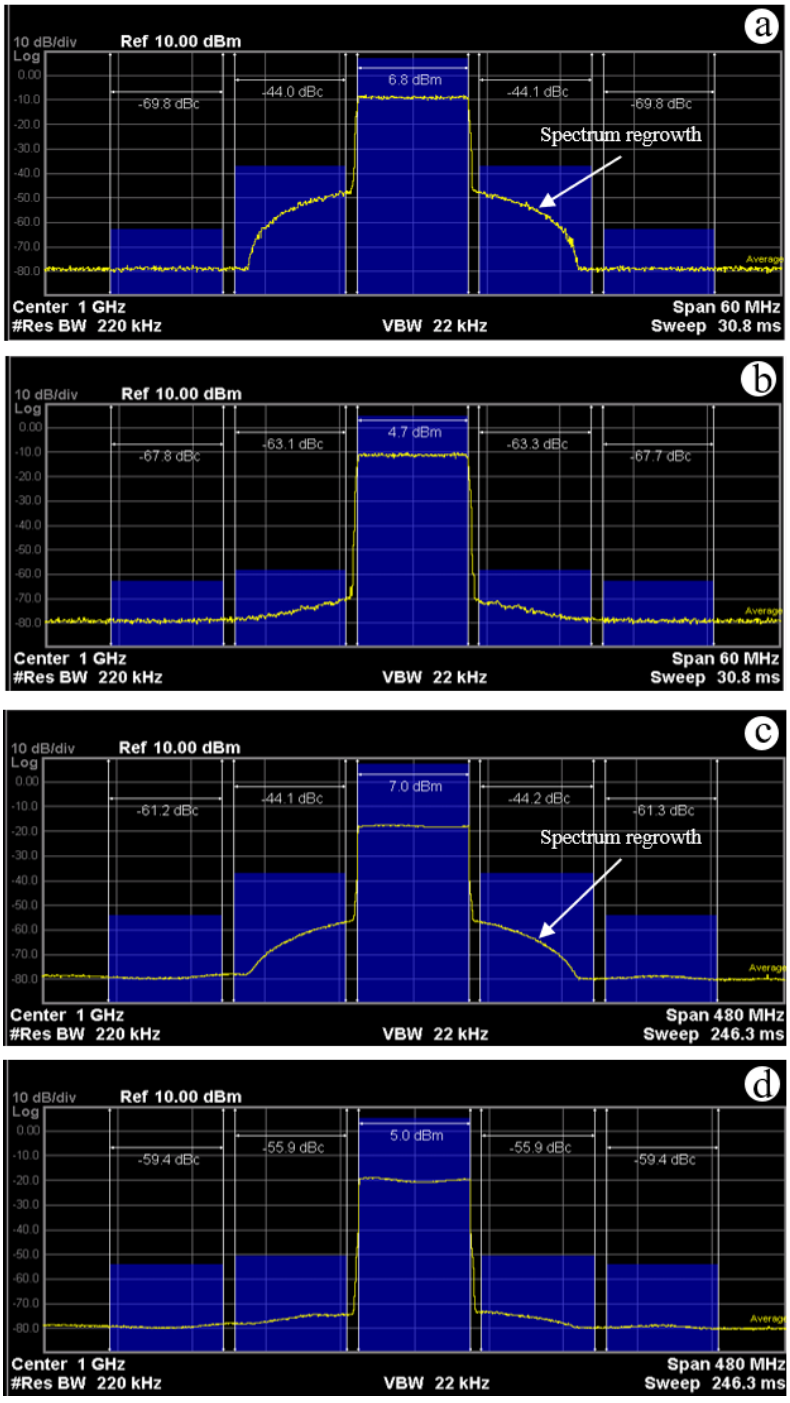

Figure 3.12: LTE signals with an intermedium frequency of 1 GHz are generated when DC photocurrent is 60 mA. (a) Without compensation @ BW = 10 MHz; (b) With compensation @ BW = 10 MHz; (c) Without compensation @ BW = 80 MHz; (d) With compensation @ BW = 80 MHz.

A range of tests were performed using the LTE signals generated by the AWG as input while the output is monitored on a MUTC photodetector at 60 mA photocurrent, see Figure 3.13 for the test results. The noise floor of this link is dominated by the relative intensity noise (RIN) of the laser which is proportional to the square of photocurrent. ACLR1 without compensation remains the same around -44 dBc for different bandwidths mainly because of the strong IMD3 introduced by high modulation depth. When a secondary channel is used to cancel the IMD3, ACLR1 is improved by 19.2 dB for a 10 MHz LTE signal, 15.4 dB for a 40 MHz LTE signal, and 9.3 dB for a 97 MHz LTE signal, at the cost of approximately 2 dB power penalty. Notably, ACLR improvement gets smaller when the input signal bandwidth increases. This can be explained by the ACLR degradation from the DAC. As the DAC outputs constant RF power, the signal-to-noise ratio (SNR) drops if the signal bandwidth is increased. We can see from Figure 3.12 that the spectrum regrowth in both (b) and (d) is minimized even if the ACLR improvements are different. As a result, the reduction of ACLR1 improvement is a limitation of the implementation but not the technique. With a better DAC, the improvement of 19.2 dB would be the same for LTE signals with different bandwidths. Compared with the ACLR1 at the MZM input, the ACLR1 with compensation is degraded by approximately 7-11 dB. There are a few factors that account for this degradation: (1) quadrature DC bias deviation, (2) laser power fluctuation, (3) optical or RF pathlength mismatch, (4) reduced SNR due to the DAC's limitations.

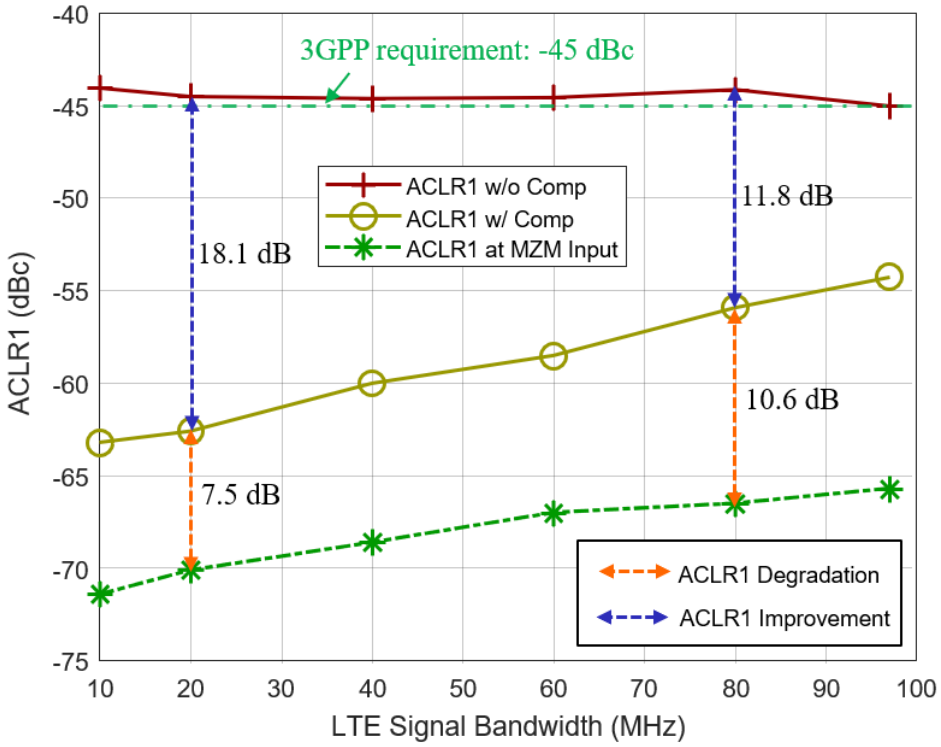

Figure 3.13: LTE signals with different bandwidths are tested using parallel modulator configuration; data is measured at photodetector with/without IMD3 compensation. ACLR1 improvement denotes the ACLR1 gained by suppressing the IMD3. ACLR1 degradation denotes the SNR loss attributed to link noise figure.

Although the IMD3 cannot be completely suppressed, the ACLR1 of this linearized link is still 10 dB above the 3GPP minimum requirement (44.2 dB), while ACLR1 without compensation is at the borderline of this requirement. For comparison, the ACLR1 reported in a 60-GHz microwave transmitter for a 20 MHz LTE signal is -50 dBc [25], and the ACLR1 measured for a 20 MHz LTE signal is -56.5 dBc using digital predistortion [11]. According to the data presented in this section, it is confirmed that this two-wavelength MZM linearization technique can be used to generate and transmit LTE signals with both high fidelity and high power, e.g., -63.2 dBc and

4.7 dBm for a 10 MHz LTE signal at 60 mA photocurrent. The signal at the output of the photodetector fully meets the 3GPP requirement on ACLR and this technique can be used in analog photonic links for telecommunication.

3.6 Summary

This chapter summarizes existing MZM linearization techniques using two wavelengths. Then the differences between optically coherent and optically incoherent linearization technique are compared. Based on the incoherent linearization, a system including two MZMs in parallel, driven by two separate lasers to suppress the IMD3 and improve the linearity of photonic RF signal generation, is proposed and investigated. A theoretical model is developed to investigate the optimum conditions to get full suppression on IMD3. MATLAB simulations further demonstrated and verified how IMD3 is suppressed at different RF and optical power ratios.

Later, a photonic link is built to investigate this two-wavelength linearization experimentally. Both RF pathlength and optical pathlength are matched with the help of a network analyzer, so the 180-degree phase can be secured by biasing two MZMs at opposite quadratures. Lastly, LTE signals with bandwidth from 10 MHz to 97 MHz are generated using a 16-bit DAC and transmitted by the linearized analog photonic link. Compared to a conventional MZM configuration, ACLR1 is improved by approximately 9-19 dB (depending on the signal bandwidth) in the parallel MZMs configuration using two-wavelength linearization technique, at the cost of 2 dB power penalty.

Chapter 4

TWO-POLARIZATION MZM LINEARIZATION

Similar to the two-wavelength Mach-Zehnder modulator (MZM) linearization technique, the two-polarization linearization technique described in this chapter is also based on optically incoherent combination. However, this technique has a reduced cost because only one laser is used.

In this chapter, the existing two-polarization MZM linearization techniques are introduced, and then an MZM linearization technique using a polarization beam combiner (PBC) is proposed followed by theoretical analysis. Later, a two-tone test is conducted to investigate the benefit from this two-polarization linearization where various link parameters are measured and compared. Lastly, LTE signal transmission over such a linearized link is tested. Significant ACLR improvement can be achieved using this two-polarization linearization technique.

4.1 Introduction

To avoid the stringent requirement on the power ratio and phase vibration in optically coherent linearization, optically incoherent linearization approaches using two different optical wavelengths have been investigated [93], [95], [102]. However, the two-wavelength approach requires two lasers, which increases overall cost and decreases spectral efficiency. As an alternative, an incoherent linearization approach, using two-polarizations has been proposed and investigated [103]–[105]. Haas presents a phase-modulated RF optical link with suppressed third-order intermodulation

distortion (IMD3) using two polarizations [103]. In his work, the anisotropic electrooptic coefficient of lithium niobate (LiNbO3) is used to simultaneously modulate two orthogonally polarized fields and two free-space linear polarizers are placed before and after the link to precisely control the optical power split or combine ratio to suppress IMD3. It was experimentally demonstrated that such configurations suppress third-order distortion to the point where the spurious-free dynamic range (SFDR) is limited by fifth-order nonlinearities. Using a similar concept, Masella presented a linearized optical single-sideband (SSB) MZM link with 15 dB SFDR improvement compared to a conventional MZM link [104]. More recently, Zhu presented a linearized link based on an integrated dual-polarization modulator, consisting of two *z*-cut $LiNbO_3$ MZMs, a PBC, and a polarization beam splitter (PBS). An adjustable polarization controller is placed in front of the modulator to control the optical power fed into the two parallel-MZMs. The unbalanced modulation indexes along with the two orthogonal polarizations are used to generate two RF signals that have different linear responses and equal third-order responses. Simulated results show 30.6 dB IMD3 suppression and 22 dB improvement of SFDR [105].

While the existing two-polarization approaches provide considerable improvement in SFDR, they all suffer from high power penalty which can be 11 dB compared to a conventional link. The power penalty is determined by the RF or optical power ratio where higher ratio gives lower power penalty. However, in the previous two-polarization linearized links, the RF power ratio is fixed at 1/3 in a $LiNbO_3$ modulator. In addition, the use of the free-space polarization controller may compromise the link's resistance to vibration and the convenience of electronic control.

In order to minimize the power penalty and eliminate the use of a free-space polarization controller, this chapter presents a linearized link based on optically incoherent combination where a fiber-based PBC and two MZMs operating in parallel are used. With the help of a polarization beam combiner, two modulated optical signals are coupled into the two orthogonal polarizations of a polarization maintaining (PM) fiber. In so doing, two independent links are formed before they arrive at a photodetector and their relative phase is independent of environment temperature or vibration.

4.2 Principle of two-polarization linearization

The schematic of the investigated link is shown in Figure 4.1. In this system, a highly linear-polarized optical carrier is generated by a packaged laser diode and launched into a PM fiber. The optical carrier is then split with controllable splitting ratio and fed into two parallel MZMs, namely the primary and the secondary MZM, see Figure 4.1. The primary MZM is used for data modulation while the secondary MZM is used to compensate nonlinear distortion. A tunable optical splitter is used to control the optical power ratio while a tunable RF splitter is used to tune the RF power splitting ratio. By properly adjusting optical and RF power splitting ratios, we can equalize the IMD3 in the two parallel MZMs.

Meanwhile, the relative phase in the generated IMDs between two MZMs may be adjusted independently by applying different DC bias voltage. In particular, a π-phase shift may be obtained by biasing the two MZMs at opposite quadratures. The two modulated outputs are orthogonally combined into the slow and fast axes of a PM fiber by means of a PBC. The combined optical signals are fed into a single-mode Erbium-doped fiber amplifier (EDFA) to equally amplify both polarizations, and the EDFA output is launched into a single-mode fiber for signal transmission.

At the receiving end of the optical link, the optical fiber is coupled to a high-speed modified uni-traveling-carrier (MUTC) photodetector. Since the two optical signals are orthogonal to one another, they are independently detected by the photodetector so as to produce two RF signals, which combine at the output. Since the two RF signals are out-of-phase, they combine destructively. To maximally suppress the IMD3, the RF and optical splitters are adjusted to produce identical amplitudes of the IMD3; biasing the MZMs in opposite quadratures ensures that the signals are out of phase. In addition, an optimization is conducted to realize maximum IMD3 suppression but minimum power penalty in the recovered RF signal.

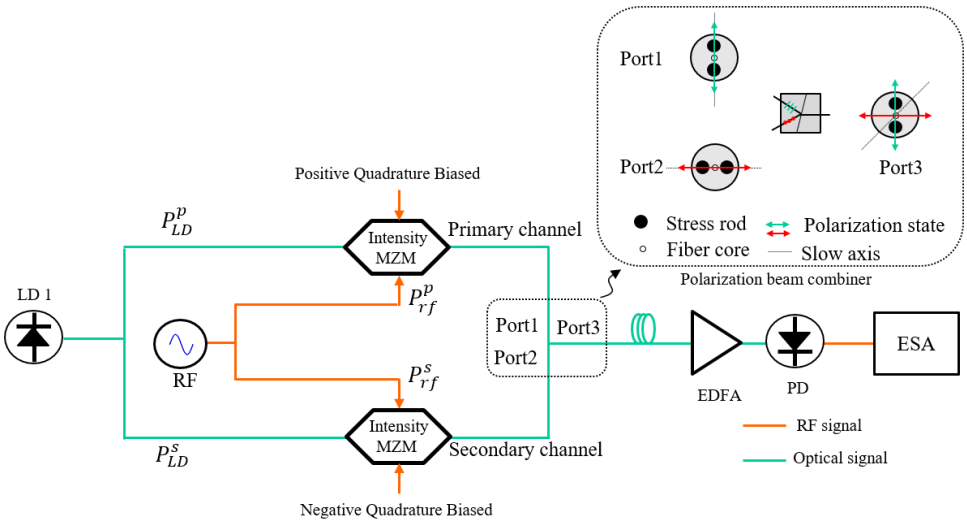

Figure 4.1: A linearized microwave photonic link assisted by fiber-based polarization beam combiner. LD: Laser diode, EDFA: Erbium doped fiber amplifier, PD: photodetector, ESA: Electrical spectrum analyzer.

To provide a quantitative measure of IMD3 suppression, the link is formally analyzed. First, since the electro-optic modulators are configured as push-pull MZMs,

the electric fields in the primary and secondary channels before the optical combiner, see Figure 4.1, can be expressed as:

$$\begin{cases} E_p = E_{LD}^p e^{j\omega_0 t} \cos\left(\frac{\varphi_{dc}^p + \varphi_{rf}^p}{2}\right) \\ E_s = E_{LD}^s e^{j\omega_0 t} \cos\left(\frac{\varphi_{dc}^s + \varphi_{rf}^s}{2}\right), \end{cases} \tag{4.1}$$

where $E_{LD}^p e^{j\omega_0 t}$ and $E_{LD}^s e^{j\omega_0 t}$ are the electric fields of the optical source in the primary and secondary channels, φ_{dc}^p and φ_{dc}^s are the phases introduced by DC bias signals, whereas φ_{rf}^p and φ_{rf}^s are the modulation phases introduced by the RF drive signals that can be expressed as:

$$\begin{cases} \varphi_{rf}^p = \frac{\pi V_p^p v(t)}{V_{\pi\_rf}},\ V_p^p = k\sqrt{P_{rf}^p / Z_0} \\ \varphi_{rf}^s = \frac{\pi V_p^s v(t)}{V_{\pi\_rf}},\ V_p^s = k\sqrt{P_{rf}^s / Z_0}. \end{cases} \tag{4.2}$$

The RF signal powers fed into the modulators are P_{rf}^p and P_{rf}^s, $v(t)$ is the normalized time-domain waveform, and k is the factor to convert root mean square (RMS) voltage to peak voltage (V_p^p and V_p^s). As a result, the combined, time-dependent optical power before the erbium-doped fiber amplifier (EDFA) is:

$$P_{tot} = \frac{1}{2}\left[P_{LD}^s\left(1 + cos\left(\varphi_{dc}^s + \varphi_{rf}^s\right)\right) + P_{LD}^p\left(1 + cos\left(\varphi_{dc}^p + \varphi_{rf}^p\right)\right)\right]. \tag{4.3}$$

Given quadrature phase bias conditions $\varphi_{dc}^p = \frac{\pi}{2}$, $\varphi_{dc}^s = -\frac{\pi}{2}$, the total photocurrent on the photodetector is:

$$I_{RF} = \frac{1}{2}\mathcal{R}G_{EDFA}\left(P_{LD}^p + P_{LD}^s - P_{LD}^p sin\varphi_{rf}^p + P_{LD}^s sin\varphi_{rf}^s\right), \tag{4.4}$$

where $\mathcal{R}$ is the responsivity of the photodetector and G_{EDFA} is the gain of the EDFA. Taylor expanding the sine functions, and keeping only the fundamental and third-order terms, yields the RF photocurrent as:

$$I_{RF} = \frac{1}{2}\mathcal{R}G_{EDFA}\left(P_{LD}^{s}\left(\varphi_{rf}^{s} - \frac{\left(\varphi_{rf}^{s}\right)^{3}}{6}\right) - P_{LD}^{p}\left(\varphi_{rf}^{p} - \frac{\left(\varphi_{rf}^{p}\right)^{3}}{6}\right)\right). \quad (4.5)$$

To completely suppress the third-order intermodulation terms, $P_{LD}^{s} \cdot \left(\varphi_{rf}^{s}\right)^{3}$ and $P_{LD}^{p} \cdot \left(\varphi_{rf}^{p}\right)^{3}$must be equal. Since the RF modulation phase is linearly proportional to the square root of input RF power, as shown in Equation 4.2, the optimum optical and RF power relationship to eliminate the IDM3 completely is

$$\left(\frac{P_{LD}^{p}}{P_{LD}^{p}}\right)^{2} = \left(\frac{P_{rf}^{s}}{P_{rf}^{p}}\right)^{3}. \quad (4.6)$$

Note that Equation 4.6 allows non-zero linear response as long as P_{LD}^{s} differs from P_{LD}^{p}. The above equation can also be expressed in decibel scale:

$$2 \cdot \Delta P_{opt}\,[dB] = 3 \cdot \Delta P_{rf}\,[dB]\ , \quad (4.7)$$

which can be used as a guide to balance the IMD3 of the two MZMs.

In this section we report on a two-tone test carried out using the linearized link to demonstrate IMD3 suppression and link performance improvement. In addition, a subset of the two-tone test is conducted at different photocurrents to compare the gain, noise figure, (third-order intercept point) OIP3, and SFDR between a conventional intensity-modulation direct-detection (IMDD) link and this linearized link. Lastly, LTE signals of various bandwidths are transmitted over this two-polarization linearized link to investigate its potential applications in telecommunication, where adjacent channel leakage ratio (ACLR) is used as the figure of merit [106].

4.3 Two-Tone Test

The experimental setup for a two-tone test is depicted in Figure 4.2. A 100-mW tunable laser with high polarization purity is used as optical source. The generated optical signal is delivered by a PM fiber to maintain its initial polarization state. A 50/50

power splitter is used to split the optical signal and a variable optical attenuator (VOA) is inserted before the secondary MZM to precisely control the optical power ratio between the two MZMs. Two single-tone sinusoidal signals are generated by two RF synthesizers (National Instrument QuickSyn Synthesizer). The generated RF signals are combined and then split to drive the two MZMs. A tunable RF attenuator is placed before the primary MZM to achieve an asymmetric RF drive. The maximum allowed power of the RF input is determined by the RF halfwave voltage (V_{π_rf}) of the MZMs because over-drive can lead to signal clipping distortion. Using commercial MZM bias control boards with feedback loops, the primary and secondary MZMs are biased at positive and negative quadratures, respectively, to achieve a 180-degree phase difference. However, the phase may be tuned if the optical or RF pathlength between two channels differ. In this test, an RF-pathlength-match cable is placed before the secondary MZM to compensate the additional path length from the insertion of an RF attenuator. The optical pathlength also needs to be matched to maintain the 180-degree phase difference. The pathlength difference before the MZM, such as the VOA on the secondary channel, is not considered because it happens prior to the RF modulation. However, the optical path length is critical after the MZM. To better control the 180-degree phase, two optical true time delay lines are inserted before the PBC to provide an additional pathlength adjustment.

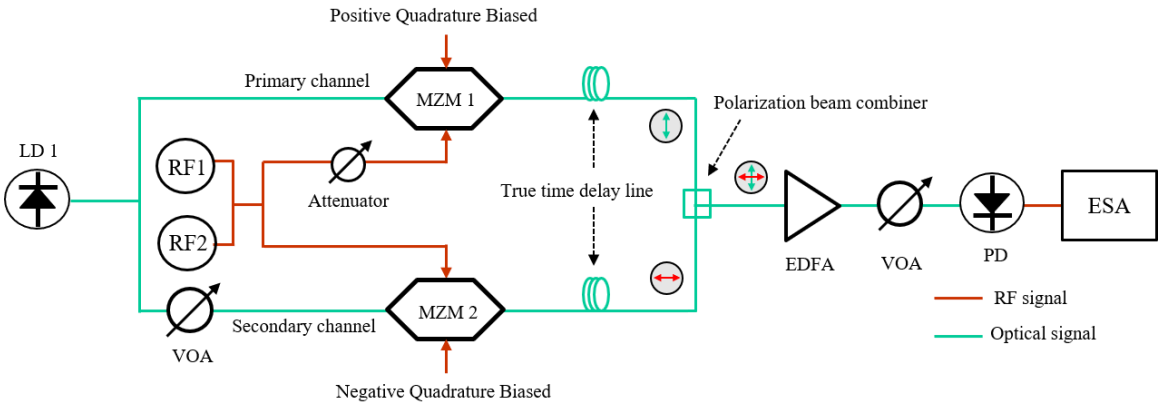

Figure 4.2: Schematic diagram of a two-tone test on the linearized link. LD: laser, VOA: variable optical attenuator, ESA: electrical spectrum analyzer.

In this two-tone test, the laser wavelength is set to 1557.62 nm and the power is set to 100 mW. As two RF signals are 993 MHz and 997 MHz, respectively, the third order intermodulation can be observed at 989 MHz ($2f_1 - f_2$) and 1001 MHz ($2f_2 - f_1$). Following Equation 4.6, the optical and RF power splitting ratio equal to 3:2 is selected for the best IMD3 suppression. Accordingly, the optical powers of the primary and the secondary channels are set to 16 dBm and 6 dBm with 10 dB imbalance, whereas the RF powers are set to -1.0 dBm and 5.7 dBm to yield 6.7 dB imbalance. With the help of the PBC, the modulated optical signals from the two channels become orthogonal. They are amplified equally by a single-mode EDFA which produces 27 dBm optical power at the output. Lastly, the amplified optical signals are controlled by a variable optical attenuator and feed to an MUTC photodetector for data recovery.

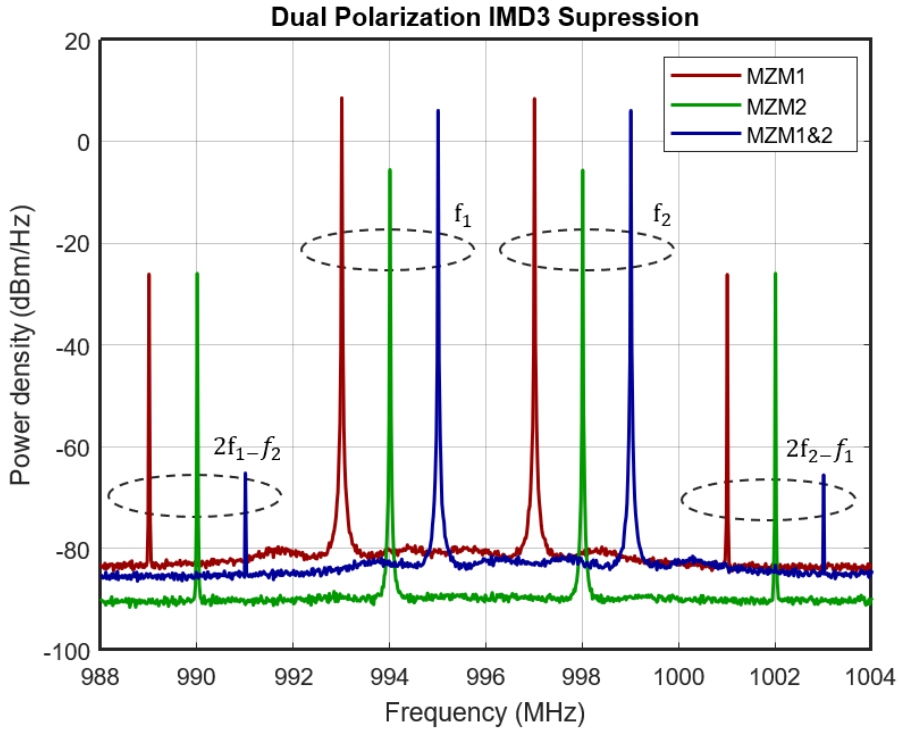

Figure 4.3: RF Spectra detected on the photodetector at 60 mA photocurrent. Third order distortions on the primary and secondary channel are balanced. About 39.2 dB suppression is observed when two optical signals are combined.

To better illustrate the IMD3 suppression, RF spectra detected on the photodetector at different conditions are shown in Figure 4.3. The primary spectrum (MZM1) is detected when no RF signal is fed to the lower MZM, the secondary spectrum (MZM2) is detected when no RF signal is fed to the upper MZM, while combined spectrum (MZM1&2) is detected when both MZMs are driven. The secondary and combined spectra are shifted by 1 MHz and 2 MHz respectively for easier comparison. As is shown in Figure 4.3, IMD3s at 989 MHz and 1001 MHz are equal at MZM1 and MZM2, but they are suppressed by 39.2 dB after they are combined

with 180-degree phase shift. With significant improvement in IMD3 suppression, there is only 2.3 dB power penalty for the fundamental frequencies. The RF power penalty can be improved if both the RF and optical power ratios between the two MZMs are increased. However, there are constraints that limit further increase of the power splitting ratio: 1) the maximum allowed optical power of the electro-optic modulators, typically 100 mW for most commercial MZMs; 2) the RF inputs are limited by the half-wave voltage of the electro-optic modulators to avoid signal clipping.

4.4 Link Parameter Characterization

The figures of merit to determine the performance of an analog photonic link include gain, noise figure, output third-order intercept point (OIP3) and SFDR. All these parameters can be measured and calculated based on a two-tone test. As shown in Figure 4.4, the test is performed at ~1 GHz, with $f_1 = 993$ MHz and $f_2 = 997$ MHz, and the input RF signal power varied from -5 dBm to 10 dBm. Fundamental and IMD3 are measured accordingly for the different power levels while the noise floor is measured when the RF input is turned off.

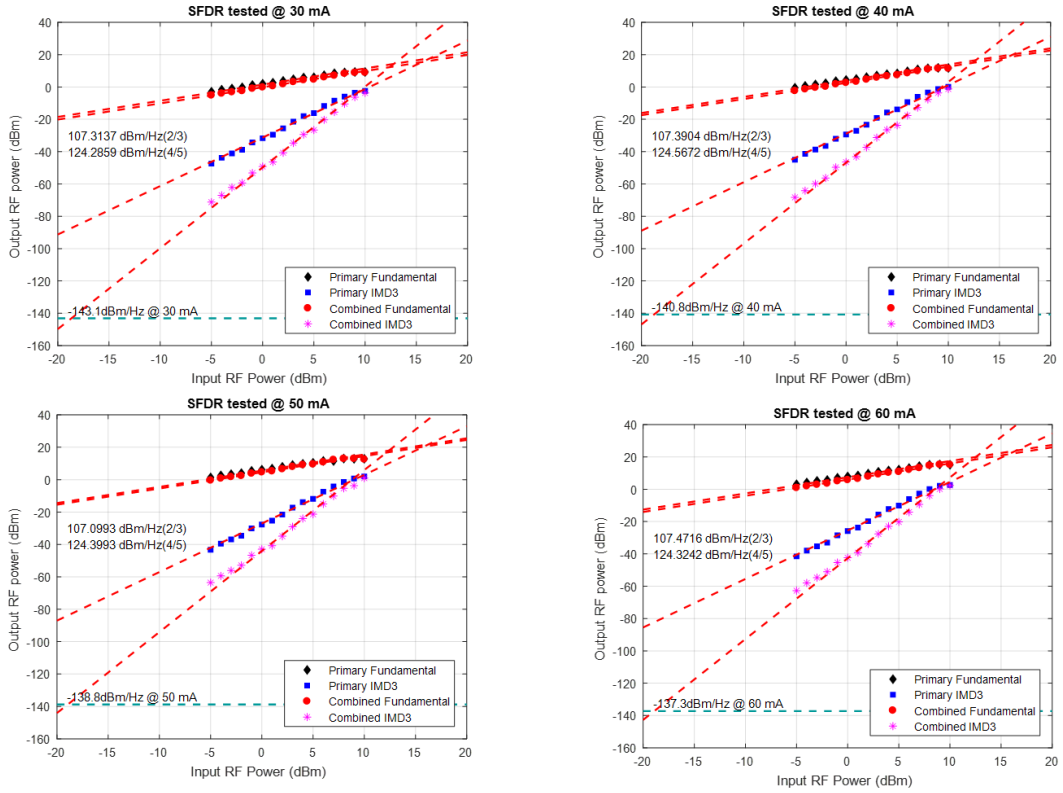

Figure 4.4: Two-tone test at 1 GHz. Black diamonds correspond to linear response without compensation, blue squares correspond to IMD3 without compensation, red dots correspond to linear response with compensation, magenta stars correspond to IMD3 with compensation, and the green dashed line at the bottom represents link's noise floor.

4.4.1 Gain

The gain of an external intensity modulation with direct detection (IMDD) link is given in [107]. If the modulator is biased at quadrature, the gain can be estimated using:

$$\mathrm{G[dB]} = -22.1 + 20\log\left(\frac{I_{dc}[mA]}{V_{\pi}[V]}\right), \tag{4.8}$$

where I_{dc} is the photocurrent and V_{π} is the half-wave voltage of the MZM. As V_{π} of the modulator under test is 2.0 V at 1 GHz, the calculated gain of the a conventional IMDD

link is listed in Table 4.1. On the other hand, the link gain can also be calculated using the measured data from Figure 4.4 and these results are listed in Table 4.1 as well. The measured gain of the uncompensated link matches well the result calculated using Equation 4.8, where the measured gain of the compensated link is about 1.1~1.7 dB lower. With the help of an EDFA and a high-power MUTC photodetector [101], this linearized link has 6 dB gain at 60 mA photocurrent.

Table 4.1: Link gain at different photocurrents

	30 mA	40 mA	50 mA	60 mA
IMDD (Calculated)	1.4 dB	3.9 dB	5.9 dB	7.4 dB
W/o Compensation （Measured）	1.5 dB	3.9 dB	5.6 dB	7.7 dB
W/ Compensation （Measured）	-0.1 dB	2.6 dB	4.5 dB	6.0 dB

4.4.2 Noise Figure

According to [107], the noise figure of an analog photonic link at room temperature (290 K) can be calculated using:

$$NF(dB) = 174 + N_{out}[dBm/Hz] - G(dB) \ , \tag{4.9}$$

where N_{out} is the total output noise power spectral density and G is gain of the link. With N_{out} and G already known, the measured noise figures of both compensated and uncompensated link can be calculated, see Table 4.2. On the other hand, the noise figure of an ideal conventional IMDD link biased at quadrature can be calculated using [107]:

$$NF(dB) = 196.1 - 20log\left(\frac{I_{dc}[mA]}{V_{\pi}[V]}\right) + N_{out}\left[\frac{dBm}{Hz}\right] . \tag{4.10}$$

Given I_{dc} and V_{π}, the noise figure for IMDD link can be calculated and is also listed in Table 4.2. According to this table, the noise figure of the link without compensation behaves in a way similar to a conventional IMDD link while the linearized link has 1.0~1.7 dB higher noise figure. Based on Equation 4.9, the increase in the noise figure is found to be due to the decrease of link gain. The noise figure can be improved by using a balanced photodetector for detection or by exploiting the low bias technique [108].

Table 4.2: Noise figure at different photocurrents

	30 mA	40 mA	50 mA	60 mA
IMDD (Calculated)	29.5 dB	29.3 dB	29.3 dB	29.2 dB
W/o Compensation （Measured）	29.4 dB	29.3 dB	29.7 dB	29.0 dB
W/ Compensation （Measured）	31.0 dB	30.6 dB	30.7 dB	30.7 dB

4.4.3 OIP3 and OIP5

As shown in Figure 4.4, in the compensated link, the slope of the intermodulation-product power as a function of the input power changes from 3 to 5, and the link then becomes fifth order limited. The third order intercept point of a quadrature-biased conventional link is given in [107] as:

$$OIP3[dBm] = -13 + 20log(I_{dc}[mA]) . \quad (4.11)$$

The OIP3 estimated using Equation 4.11 for the IMDD link and measured for the un-compensated link as well as the OIP5 for the compensated link are given in Table 4.3. According to the table, the measured OIP3 of the uncompensated link matches well with the simulated results while the intercept point of a compensated link

is ~5 dB lower. Although the OIP5 of the linearized link is lower than the OIP3 of a conventional link, the linearized link has lower intermodulation for different levels of RF inputs especially for the low range, see Figure 4.4. Hence, the performance of the linearized link is not degraded even with a lower fifth-order output intercept point.

Table 4.3: OIP3 and OPI5 at different photocurrents

		30 mA	40 mA	50 mA	60 mA
OIP3	IMDD (Calculated)	16.5 dBm	19.0 dBm	21.0 dBm	22.6 dBm
OIP3	W/o Compensation （Measured）	17.9 dBm	20.3 dBm	21.8 dBm	24.4 dBm
OIP5	W/ Compensation （Measured）	12.3 dBm	14.9 dBm	16.7 dBm	17.3 dBm

4.4.4 SFDR

According to [107], if bias current I_{dc} and spectral noise density N_{out} are known, the third order spurious-free dynamic range of an IMDD link can be calculated using:

$$SFDR_3\left[dB \cdot Hz^{\frac{2}{3}}\right] = -8.7 + \frac{40}{3} log(I_{dc}[mA]) - \frac{2}{3} N_{out}\left[\frac{dBm}{Hz}\right] . \qquad (12)$$

Beside this numerical approach, SFDR can also be obtained by curve fitting which is illustrated in Figure 4.4. As shown in Table 4.4, the SFDRs calculated using Equation 4.12 (conventional IMDD link) match well those obtained by curve fitting (measured without predistortion) whereas SFDR is improved by 17 dB in the linearized link (measured with predistortion).

Table 4.4: SFDR at different photocurrents

	30 mA	40 mA	50 mA	60 mA
IMDD (Calculated)	106.4 $dB/Hz^{2/3}$	106.5 $dB/Hz^{2/3}$	106.5 $dB/Hz^{2/3}$	106.5 $dB/Hz^{2/3}$
W/o Compensation （Measured）	107.3 $dB/Hz^{2/3}$	107.4 $dB/Hz^{2/3}$	107.1 $dB/Hz^{2/3}$	107.5 $dB/Hz^{2/3}$
W/ Compensation （Measured）	124.3 $dB/Hz^{4/5}$	124.6 $dB/Hz^{4/5}$	124.4 $dB/Hz^{4/5}$	124.3 $dB/Hz^{4/5}$

According to Figure 4.4, link's spectral noise density rises from -143.1 dBm/Hz to -137.6 dBm/Hz when the photocurrent increases from 30 mA to 60 mA. At the same time, the linear response increases by 6 dB and, as a result, SFDR remains unchanged. The independence of SFDR from the photocurrent indicates that, in this case, the link is RIN limited.

To summarize, the link parameters of a quadrature biased IMDD link are calculated, measured, and compared to that of this dual-polarization linearized link. When the secondary MZM is not driven by an RF signal, the measured link parameters match well with an ideal quadrature biased IMDD link. Once the secondary MZM is used for IMD3 compensation, the link gain decreases by 1.1~1.7 dB, the noise figure increases by 1.0~1.7 dB, the output intercept point drops by ~5 dB, and the SFDR increases by 17 dB.

4.5 LTE signal transmission on two-polarization linearized link

Since the targeted application of the proposed link is next-generation wireless communications, the transmission of LTE signals with different instantaneous bandwidths is demonstrated. According to the Federal Communications Commission (FCC), high-band, mid-band, and low-band will be deployed in 5G [109]. The high-band is understood as 24 GHz and above, the mid-band spans roughly in the range from

2.5 GHz to 4.2 GHz, whereas the low-band covers frequencies of a few hundred MHz. In general, higher carrier frequencies can handle higher data rates but have smaller coverage compared because of free space loss. To probe the application of the linearized link in low-band 5G, LTE signals with different bandwidths are tested at an intermediate frequency (IF) of 1 GHz.

As illustrated in Figure 4.5, this setup is similar to the two-tone test setup except for the generation and feed of RF signals. Using a 16-bit digital-to-analog (DAC) converter (DAC34SH84), high-quality LTE baseband signals are generated. The baseband signals are then shifted to an intermediate frequency using onboard RF mixers (TRF3705) to 1 GHz, where the intermediate frequency is generated by an external RF synthesizer.

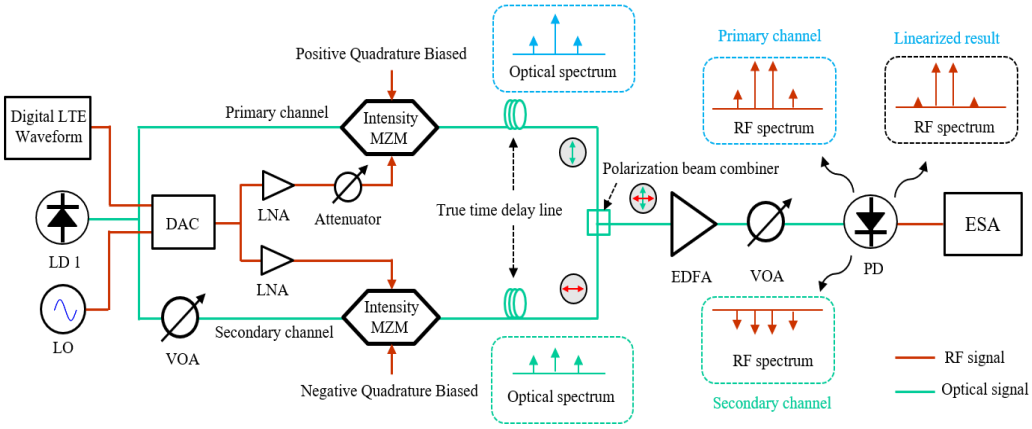

Figure 4.5: Illustration of LTE signal generation and transmission over an analog photonic link where the two-polarization linearization technique is used. LO: local oscillator, DAC: digital-to-analog converter.

The LTE signals are generated in the same way as described in chapter 3. An LTE waveform of 20 MHz bandwidth is defined in MATLAB with a sampling rate of

153.6 MHz. By controlling the DAC sampling rate, LTE signals with different bandwidths can be generated. For example, LTE signals with bandwidths of 10~97 MHz can be generated by setting the external clock (twice the sampling rate) to 153.6~1489.92 MHz.

An RF power divider is used to split the LTE signal and feed the upper and lower MZMs. Limited by the DAC, the generated LTE signal has an output power at -7 dBm. Moreover, the RF power divider adds 6 dB insertion loss which reduces the RF input at the MZM to -13.5 dBm. To get more RF power from the link, the modulation depth is increased by putting two low-noise amplifiers (LNAs) after the RF power divider. The LNA is not placed before the RF power divider because ACLR can degrade significantly due to the nonlinearity arise from the RF power divider. Two LNAs with 20 dB gain and 40 dBm OIP3 at 1 GHz are used. With -13.5 dBm input power, both LNAs operate at linear region. The distortion attributed to the MZM can be observed with the help of an electrical spectrum analyzer where the test is conducted in terms of ACLR.

As shown in Figure 4.5, the IMD3 can be equalized by adjusting the RF and optical power ratio using the variable RF and optical attenuators. The upper MZM provides the photodetector with the main signal while the lower MZM provides the photodetector with the IMD3 cancellation signal. The outputs from the two MZMs are combined with a PBC into orthogonal polarizations. To amplify two orthogonal optical signals equally, a single-mode EDFA is used. According to Equation 4.6, the optical and RF power ratio was set to 10 dB and 6.7dB to minimize IMD3. With the help of high-power MUTC photodetectors, the DC photocurrent can be set to 60mA an achieve 6-7 dB link gain.

For illustration, measured spectra using 10 MHz and 80 MHz LTE signals are given in Figure 4.6. The spectral regrowth is significant in (a) and (c) when the secondary channel is not used, resulting in ACLR1 at -46 dBc. As the ACLR requirement of LTE base station is -44.2 dBc [62], the link can barely meet the requirement even if RF input is slightly increased. In contrast, as seen in (b) and (d), ACLR1 in the linearized link reaches -65.6 dB and -59.5 dB, which marks an ACLR1 improvement by 19.6 dB and 13.0 dB for 10MHz and 80MHz LTE signal, respectively. This ACLR1 improvement comes at a small cost of ~2 dB power penalty for both cases.

Comparing (a) and (c) in Figure 4.6, the integrated fundamental power remains the same because the DAC operates at constant output power mode. The measured ACLR1s are similar because the first adjacent power is dominated by IMD3, which is similar in conventional IMDD link. However, ACLR2s have a 8.6 dB difference because the second adjacent channel is dominated by the noise floor. In this experiment, the noise floor is dominated by laser RIN noise and it remains the same if photocurrent is fixed at 60 mA. For example, the integrated RF power over the second channel increased by 9 dB when the bandwidth increased from 10 MHz to 80 MHz, which is consistent with the measured 8.6 dB difference. Comparing (b) and (d) in Figure 4.6, a similar phenomenon can be found for the fundamental power and ACLR2. However, the ACLR1 has about 6 dB difference because the first adjacent channel power is dominated by the noise floor and the residue of IMD3.

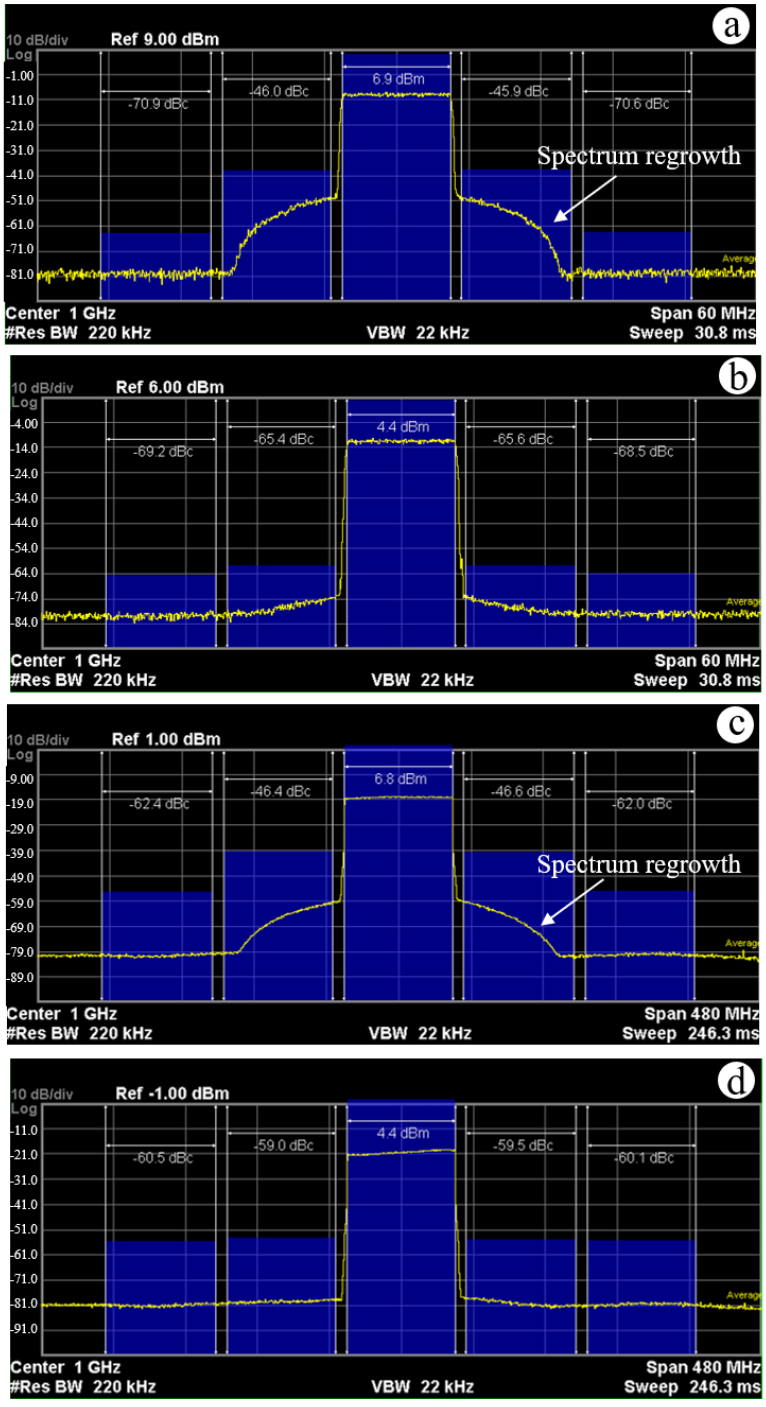

Figure 4.6: LTE signals with an intermediate frequency of 1 GHz are generated when DC photocurrent is 60 mA. (a) Without compensation @ BW = 10 MHz; (b) With compensation @ BW = 10 MHz; (c) Without compensation @ BW = 80 MHz; (d) With compensation @ BW = 80 MHz.

To investigate the linearization technique for broad bandwidth applications, LTE signals with various bandwidths are tested. Note that ACLR1 and ACLR2 degrades with the increase of signal bandwidth regardless of IMD3. When generating LTE signals with different bandwidths, the integrated RF power over the entire RF spectrum remains the same because the DAC has a fixed total output power. Thus, when the bandwidth of the LTE signal increases, the power spectrum density (PSD) decreases accordingly, resulting in a degradation of SNR or ACLR. This phenomenon adds complexity to the result, so the ACLR1 at the MZM RF port is used as the baseline and plotted in Figure 4.7 (a) as 'MZM input'.

As illustrated in Figure 4.7 (a), the ACLR1 remains the same at -46 dBc in conventional IMDD links when LTE signals with different bandwidths are used. In an unlinearized link, the integrated power in the first adjacent channel is dominated by IMD3 because it is much stronger than noise floor. As a result, the ACLR1 remains the same because the power spectrum density in the center and the first adjacent channel change at the same ratio when signal bandwidth is increased. In a linearized link, the integrated power in the first adjacent channel is determined by the residue of the IMD3 and the noise floor which have similar power levels. When the LTE signal bandwidth is increased, the power spectrum density drops accordingly in the center channel but drops slightly in the first adjacent channel because the noise floor remains unchanged. As a result, the ACLR1 degrades if the LTE signal bandwidth is increased as shown in Figure 4.7(a). When the third-order nonlinearity is compensated using a secondary channel, the ACLR1 is improved by 19.6 dB, 15.6 dB, and 11.8 dB for LTE signals with bandwidths of 10 MHz, 40 MHz, and 97 MHz, respectively. The tradeoff to get the linearized performance is ~ 2 dB power reduction.

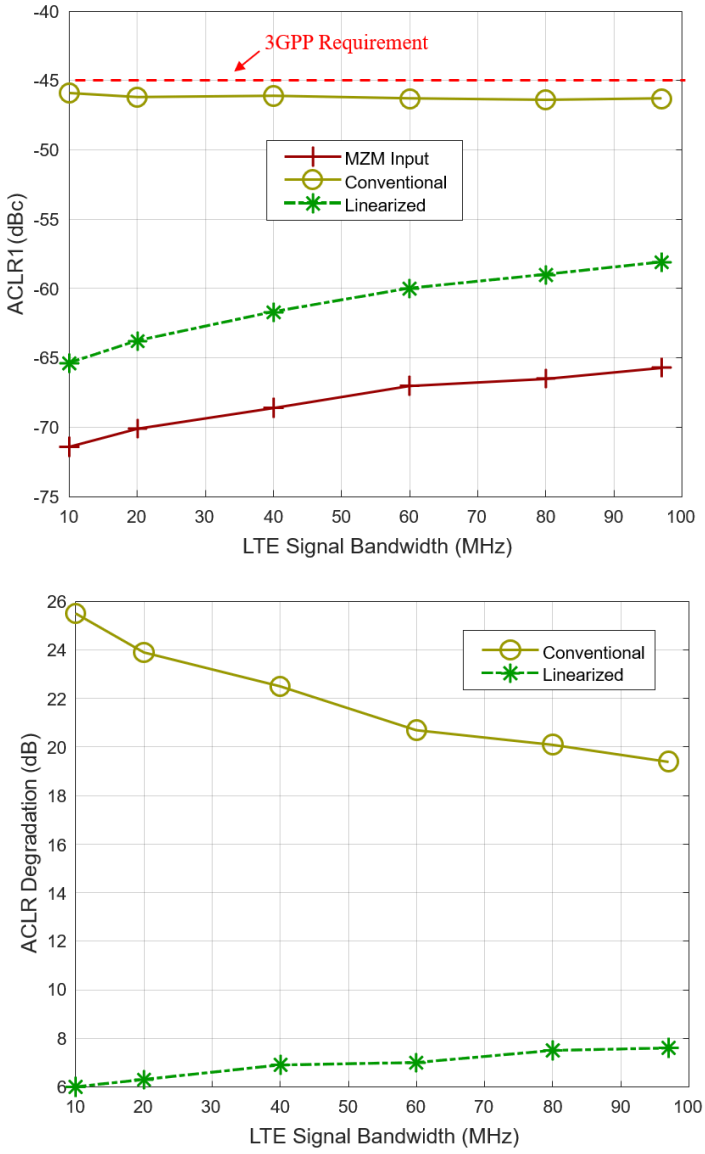

Figure 4.7: a) ALCR1 of LTE signals with different bandwidths are tested in a linearized link and an unlinearized link. b.) ACLR degradation which represents the ACLR difference between the MZM input and the photodetector output.

Although IMD3 is almost completely suppressed in both Figure 4.6 (b) and (d), the measured ACLR1 is quite different. Notably, it is not accurate to evaluate the linearization performance by utilizing ACLR1 only. As an alternative, the ACLR1 at the input of MZM is used as a reference, which is plotted in Figure 4.7 (a). To better illustrate the significance of the proposed linearization technique, the ACLR1 degradation between the IMDD link input and output are plotted in Figure 4.7 (b). For an LTE signal with various bandwidths, the ACLR1 is degraded by 19~26 dB in a conventional IMDD link while it is only degraded by 6~8 dB in a linearized link. The degradation is attributed to link's noise figure due to the laser RIN and the EDFA amplified spontaneous emission (ASE) noise.

According to Figure 4.7 (a), the measured ACLR1 in the proposed link ranges from -65 dBc to -58 dBc, which is over 13 dB better than the 3GPP minimum requirement. For comparison, Table 4.5 lists the performance of all three types of MZM linearization technique using a 20 MHz LTE signal. In the digital predistortion, the ACLR1 of generated signal is 6-7 dB worse than the optical linearization technique, but it gives the highest RF power at 60 mA photocurrent because the carrier to sideband power ratio is optimized. The two-wavelength and two-polarization linearization techniques have similar performances, and both have excellent ACLR and ~5 dB RF power.

Table 4.5: ACLR1 comparison for a 20 MHz LTE Signal

Frequency (GHz)	ACLR1 (dBc)	Power (dBm)	Photocurrent (mA)	Linearization method
1.06	-56.5	10.6	60	Digital predistortion
1.0	-62.6	4.8	60	Two wavelengths
1.0	-63.8	4.4	60	Two polarizations

4.6 Summary

A linearized analog photonic link, which is based on two separate MZMs in parallel and a polarization beam combiner, is presented. A mathematical model is derived to estimate the conditions whereby IMD3 can be suppressed by combining two out-of-phase RF signals. To verify this approach experimentally, a two-tone test is performed to demonstrate that IMD3 can be suppressed by 39.2 dB at the cost of 2.3 dB power penalty. A set of two-tone tests at 1 GHz is performed at various photocurrents to characterize the link in terms of gain, noise figure, OIP3, OIP5, and SFDR. It is experimentally verified that the measured results of the conventional link match well with the theoretical prediction. When the dual-polarization linearization technique is used, the SFDR is increased by about 17 dB at the cost of 1.1~1.7 dB gain penalty and 1.0~1.7 dB noise figure increase. Meanwhile, LTE signals with bandwidths of 10~97 MHz are delivered by this linearized link. With the dual-polarization linearization technique, ACLR1 is improved by 11.8~19.6 dB at the cost of approximately 2 dB power penalty compared to a conventional IMDD link.

Chapter 5

PHOTODETECTOR NONLINEARITY MEASUREMENT SYSTEM

When photodetectors are used for telecommunication, their intrinsic nonlinearities become very important. In this chapter, the methodologies of photodetector nonlinearity measurement are compared. According to the comparison, three-tone test using external modulation scheme seems to have the best accuracy. Consequently, a three-one photodetector nonlinearity test setup is integrated. After proper calibration, third-order output intercept point (OIP3) of modified uni-travelling carrier (MUTC) photodetectors is tested under different photocurrents, bias voltages, and frequencies.

5.1 Introduction

The nonlinear performance of a photodetector can be measured using two methods: two-tone test and three-tone test. The response of a two-tone test is illustrated in Figure 5.1 (a), where f_1 and f_2 are RF input. The high order harmonics and intermodulation above $2f_1$ introduce negligible influence on the fundamental signal because they are far away from the fundamental frequencies. However, the third-order intermodulation (IMD3) frequencies at $2f_1 - f_2$ and $2f_2 - f_1$ are so close to the fundamental signal that it cannot be filtered. In a two-tone test, the fundamental and IMD3 frequencies are monitored simultaneously and the OIP3 can be calculated according to Figure 1.10. Similarly, the three-tone test response is illustrated in Figure 5.1 (b), where there are nine IMD3 frequencies near the fundamental frequency. We

only monitor the frequencies at $f_1 + f_2 - f_3$, $f_1 + f_3 - f_2$ and $f_2 + f_3 - f_1$ because they include no second order responses, such as $2f_1$, $2f_2$, or $2f_3$.

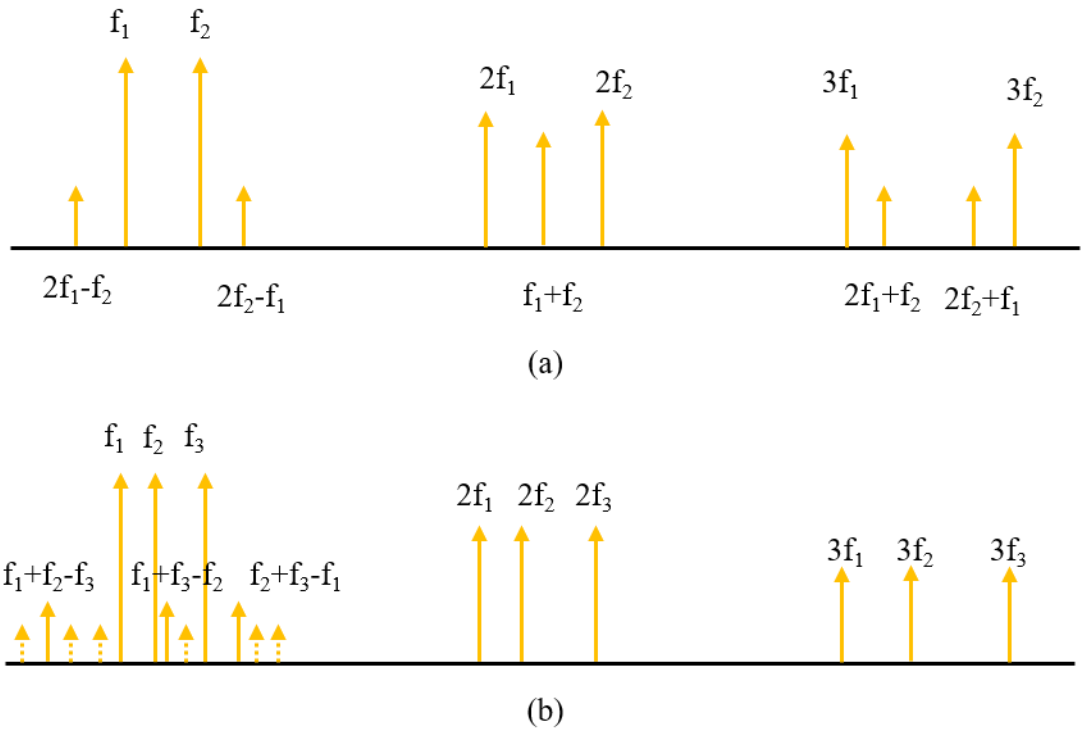

Figure 5.1: The frequency response of a nonlinear device using (a) two-tone test and (b) three-tone test.

There are three schemes to implement the above two methods to photodetector nonlinearity measurement, i.e., the frequencies can be generated by direct modulated optical source [110], [111], heterodyne source [112], or external modulation [113]. An illustration of those schemes is given in Figure 5.2, where both two-tone and three-tone test system are included. A five-laser two-tone test setup is shown in Figure 5.2 (a) where two pair of lasers are used to generate two frequencies while a fifth laser is used

to maintain constant optical power on the photodetector. This approach requires accurate control on laser wavelengths because of thermal drift. Laser wavelength locking technique is needed sometimes which further complicates the system. A four-laser three-tone setup is shown in Figure 5.2 (b) where three tones are generated by three directly modulated lasers and the fourth laser is used to maintain constant optical power on the photodetector too. The potential limiting factor of this approach is the nonlinearity arises from the laser. Lastly, a two-lase two-tone test system is shown in Figure 5.2 (c) where two frequencies are generated by two external modulators. Although this method has the simplest structure, the measurement accuracy is degraded by the nonlinear response from the electro-optic modulator. One of the most accurate and effective way to measure the photodetector nonlinearity is using three-tone test in combine with external modulation. This approach is reported in [113], where four lasers are used. Based on this approach, we optimized it, where the number of lasers and EDFAs is reduced.

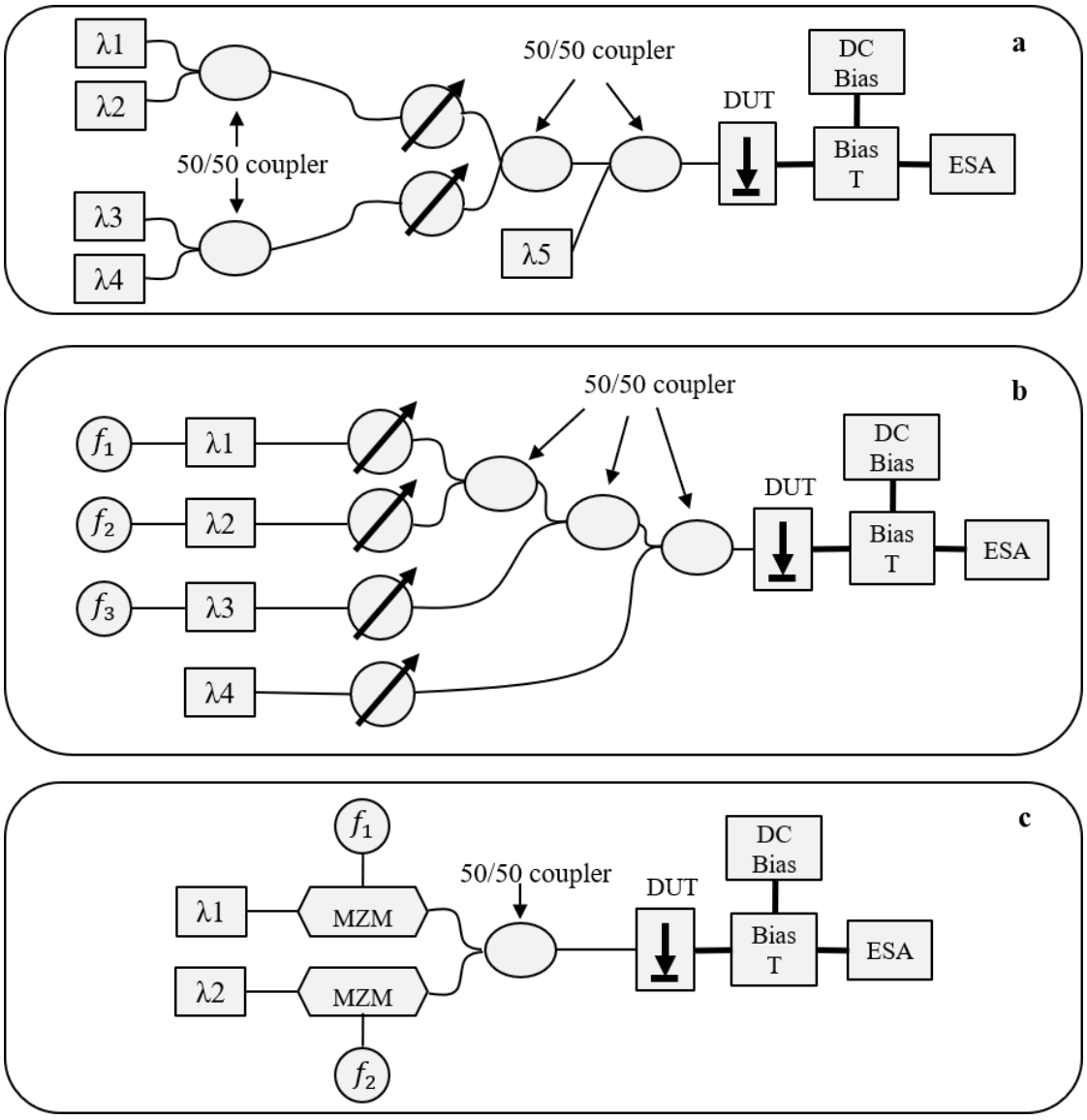

Figure 5.2: Three types of modulation scheme: a) heterodyne two-tone test system, b) direct modulated laser three-tone system, c) external modulated two-tone system.

5.2 Three-tone system theory and simulation

The optimized three-tone system using external modulation is illustrated in Figure 5.3. Three tunable lasers are set to different wavelengths so the optical intermodulation has no impact on the photodetector test. The optical carriers are then modulated by three MZMs with frequencies at f_1, f_2, and f_3, and the modulators are biased to quadrature to minimize its nonlinearity. Then three modulated optical signals are amplified by an EDFA that has automatic power control. As the output of the Erbium-doped fiber amplifier (EDFA) is constant when RF input is changed, a fourth laser to maintain constant photocurrent is not required. The output of the EDFA is maintained at constant power to minimize the EDFA nonlinearity. As an alternative, a passive optical attenuator is used to control the optical power injected into the photodetector. The photodetector nonlinearity can be measured at different photocurrents, frequencies, and bias voltages using this configuration. When the RF output on the photodetector is very strong, the electrical spectrum analyzer can introduce nonlinear distortion. In order to overcome this problem and increase the range of OIP3 the system can measure, an RF attenuator is added at the input of the electrical spectrum analyzer.

In the push-pull MZM configuration, the first order optical response of MZM can be written as:

$$\begin{cases} P_i = P_{LDi} L_i [1 + sin(\phi_{dci}) J_1(m_i)\, sin(\omega_i t)] \\ \phi_{dc} = \frac{\pi V_{dc}}{V_{\pi,dc}} \quad m_i = \frac{\pi V_{rfi}}{V_{\pi,rfi}} \quad \omega_i = 2\pi f_{rfi}\,, \end{cases} \tag{5.1}$$

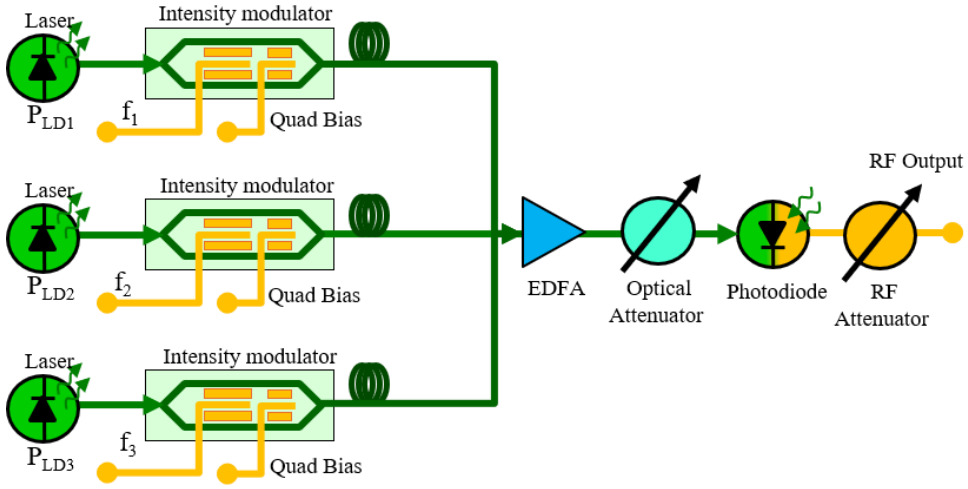

Figure 5.3: A three-tone photodetector nonlinearity test system based on external modulation and an EDFA with automatic gain control.

where P_{LDi} is the optical power of the i^{th} laser, $L_i$is the optical loss of channel i from laser to photodetector, m_i is the modulation index of the i^{th} MZM, and V_{rfi} is the driving voltage of the i^{th} input RF signal. The total optical power on the photodetector would be:

$$P_{tot} = (P_1 + P_2 + P_3)g_{EDFA}\ . \tag{5.2}$$

As the wavelength of the three lasers are set far away from each other, the photodetector does respond to the intermodulation between different optical carriers. Suppose the modulator is quadrature biased, the optical power to generate RF current on the photodetector is:

$$\begin{cases} P_{tot\_RF} = \sum_{i=1}^{3} \gamma_i \, sin(\omega_i t) \\ \gamma_i = P_{LDi} L_i J_1(m_i)\ . \end{cases} \tag{5.3}$$

The responsivity of the photodetector is usually given for the DC photocurrent; however, the responsivity should also be considered for the RF photocurrent. Using a

polynomial model where only the fundamental, second order, and third order response are considered, the RF photocurrent can be written as:

$$I_{PD} = c_1 P_{tot\_RF} + c_2 P_{tot\_RF}^2 + c_3 P_{tot\_RF}^3 \,, \tag{5.4}$$

Where the c_1, c_2, and c_3 are the responsivity corresponding to different order of optical mixing. The fundamental response determines the power of useful signals which can be written as:

$$I_{PD\_fundamental} = c_1(\gamma_1 \sin \omega_1 t + \gamma_2 \sin \omega_2 t + \gamma_3 \sin \omega_3 t) \,. \tag{5.5}$$

As the second order intermodulation is close to DC, it is not considered in most applications. The second order harmonics are far away from the fundamental signal and is considered in broadband applications. For the IMD3, it is worth expanding the third order intermodulation $c_3(\gamma_1 \sin \omega_1 t + \gamma_2 \sin \omega_2 t + \gamma_3 \sin \omega_3 t)^3$, so that the photocurrent of the IMD3 generated by two-tone mix and three-tone mix can be calculated as:

$$\begin{cases} IMD3(2f_i - f_k): & \frac{3c_3\gamma_i^2\gamma_k}{4} \\ IMD3(f_i + f_j - f_k): & \frac{3c_3\gamma_i\gamma_j\gamma_k}{2} \,. \end{cases} \tag{5.6}$$

If $\gamma_i = \gamma_j = \gamma_k$, the IMD3 power generated by $2f_i - f_k$ will be 6 dB lower than IMD3 power generated by $f_i + f_j - f_k$. The relationship between the fundamental and IMD3 frequencies are illustrated in Figure 5.4. f_1, f_2, and f_3 are selected in such a way that the offset in between is not equal to avoid an overlap between the IMD3 frequencies generated by two-tone mix or three-tone mix.

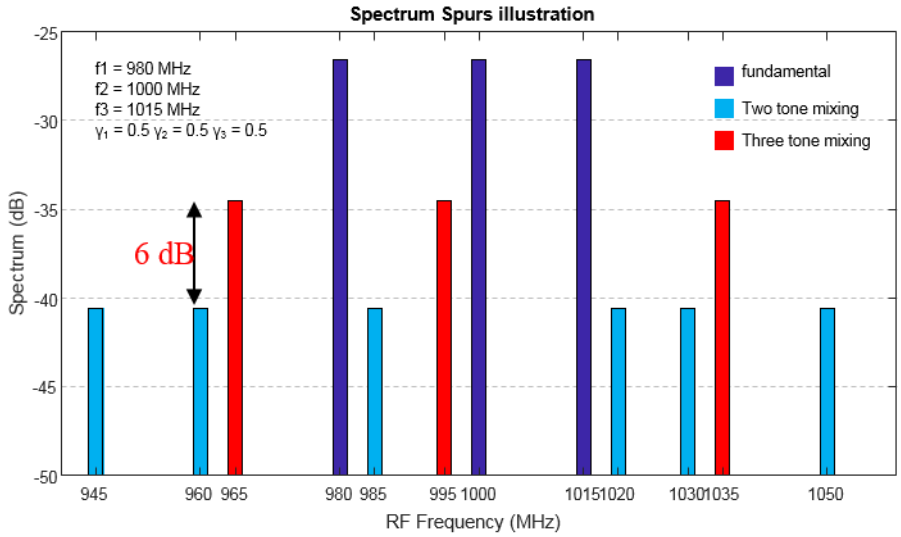

Figure 5.4: A RF spectrum illustration according to Equation 5.6 where the fundamental and third-order intermodulation frequencies are plotted.

As the transfer function of MZM is sinusoidal, various high order distortions can be monitored. Here we have only investigate the fundamental, second-order and third-order harmonics. If the photodetector is perfect linear, all distortions can be attributed to the MZM, which are listed in the first column of Table 5.1. Since f_1, f_2, and f_3 are the signals of interest, $2f_i$ and $3f_i$ are unwanted which can be filtered easily. If the photodetector is not perfectly linear, second and third order distortion occurs, which is shown in the second and third column of Table 5.1. There are three frequencies in the third column that are generated solely by the third order distortion of the photodetector, i.e., $f_1 + f_2 - f_3$, $f_1 + f_3 - f_2$, and $f_2 + f_3 - f_1$. Those frequencies are close to the fundamental frequencies and can serve as good indicators of IMD3 in photodetectors.

Table 5.1: The first, second, and third order harmonics and intermodulation in photodetector and Mach-Zehnder modulator.

		Photodiode		
		1st	2nd	3rd
Optical modulator	1st	f_{rf1} f_{rf2} f_{rf3}	$f_{rf1}-f_{rf2}$ $f_{rf1}+f_{rf2}$ $f_{rf1}-f_{rf3}$ $f_{rf1}+f_{rf3}$ $f_{rf2}-f_{rf3}$ $f_{rf2}+f_{rf3}$	$f_{rf1}+f_{rf2}-f_{rf3}$ $f_{rf1}+f_{rf3}-f_{rf2}$ $f_{rf2}+f_{rf3}-f_{rf1}$ $2f_{rf1}-f_{rf2}$ $2f_{rf1}-f_{rf3}$ $2f_{rf2}-f_{rf1}$ $2f_{rf2}-f_{rf3}$ $2f_{rf3}-f_{rf1}$ $2f_{rf3}-f_{rf1}$
	2nd	$2f_{rf1}$ $2f_{rf2}$ $2f_{rf3}$	$2f_{rf1}-2f_{rf2}$ $2f_{rf1}+2f_{rf2}$ $2f_{rf1}-2f_{rf3}$ $2f_{rf1}+2f_{rf3}$ $2f_{rf2}-2f_{rf3}$ $2f_{rf2}+2f_{rf3}$	$2\begin{pmatrix} f_{rf1}+f_{rf2}-f_{rf3} & f_{rf1}+f_{rf3}-f_{rf2} & f_{rf2}+f_{rf3}-f_{rf1} \\ 2f_{rf1}-f_{rf2} & 2f_{rf1}-f_{rf3} & 2f_{rf2}-f_{rf1} \\ 2f_{rf2}-f_{rf3} & 2f_{rf3}-f_{rf1} & 2f_{rf3}-f_{rf1} \end{pmatrix}$
	3rd	$3f_{rf1}$ $3f_{rf2}$ $3f_{rf3}$	$3f_{rf1}-3f_{rf2}$ $3f_{rf1}+3f_{rf2}$ $3f_{rf1}-3f_{rf3}$ $3f_{rf1}+3f_{rf3}$ $3f_{rf2}-3f_{rf3}$ $3f_{rf2}+3f_{rf3}$	$3\begin{pmatrix} f_{rf1}+f_{rf2}-f_{rf3} & f_{rf1}+f_{rf3}-f_{rf2} & f_{rf2}+f_{rf3}-f_{rf1} \\ 2f_{rf1}-f_{rf2} & 2f_{rf1}-f_{rf3} & 2f_{rf2}-f_{rf1} \\ 2f_{rf2}-f_{rf3} & 2f_{rf3}-f_{rf1} & 2f_{rf3}-f_{rf1} \end{pmatrix}$

A simulation based on this three-tone setup is completed using MATLAB where the RF inputs are sinusoidal waveforms, the Mach-Zehnder modulator transfer function follows Equation 2.1, and the response of the photodetector follows Equation 5.4. The RF spectrum of the calculated photocurrent can be acquired using a digital spectrum analyzer, which is based on Discrete Fourier Transform (DFT).

As shown in Figure 5.5, the RF spectrum that includes the fundamental and IMD3 frequencies in a three-tone test is illustrated. This simulation is performed around 1 GHz fundamental frequencies where the frequency offsets are 20 MHz and 30 MHz. With this asymmetric frequency offset, IMD3 attributed to two-tone mix and three-tone mix can be separated. From this simulation, it is confirmed that the three-tone IMD3 is 6 dB stronger than the two-tone IMD3. Extracting both the fundamental and IMD3 power from Figure 5.5 at different RF inputs (-30 – 10 dBm), this relationship can be plotted in Figure 5.6. As expected, fundamental and IMD3 response have slopes of 1 and 3, which will intercept at the OIP3 of a photodetector.

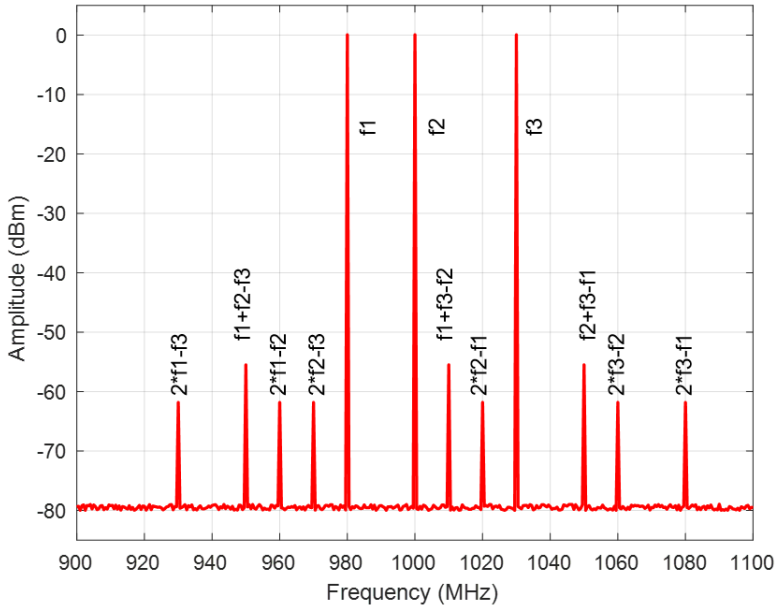

Figure 5.5: The RF spectrum acquired using the three-tone test model.

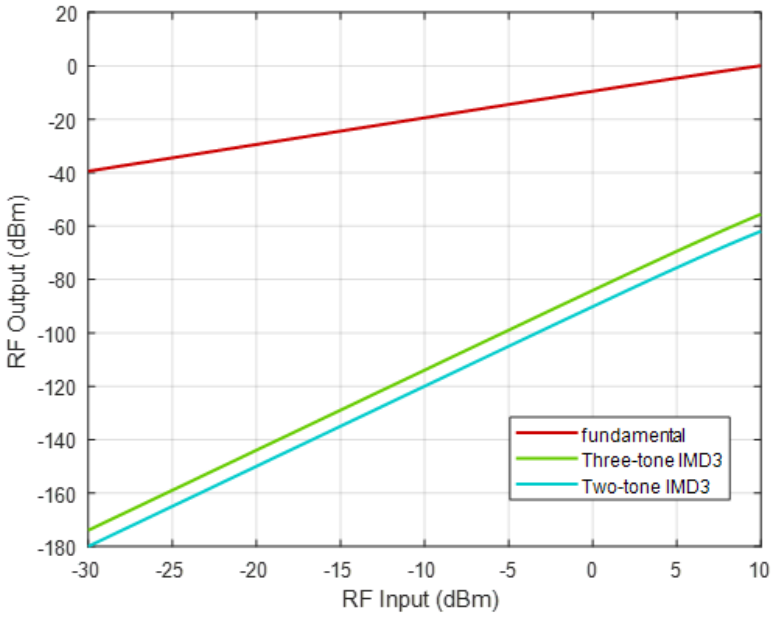

Figure 5.6: Simulated three-tone test result where the power of the fundamental and IMD3 frequencies are plotted.

5.3 System integration

As illustrated in Figure 5.7, a three-tone photodetector nonlinearity measurement system is integrated consisting of a modulation module, an RF source module, and an EDFA module. The modulation module completes the modulation process, the RF source module provides the system with high purity RF signals, and the EDFA module helps to maintain a constant photocurrent.

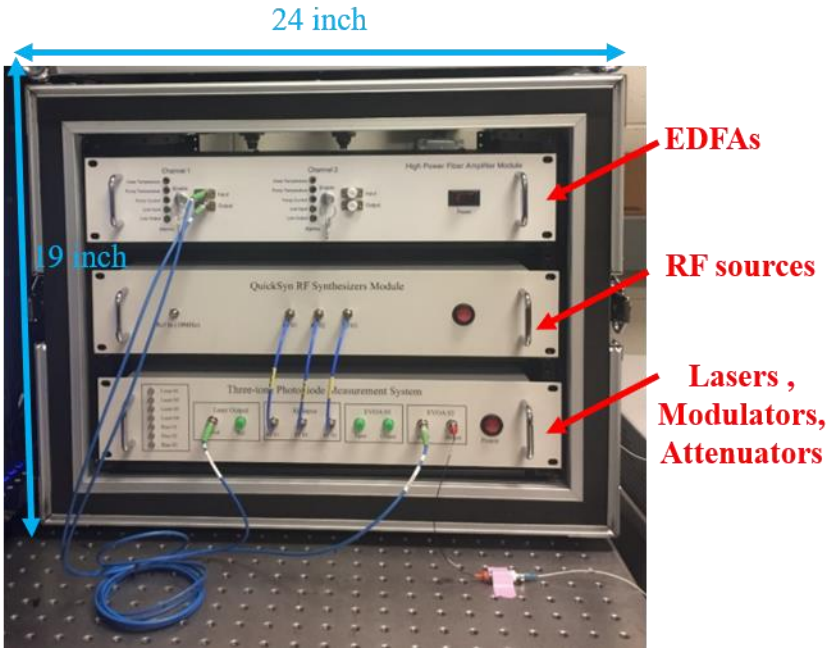

Figure 5.7: A three-tone test system is integrated on a rack which can measure OIP3 of photodetectors up to 20 GHz.

As shown in Figure 5.8, the modulation module consists of four lasers, three MZMs, and two variable optical attenuators. Three ID Photonics CoBrite DX1 lasers, with parameters listed in Table 5.2, are used to provide optical carriers to the three MZMs. The modulators are commercially available intensity modulators from Optilab

(IM-1550-40-PM-HER) and their parameters are listed in Table 5.3. The modulators are controlled by three individual bias controllers in order to maintain them at quadrature bias. The bias controller is based on pilot tone and a feedback loop, where internally integrated photodetectors in the MZMs are used. With the help of the MZMs, three RF signals are upconverted into three optical carriers and combined by two 50/50 optical couplers.

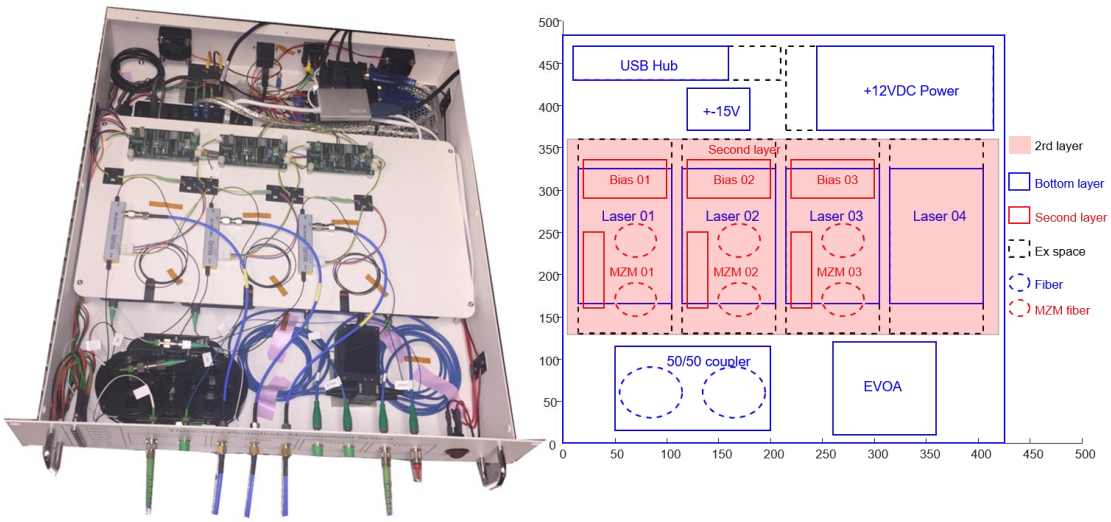

Figure 5.8: The arrangement of optical modulation module.

Table 5.2: Technical specification of the lasers

Optical Parameters	Laser (H01)	Unit
Wavelength Tunability	191.3-196.25	THz
Optical Output Power	6-15.5	dBm
RIN	< -145 (up to 40 GHz)	dB/Hz
Frequency accuracy (24 hours)	1.5	GHz

Table 5.3: Technical specification of the electro-optic modulators.

Optical Parameter	IM-1550-40-PM-HER	Unit
Wavelength	1525-1610	nm
3dB bandwidth	>30	GHz
Insertion loss	<4.5	dB
Extinction Ratio	>30	dB
Vpi (RF)	<4.5 @ 1 kHz	V
Input Optical Power	<100	mW
Input RF Power	<27	dBm

As shown in Figure 5.9, the RF source module consists of three RF synthesizers (National Instrument QuickSyn). They provide the MZMs with RF input at different frequencies. As each synthesizer drains 20W nominal power, heat sinks and fans are used to ensure that they do not overheat. The RF source module is isolated from the modulation module because lasers, modulators, and optical fibers are very sensitive to ambient temperatures. As the RF output range of the RF synthesizer is -20 dBm to +13 dBm, no additional RF amplifier is required because there is 33 dB dynamic range to drive the MZM.

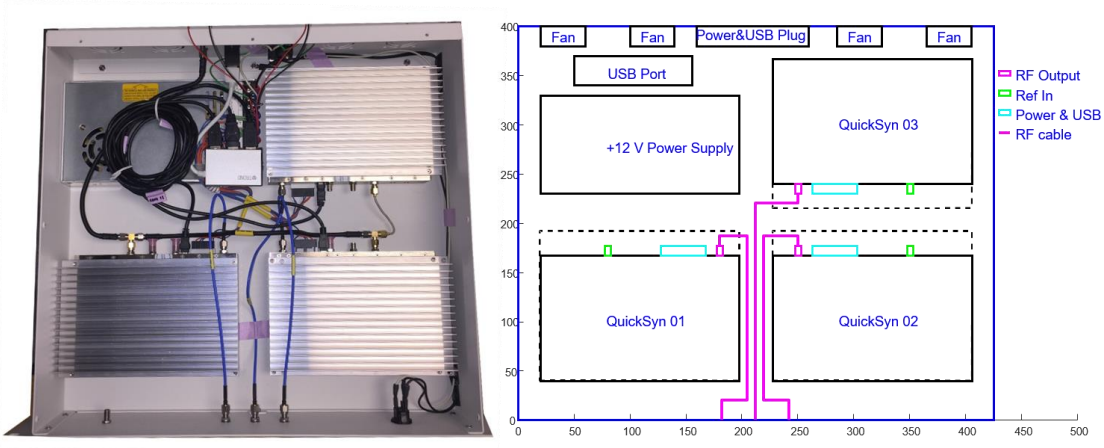

Figure 5.9: The RF source module with three QuickSyn RF synthesizers.

The EDFA module contains two optical amplifiers that can output 27-33 dBm optical power. As each EDFA consumes about 10W power, the heat sink and fans are also employed. To maintain a stable EDFA output power, the input optical power should always be higher than -10 dBm. Since ASE is the main concern of EDFA, the optical signal should be maximized in order to ensure the EDFA operates within its saturation region. Lastly, optical variable attenuators are used to control the optical power after EDFA, so photocurrent can be precisely controlled.

In summary, a three-tone test can be accomplished by using those three modules simultaneously. RF signals are generated and upconverted into an optical signal, then amplified to drive the photodetector. The wavelengths of the three lasers are set apart from each other in order to avoid any intermodulation response on the photodetector, where the frequency offset should at least double the frequency of interest. In this dissertation, the lasers are set 50 GHz apart to ensure that 20 GHz photodetector can be measured.

5.4 Experiment and analysis

A wide range of three-tone tests are done with the help of this three-tone system to evaluate the OIP3 of MUTC photodetectors under different photocurrents, frequencies, and bias voltages. The OIP3 is calculated based on measuring the fundamental and third order intermodulation frequencies. As illustrated in Figure 5.10, the fundamental signal has a slope of 1, and the third-order distortion has a slope of 3. The intercept point of two lines are the output intercept point of third order (OIP3), which can be calculated by:

$$OIP_3 = \frac{3P_f - P_t}{2}, \tag{5.7}$$

where P_f and P_t are the fundamental and third-order RF power measured on the photodetector.

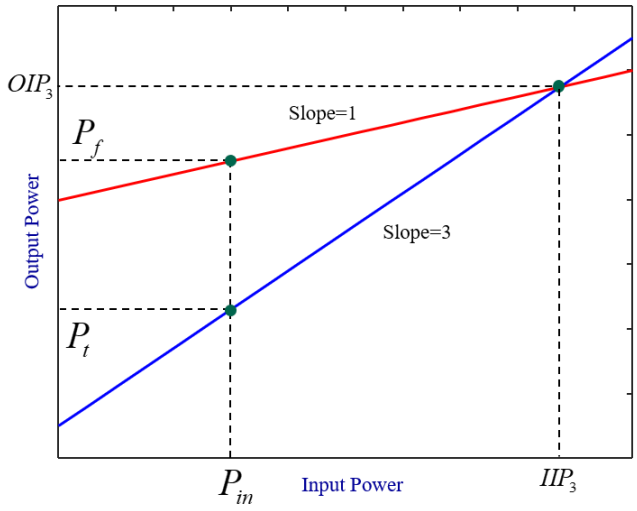

Figure 5.10: The OIP3 of photodetector can be calculated using curve fitting.

5.4.1 Accuracy validation

To investigate the accuracy of this three-tone test, we use two systems to test the same photodetectors and compare their results. Two MUTC photodetectors (MUTC-4 and MUTC-13) are tested at photocurrents range from 20 mA to 60 mA. As shown in Figure 5.11, an MUTC-4 photodetector is reverse biased at 5.5 V and the RF signals are at 10 GHz. This photodetector has a peak OIP3 of 36 dBm measured at 50 mA photocurrent while the OIP3 drops on both sides, i.e., 4 dB at 20 mA, and 2 dB at 60 mA. This phenomenon has been also reported in [114]–[116], where one or two OIP3 peaks are observed. In the second test, an MUTC-13 photodetector is test with various photocurrents, from 10 mA to 35 mA, at 10GHz with 4.5 V reverse bias voltage. As shown in Figure 5.12, the OIP3 is maximized at 32.5 dBm with 16 mA photocurrent.

Based on this result, the measured OIP3 of those MUTC photodetectors are above 30 dBm and more importantly, the measured results agree with one another with less than 1 dB difference.

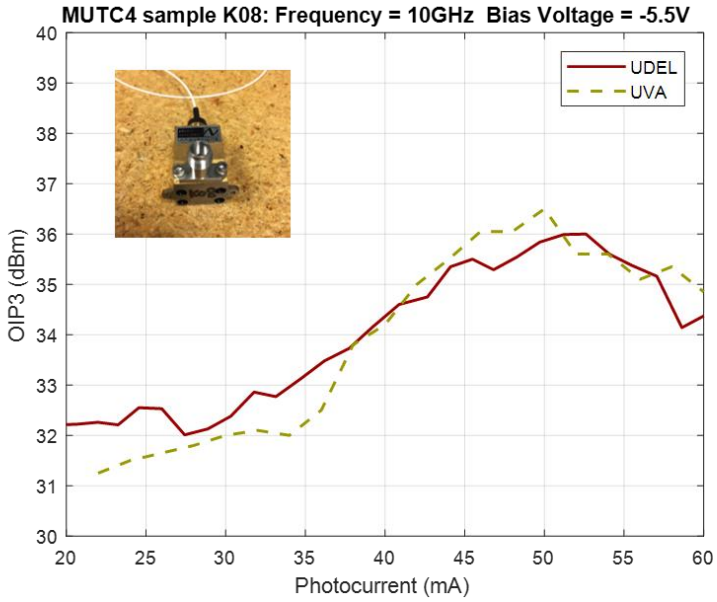

Figure 5.11 MUTC-4 photodetector and its OIP3 measured using two three-tone test systems at UDEL and UVA.

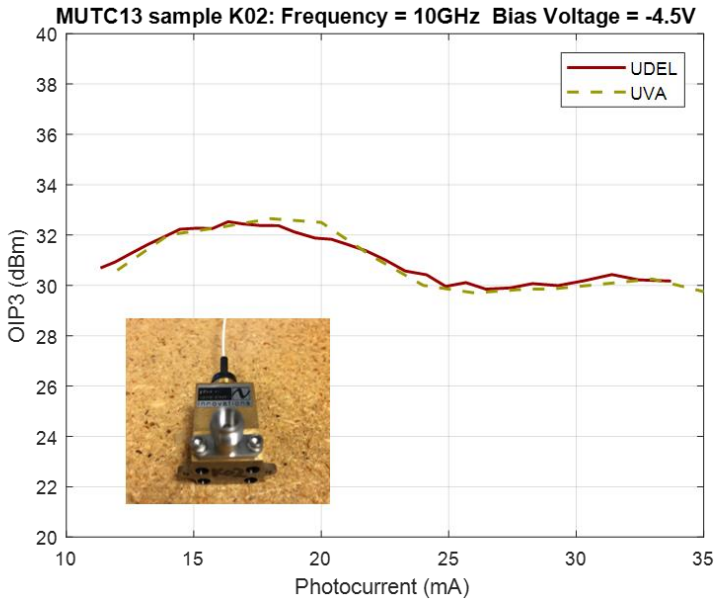

Figure 5.12 MUTC-13 photodetector and its OIP3 measured using two three-tone test systems at UDEL and UVA.

5.4.2 OIP3 dependence on the photocurrent

Photocurrent determines how much RF power can be generated on a photodetector. In most applications, a high photocurrent is required to generate more RF power. In this test, two MUTC photodetectors are tested using at 5 GHz and 10 GHz. The MUTC-4 photodetector has a flat OIP3 at different photocurrents, see Figure 5.13. Whereas the MUTC-13 photodetector has OIP3 peaks at 12 mA and 34 mA. OIP3 peaks in MUTC photodetectors can be designed to meet application requirements. As a result, this phenomenon is beneficial to design high-power photodetector targeted at certain photocurrent. The peak in OIP3 at different photocurrents may originate from temperature dependent photodetector responsivity.

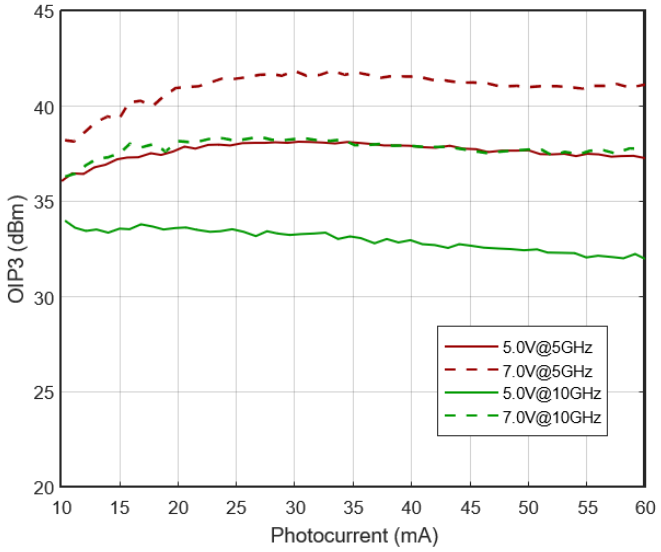

Figure 5.13: Measured OIP3 of MUTC-4 photodetector at different photocurrents.

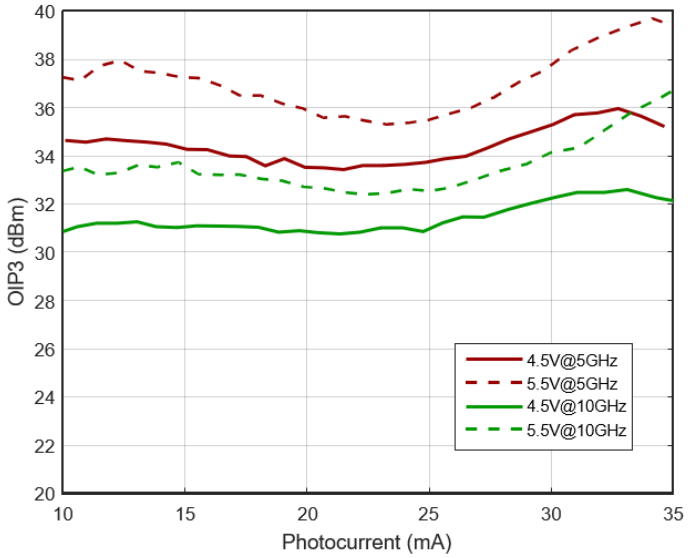

Figure 5.14: Measured OIP3 of MUTC-13 photodetector at different photocurrents.

5.4.3 OIP3 dependence on the frequency

The photodetector OIP3 is also a function of the frequency, so it is tested from 5 to 15 GHz. As shown in Figure 5.15, the measure OIP3 gets smaller at higher frequency with a variation within 5 dB. There are a few factors that account for this decrease. First, the photodetector's response rolls off with increased frequency, where the 3dB bandwidth of the MUTC-4 photodetector undertest is about 17 GHz. Second, the voltage-dependent capacitance in a photodetector adds more complexity to its frequency response. The frequency-dependent roll off, from the photodetector, is the main reason that decreases the OIP3. Unlike the smooth curve in Figure 5.13 and 5.14, where the photocurrent is controlled by an optical attenuator after an EDFA, the curves in Figure 5.15 are very noisy because the bias condition of an MZM is subjected to variation when the drive signal changes frequency.

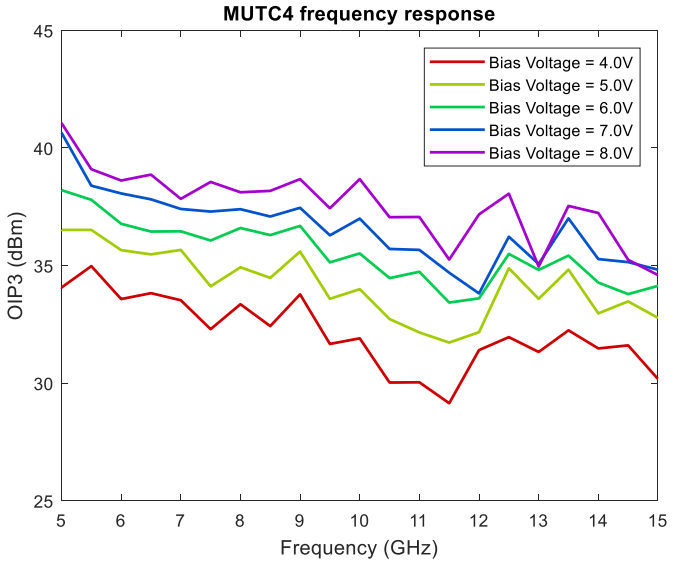

Figure 5.15: OIP3 of an MUTC-4 photodetector at different frequencies with 20 mA photocurrent.

5.4.4 OIP3 dependence on the bias voltage

An MUTC-4 photodetector is tested using the aforementioned three-tone system at different bias voltages. As this photodetector requires reversed bias, a Keithley 2401 source meter is used to drive the photodetector with voltage from 3 V to 8 V. As shown in Figure 5.16, OIP3 increases with the reverse bias voltage mainly because of the voltage-dependent responsivity [117]. The voltage dependent responsivity is caused by the Franz-Keldysh effect which describes the change of the absorption edge in semiconductor under high electric fields. In other words, the bias voltage changes the efficiency of optical-to-electrical conversion, so the OIP3 changes accordingly. In addition, OIP3 is linear proportional to the reverse-bias voltage at lower ranges and compresses at higher range. To take advantage from this phenomenon and avoid over-biasing the photodetector, the bias voltage should be set to 6-7 V.

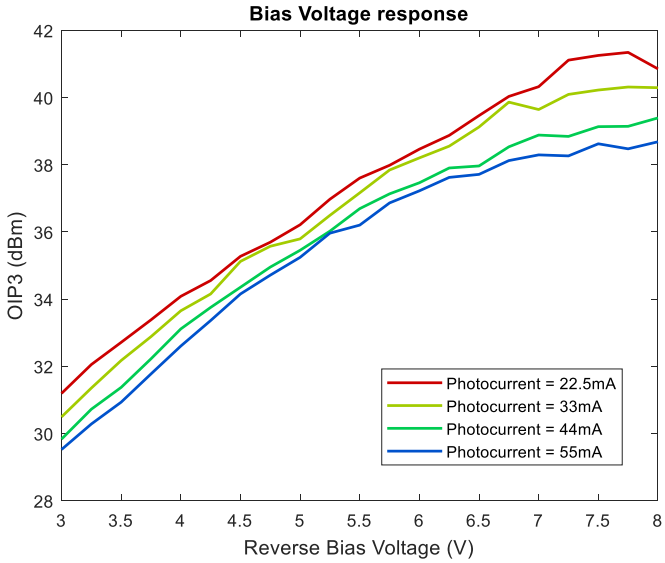

Figure 5.16: OIP3 of an MUTC-4 photodetector at different reverse bias voltages.

5.5 Summary

In this chapter, different schemes to implement the two-tone or three-tone methods are discussed and compared. According to the comparisons, a three-tone test with an external modulation scheme is the most accurate way to measure photodetector nonlinearities. The proposed three-tone test model is analyzed and simulated, where the relationship between IMD3 frequencies, generated by two-tone and three-tone mix, are compared. A three-tone photodetector nonlinearity measurement system is integrated which is capable of measuring OIP3 up to 20 GHz. The accuracy of this system is verified by testing the same photodetectors on two three-tone systems. Lastly, numerous experiments are done to investigate photodetector OIP3's dependence on photocurrents, frequencies, and bias voltages.

Chapter 6

CONCLUSION AND FUTURE WORK

6.1 Summary

This dissertation is targeted at investigating the nonlinearities of analog photonic links and seeking for linearization approaches, so a linearized analog photonic link for telecommunication can be realized. We first investigated the linearization of Mach-Zehnder modulator (MZM) digitally and optically, then a three-tone photodetector nonlinearity test system is interested and tested.

In the MZM digital predistortion approach, an arcsine transfer function is used to predistort the input data, so the sinusoidal transfer function of an MZM can be compensated. A dual-electrode Mach-Zehnder modulator (DE-MZM) is used to verify this linearization. In this configuration, one MZM is used for data modulation while the other MZM is used to provide a tunable optical carrier. Long-Term Evolution (LTE) signals with 5 MHz and 20 MHz bandwidths are tested in terms of adjacent channel leakage ratio (ACLR). Compared to an unlinearized link, 3-9 dB improvement of ACLR1 is monitored for 5 MHz and 20 MHz LTE signals using this digital predistortion. Then the digital predistortion is implemented in a photonic transceiver where tunable optical paired sources (TOPS) and single sideband (SSB) modulation are used. Again, the digital predistortion helps to improve the link's ACLR by 6-8 dB for various frequencies from 1.7 GHz to 17 GHz. However, the transfer function of MZM can be more complicated than ideal sinusoidal, so we investigated two optical

linearization approaches that two MZMs in parallel, i.e., two-wavelength linearization and two-polarization linearization.

In the two-wavelength linearization approach, two separate MZMs are arranged in parallel, where one MZM is feed by a high-power laser and a low-power RF signal while the other MZM is driven by a low-power laser and a high-power RF signal. The optical power ratio, RF power ratio, opposite quadrature bias, and 180-degree phase difference between two MZMs are calibrated to suppress the third-order intermodulation distortion (IMD3). LTE signals of various bandwidths are used to validate this linearization approach experimentally. It is demonstrated that with this approach the first adjacent channel leakage ratio (ACLR1) can be improved by 19.2 dB for a 10 MHz LTE signal, and 18.1 dB for a 20 MHz LTE signal at the cost of approximately 2 dB power penalty.

In the two-polarization linearization approach, a similar configuration using two parallel MZMs is used. However, there are two differences. First, only one laser is required so the cost is reduced. Second, the optically incoherent combination is based on polarization orthogonality using a polarization beam combiner (PBC). This approach is experimentally verified by a two-tone test where the IMD3 is suppressed by 39.2 dB at the cost of 2.3 dB power penalty. Later, a set of two-tone tests at 1 GHz are performed at various photocurrents to characterize the link's performance in terms of gain, noise figure, output intercept point (OIP), and SFDR. When the dual-polarization linearization technique is used, the SFDR can be increased by ~17 dB at the cost of 1.1~1.7 dB gain reduction and 1.0~1.7 dB noise figure increase. Also, LTE signals with bandwidths are delivered by this linearized link with ACLR1 improvement of 11.8~19.6 dB.

Lastly, different schemes to measure photodetector nonlinearity are summarized and compared. A three-tone setup using external modulation is analyzed, simulated, integrated and tested. Modified uni-traveling carrier (MUTC) photodetectors are tested to investigate their OIP3 dependence on photocurrents, bias voltages, and frequencies.

6.2 Future Work

1. The digital predistortion technique can be combined with optical linearization approach to further linearize analog photonic links.

2. Photodetector nonlinear model can be studied based on the nonlinear performance measured using this three-tone test setup.

3. Digital predistortion for photodetector nonlinearity can be investigated which can be verified using an optically linearized analog photonic link.

4. QAM and LTE signals at higher data rates can be tested using the same MZM linearization techniques, where the link's performance can be characterized in terms of eye diagram, EVM, and constellation.

5. The linearized analog links can be tested using long optical fibers to investigate their performance in long-haul applications.

REFERENCES

[1] D. Novak *et al.*, "Radio-Over-Fiber Technologies for Emerging Wireless Systems," *IEEE J. Quantum Electron.*, vol. 52, no. 1, pp. 1–11, Jan. 2016.

[2] H. Haas, L. Yin, Y. Wang, and C. Chen, "What is LiFi?," *J. Light. Technol.*, vol. 34, no. 6, pp. 1533–1544, Mar. 2016.

[3] J. Capmany, J. Mora, I. Gasulla, J. Sancho, J. Lloret, and S. Sales, "Microwave Photonic Signal Processing," *J. Light. Technol.*, vol. 31, no. 4, pp. 571–586, Feb. 2013.

[4] L. Tsybeskov, D. J. Lockwood, and M. Ichikawa, "Silicon Photonics: CMOS Going Optical [Scanning the Issue]," *Proc. IEEE*, vol. 97, no. 7, pp. 1161–1165, Jul. 2009.

[5] W. Ng, A. A. Walston, G. L. Tangonan, J. J. Lee, I. L. Newberg, and N. Bernstein, "The first demonstration of an optically steered microwave phased array antenna using true-time-delay," *J. Light. Technol.*, vol. 9, no. 9, pp. 1124–1131, Sep. 1991.

[6] R. H. Blumenthal, "Design of a Microwave-Frequency Light Modulator," *Proc. IRE*, vol. 50, no. 4, pp. 452–456, Apr. 1962.

[7] X. Li, Z. Dong, J. Yu, N. Chi, Y. Shao, and G. K. Chang, "Fiber-wireless transmission system of 108 Gb/s data over 80 km fiber and 2×2 multiple-input multiple-output wireless links at 100 GHz W-band frequency," *Opt. Lett.*, vol. 37, no. 24, pp. 5106–5108, Dec. 2012.

[8] J. Zhang, J. Yu, N. Chi, Z. Dong, X. Li, and G. Chang, "Multichannel 120-Gb/s Data Transmission Over 2 ×2 MIMO Fiber-Wireless Link at W-Band," *IEEE Photonics Technol. Lett.*, vol. 25, no. 8, pp. 780–783, Apr. 2013.

[9] R. Puerta, J. Yu, X. Li, Y. Xu, J. J. V. Olmos, and I. T. Monroy, "Single-Carrier Dual-Polarization 328-Gb/s Wireless Transmission in a D-Band Millimeter Wave 2 × 2 MU-MIMO Radio-Over-Fiber System," *J. Light. Technol.*, vol. 36, no. 2, pp. 587–593, Jan. 2018.

[10] N. H. Zhu *et al.*, "Directly Modulated Semiconductor Lasers," *IEEE J. Sel. Top. Quantum Electron.*, vol. 24, no. 1, pp. 1–19, Jan. 2018.

[11] Y. Matsui *et al.*, "55-GHz Bandwidth Short-Cavity Distributed Reflector Laser and its Application to 112-Gb/s PAM-4," in *Optical Fiber Communication Conference Postdeadline Papers (2016), paper Th5B.4*, 2016, p. Th5B.4.

[12] S. Kobayashi, Y. Yamamoto, M. Ito, and T. Kimura, "Direct frequency modulation in AlGaAs semiconductor lasers," *IEEE J. Quantum Electron.*, vol. 18, no. 4, pp. 582–595, Apr. 1982.

[13] R. Tucker, "High-speed modulation of semiconductor lasers," *J. Light. Technol.*, vol. 3, no. 6, pp. 1180–1192, Dec. 1985.

[14] T. L. Koch and J. E. Bowers, “Nature of wavelength chirping in directly modulated semiconductor lasers,” *Electron. Lett.*, vol. 20, no. 25, pp. 1038–1040, Dec. 1984.
[15] J. E. Simsarian, M. C. Larson, H. E. Garrett, Hong Xu, and T. A. Strand, “Less than 5-ns wavelength switching with an SG-DBR laser,” *IEEE Photonics Technol. Lett.*, vol. 18, no. 4, pp. 565–567, Feb. 2006.
[16] N. Fujiwara, H. Ishii, H. Okamoto, Y. Kawaguchi, Y. Kondo, and H. Oohashi, “Suppression of Thermal Wavelength Drift in Super-Structure Grating Distributed Bragg Reflector (SSG-DBR) Laser with Thermal Drift Compensator,” *IEEE J. Sel. Top. Quantum Electron.*, vol. 13, no. 5, pp. 1164–1169, Sep. 2007.
[17] H. Okamoto *et al.*, “A wavelength-tunable duplex integrated light source for fast wavelength switching,” *J. Light. Technol.*, vol. 14, no. 6, pp. 1033–1041, Jun. 1996.
[18] M. Gay *et al.*, “Frequency Drift Reduction in a Four-Laser Array for TWDM PON Applications,” *IEEE Photonics Technol. Lett.*, vol. 30, no. 14, pp. 1345–1348, Jul. 2018.
[19] Y. Ueno, K. Mochizuki, K. Hasegawa, and M. Nogami, “Fast wavelength switching with DFB lasers utilizing thermal compensation,” in *2015 Opto-Electronics and Communications Conference (OECC)*, 2015, pp. 1–3.
[20] S. Yoo, J. K. Lee, and K. Kim, “Suppression of thermal wavelength drift in widely tunable DS-DBR laser for fast channel-to-channel switching,” *Opt. Express*, vol. 25, no. 24, p. 30406, Nov. 2017.
[21] Y. Tian *et al.*, “Drive design and performance test of a tunable DFB laser,” in *2017 Chinese Automation Congress (CAC)*, Jinan, 2017, pp. 4024–4027.
[22] C. H. Cox, G. E. Betts, and L. M. Johnson, “An analytic and experimental comparison of direct and external modulation in analog fiber-optic links,” *IEEE Trans. Microw. Theory Tech.*, vol. 38, no. 5, pp. 501–509, May 1990.
[23] A. J. Mercante, S. Shi, P. Yao, L. Xie, R. M. Weikle, and D. W. Prather, “Thin film lithium niobate electro-optic modulator with terahertz operating bandwidth,” *Opt. Express*, vol. 26, no. 11, pp. 14810–14816, May 2018.
[24] E. I. Ackerman *et al.*, “Signal-to-Noise Performance of Two Analog Photonic Links Using Different Noise Reduction Techniques,” in *2007 IEEE/MTT-S International Microwave Symposium*, Honolulu, HI, USA, 2007, pp. 51–54.
[25] Y. Fu, X. Zhang, B. Hraimel, T. Liu, and D. Shen, “Mach-Zehnder: A Review of Bias Control Techniques for Mach-Zehnder Modulators in Photonic Analog Links,” *IEEE Microw. Mag.*, vol. 14, no. 7, pp. 102–107, Nov. 2013.
[26] T. Gorman and S. Haxha, “Full-Wave Comparison of Z-cut and X-cut Lithium Niobate (LiNbO3) Electrooptic Modulators Using Finite Element Method,” p. 6, 2007.
[27] H. Nagata and K. Kiuchi, “Temperature dependence of dc drift of Ti:$LiNbO_3$ optical modulators with sputter deposited SiO_2 buffer layer,” *J. Appl. Phys.*, vol. 73, no. 9, pp. 4162–4164, May 1993.

[28] H. Nagata, Y. Li, W. R. Bosenberg, and G. L. Reiff, “DC Drift of X-Cut LiNbO<tex>$_3$</tex>Modulators,” *IEEE Photonics Technol. Lett.*, vol. 16, no. 10, pp. 2233–2235, Oct. 2004.
[29] N. Mitsugi, K. Kiuchi, and H. Nagata, “Activation Energy for Dc-drift in X-cut LiNbO_3 Optical Intensity Modulators,” *Appl. Opt.*, vol. 37, no. 34, p. 8147, Dec. 1998.
[30] M. B. Shemirani and J. M. Kahn, “Higher-Order Modal Dispersion in Graded-Index Multimode Fiber,” *J. Light. Technol.*, vol. 27, no. 23, pp. 5461–5468, Dec. 2009.
[31] A. Gholami, D. Molin, and P. Sillard, “Compensation of Chromatic Dispersion by Modal Dispersion in MMF- and VCSEL-Based Gigabit Ethernet Transmissions,” *IEEE Photonics Technol. Lett.*, vol. 21, no. 10, pp. 645–647, May 2009.
[32] G. Yabre, “Comprehensive theory of dispersion in graded-index optical fibers,” *J. Light. Technol.*, vol. 18, no. 2, pp. 166–177, Feb. 2000.
[33] G. H. Smith, D. Novak, and Z. Ahmed, “Overcoming chromatic-dispersion effects in fiber-wireless systems incorporating external modulators,” *IEEE Trans. Microw. Theory Tech.*, vol. 45, no. 8, pp. 1410–1415, Aug. 1997.
[34] V. J. Urick and F. Bucholtz, “Compensation of arbitrary chromatic dispersion in analog links using a modulation-diversity receiver,” *IEEE Photonics Technol. Lett.*, vol. 17, no. 4, pp. 893–895, Apr. 2005.
[35] Nan-Kuang Chen and Sien Chi, “Spectral characteristics of side-polished endlessly single-mode photonic crystal fiber: waveguide dispersion,” in *2006 Optical Fiber Communication Conference and the National Fiber Optic Engineers Conference*, 2006, pp. 3 pp.-.
[36] S. Rashleigh, “Origins and control of polarization effects in single-mode fibers,” *J. Light. Technol.*, vol. 1, no. 2, pp. 312–331, Jun. 1983.
[37] R. B. Dyott, J. R. Cozens, and D. G. Morris, “Preservation of polarisation in optical-fibre waveguides with elliptical cores,” *Electron. Lett.*, vol. 15, no. 13, pp. 380–382, Jun. 1979.
[38] K. Okamoto, T. Hosaka, and Y. Sasaki, “Linearly single polarization fibers with zero polarization mode dispersion,” *IEEE J. Quantum Electron.*, vol. 18, no. 4, pp. 496–503, Apr. 1982.
[39] R. D. Birch, D. N. Payne, and M. P. Varnham, “Fabrication of polarisation-maintaining fibres using gas-phase etching,” *Electron. Lett.*, vol. 18, no. 24, pp. 1036–1038, Nov. 1982.
[40] P. Urquhart, O. G. Lopez, G. Boyen, and A. Bruckmann, “Optical Amplifiers for Telecommunications,” in *2007 IEEE International Symposium on Intelligent Signal Processing*, 2007, pp. 1–6.
[41] C. R. Giles and E. Desurvire, “Modeling erbium-doped fiber amplifiers,” *J. Light. Technol.*, vol. 9, no. 2, pp. 271–283, Feb. 1991.

[42] K. Kikushima and H. Yoshinaga, “Distortion due to gain tilt of erbium-doped fiber amplifiers,” *IEEE Photonics Technol. Lett.*, vol. 3, no. 10, pp. 945–947, Oct. 1991.
[43] C. Y. Kuo and E. E. Bergmann, “Second-order distortion and electronic compensation in analog links containing fiber amplifiers,” *J. Light. Technol.*, vol. 10, no. 11, pp. 1751–1759, Nov. 1992.
[44] C. Y. Kuo, “Fundamental nonlinear distortions in analog links with fiber amplifiers,” *J. Light. Technol.*, vol. 11, no. 1, pp. 7–15, Jan. 1993.
[45] Chia-Chi Wang and G. J. Cowle, “Optical gain control of erbium-doped fiber amplifiers with a saturable absorber,” *IEEE Photonics Technol. Lett.*, vol. 12, no. 5, pp. 483–485, May 2000.
[46] Uh-Chan Ryu, K. Oh, W. Shin, and U. C. Paek, “Inherent enhancement of gain flatness and achievement of broad gain bandwidth in erbium-doped silica fiber amplifiers,” *IEEE J. Quantum Electron.*, vol. 38, no. 2, pp. 149–161, Feb. 2002.
[47] H. Ono, M. Yamada, and M. Shimizu, “S-band erbium-doped fiber amplifiers with a multistage configuration esign, characterization, and gain tilt compensation,” *J. Light. Technol.*, vol. 21, no. 10, pp. 2240–2246, Oct. 2003.
[48] T. Hatano, D. Yoon, and K. Mizuno, “Fast gain tilt compensator employing LiNbO/sub 3/ polarization transformer,” in *2005 31st European Conference on Optical Communication, ECOC 2005*, 2005, vol. 4, pp. 823–824 vol.4.
[49] Vincent J. Urick Jr., Jason D. Mckinney, Keith J. Williams, “Distortion in Fiber Optic Links,” in *FUNDAMENTALS OF MICROWAVE PHOTONICS*, John Wiley & Sons, Ltd, 2015, pp. 124–165.
[50] T. Ozeki and E. H. Hara, “Measurement of nonlinear distortion in photodiodes,” *Electron. Lett.*, vol. 12, no. 3, pp. 80–81, Feb. 1976.
[51] R. D. Esman and K. J. Williams, “Measurement of harmonic distortion in microwave photodetectors,” *IEEE Photonics Technol. Lett.*, vol. 2, no. 7, pp. 502–504, Jul. 1990.
[52] H. Jiang and P. K. L. Yu, “Equivalent circuit analysis of harmonic distortions in photodiode,” *IEEE Photonics Technol. Lett.*, vol. 10, no. 11, pp. 1608–1610, Nov. 1998.
[53] K. J. Williams and R. D. Esman, “Photodiode DC and microwave nonlinearity at high currents due to carrier recombination nonlinearities,” *IEEE Photonics Technol. Lett.*, vol. 10, no. 7, pp. 1015–1017, Jul. 1998.
[54] A. S. Hastings, D. A. Tulchinsky, and K. J. Williams, “Photodetector Nonlinearities Due to Voltage-Dependent Responsivity,” *IEEE Photonics Technol. Lett.*, vol. 21, no. 21, pp. 1642–1644, Nov. 2009.
[55] M. Chtioui *et al.*, “High-Power High-Linearity Uni-Traveling-Carrier Photodiodes for Analog Photonic Links,” *IEEE Photonics Technol. Lett.*, vol. 20, no. 3, pp. 202–204, Feb. 2008.
[56] A. Beling, H. Pan, H. Chen, and J. C. Campbell, “Measurement and Modeling of a High-Linearity Modified Uni-Traveling Carrier Photodiode,” *IEEE Photonics Technol. Lett.*, vol. 20, no. 14, pp. 1219–1221, Jul. 2008.

[57] A. Beling, H. Pan, H. Chen, and J. C. Campbell, “Measurement and modelling of high-linearity partially depleted absorber photodiode,” *Electron. Lett.*, vol. 44, no. 24, pp. 1419–1420, Nov. 2008.
[58] A. S. Hastings *et al.*, “Suppression of Even-Order Photodiode Nonlinearities in Multioctave Photonic Links,” *J. Light. Technol.*, vol. 26, no. 15, pp. 2557–2562, Aug. 2008.
[59] M. N. Hutchinson, J. M. Singley, V. J. Urick, S. R. Harmon, J. D. McKinney, and N. J. Frigo, “Mitigation of Photodiode Induced Even-Order Distortion in Photonic Links With Predistortion Modulation,” *J. Light. Technol.*, vol. 32, no. 20, pp. 3885–3892, Oct. 2014.
[60] Y. Ye *et al.*, “Simultaneous Suppression of Even-Order and Third-Order Distortions in Directly Modulated Analog Photonic Links,” *IEEE Photonics J.*, vol. 9, no. 3, pp. 1–12, Jun. 2017.
[61] J. Davila-Rodriguez *et al.*, “Temperature dependence of nonlinearity in high-speed, high-power photodetectors,” in *2017 IEEE Photonics Conference (IPC)*, 2017, pp. 99–100.
[62] 3GPP, “LTE; Evolved Universal Terrestrial Radio Access (E-UTRA); Base Station (BS) conformance testing,” *3GPP TS 36141 Version 1560 Release 15*, pp. 202–208, May 2019.
[63] A. Egger, M. Horn, and T. Vien, “Broadband Linearization of Microwave Power Amplifiers,” in *1980 10th European Microwave Conference*, 1980, pp. 490–494.
[64] S. P. Stapleton and F. C. Costescu, “An adaptive predistorter for a power amplifier based on adjacent channel emissions (mobile communications),” *IEEE Trans. Veh. Technol.*, vol. 41, no. 1, pp. 49–56, Feb. 1992.
[65] jae-Hee Han, Tasik Chung, and Sangwook Nam, “Adaptive predistorter for power amplifier based on real-time estimation of envelope transfer characteristics,” *Electron. Lett.*, vol. 35, no. 25, pp. 2167–2168, Dec. 1999.
[66] J. Kim and K. Konstantinou, “Digital predistortion of wideband signals based on power amplifier model with memory,” *Electron. Lett.*, vol. 37, no. 23, pp. 1417–1418, Nov. 2001.
[67] D. R. Morgan, Z. Ma, J. Kim, M. G. Zierdt, and J. Pastalan, “A Generalized Memory Polynomial Model for Digital Predistortion of RF Power Amplifiers,” *IEEE Trans. Signal Process.*, vol. 54, no. 10, pp. 3852–3860, Oct. 2006.
[68] Y. J. Liu, W. Chen, J. Zhou, B. H. Zhou, and F. M. Ghannouchi, “Digital Predistortion for Concurrent Dual-Band Transmitters Using 2-D Modified Memory Polynomials,” *IEEE Trans. Microw. Theory Tech.*, vol. 61, no. 1, pp. 281–290, Jan. 2013.
[69] D. Zhou and V. E. DeBrunner, “Novel Adaptive Nonlinear Predistorters Based on the Direct Learning Algorithm,” *IEEE Trans. Signal Process.*, vol. 55, no. 1, pp. 120–133, Jan. 2007.

[70] M. Bertelsmeier and W. Zschunke, “Linearization of Broadband Optical Transmission Systems by Adaptive Predistortion,” *Frequenz*, vol. 38, no. 9, pp. 206–212, 1984.
[71] G. C. Wilson *et al.*, “Predistortion of electroabsorption modulators for analog CATV systems at 1.55 /spl mu/m,” *J. Light. Technol.*, vol. 15, no. 9, pp. 1654–1662, Sep. 1997.
[72] V. Magoon and B. Jalali, “Electronic linearization and bias control for externally modulated fiber optic link,” in *International Topical Meeting on Microwave Photonics MWP 2000 (Cat. No.00EX430)*, 2000, pp. 145–147.
[73] A. Katz, W. Jemison, M. Kubak, and J. Dragone, “Improved radio over fiber performance using predistortion linearization,” in *IEEE MTT-S International Microwave Symposium Digest, 2003*, 2003, vol. 2, pp. 1403–1406 vol.2.
[74] L. Roselli *et al.*, “Analog laser predistortion for multiservice radio-over-fiber systems,” *J. Light. Technol.*, vol. 21, no. 5, pp. 1211–1223, May 2003.
[75] V. J. Urick, M. S. Rogge, P. F. Knapp, L. Swingen, and F. Bucholtz, “Wide-band predistortion linearization for externally modulated long-haul analog fiber-optic links,” *IEEE Trans. Microw. Theory Tech.*, vol. 54, no. 4, pp. 1458–1463, Jun. 2006.
[76] Y. Shen, B. Hraimel, X. Zhang, G. E. R. Cowan, K. Wu, and T. Liu, “A Novel Analog Broadband RF Predistortion Circuit to Linearize Electro-Absorption Modulators in Multiband OFDM Radio-Over-Fiber Systems,” *IEEE Trans. Microw. Theory Tech.*, vol. 58, no. 11, pp. 3327–3335, Nov. 2010.
[77] Y. Bao, Z. Li, J. Li, X. Feng, B. Guan, and G. Li, “Nonlinearity mitigation for high-speed optical OFDM transmitters using digital pre-distortion,” *Opt. Express*, vol. 21, no. 6, pp. 7354–7361, Mar. 2013.
[78] R. Sadhwani and B. Jalali, “Adaptive CMOS predistortion linearizer for fiber-optic links,” *J. Light. Technol.*, vol. 21, no. 12, pp. 3180–3193, Dec. 2003.
[79] “LTE;Evolved Universal Terrestrial Radio Access (E-UTRA);User Equipment (UE) radio transmission and reception,” *3GPP TS 36101 Version 1350 Release 13*, pp. 162–166, Dec. 2016.
[80] H. Pan, X. Wang, A. Beling, H. Chen, and J. C. Campbell, “Characterization and Optimization of InGaAs/InP Photodiodes with High Saturation Current,” in *2007 International Conference on Numerical Simulation of Optoelectronic Devices*, 2007, pp. 79–80.
[81] Y. Fu, H. Pan, Z. Li, A. Beling, and J. C. Campbell, “Characterizing and Modeling Nonlinear Intermodulation Distortions in Modified Uni-Traveling Carrier Photodiodes,” *IEEE J. Quantum Electron.*, vol. 47, no. 10, pp. 1312–1319, Oct. 2011.
[82] G. J. Schneider, J. A. Murakowski, C. A. Schuetz, S. Shi, and D. W. Prather, “Radiofrequency signal-generation system with over seven octaves of continuous tuning,” *Nat. Photonics*, vol. 7, no. 2, pp. 118–122, Feb. 2013.

[83] G. H. Smith, D. Novak, and Z. Ahmed, “Technique for optical SSB generation to overcome dispersion penalties in fibre-radio systems,” *Electron. Lett.*, vol. 33, no. 1, pp. 74–75, Jan. 1997.
[84] S. K. Korotky and R. M. de Ridder, “Dual parallel modulation schemes for low-distortion analog optical transmission,” *IEEE J. Sel. Areas Commun.*, vol. 8, no. 7, pp. 1377–1381, Sep. 1990.
[85] G. E. Betts, “Linearized modulator for suboctave-bandpass optical analog links,” *IEEE Trans. Microw. Theory Tech.*, vol. 42, no. 12, pp. 2642–2649, Dec. 1994.
[86] M. L. Farwell, Z. Q. Lin, E. Wooten, and W. S. C. Chang, “An electrooptic intensity modulator with improved linearity,” *IEEE Photonics Technol. Lett.*, vol. 3, no. 9, pp. 792–795, Sep. 1991.
[87] T. P. McKenna, J. H. Kalkavage, T. R. Clark, R. B. Waterhouse, and D. Novak, “Photonic downconverting link with digital linearization,” in *2015 IEEE MTT-S International Microwave Symposium*, 2015, pp. 1–4.
[88] Y. Pan *et al.*, “Adaptive linearized microwave downconversion utilizing a single dual-electrode Mach–Zehnder modulator,” *Opt. Lett.*, vol. 40, no. 11, pp. 2649–2652, Jun. 2015.
[89] F. Wang *et al.*, “Photonic Generation of High Fidelity RF Sources for Mobile Communications,” *J. Light. Technol.*, vol. 35, no. 18, pp. 3901–3908, Sep. 2017.
[90] G. Zhu, W. Liu, and H. R. Fetterman, “A Broadband Linearized Coherent Analog Fiber-Optic Link Employing Dual Parallel Mach #x2013;Zehnder Modulators,” *IEEE Photonics Technol. Lett.*, vol. 21, no. 21, pp. 1627–1629, Nov. 2009.
[91] W. Jiang *et al.*, “A Linearization Analog Photonic Link With High Third-Order Intermodulation Distortion Suppression Based on Dual-Parallel Mach–Zehnder Modulator,” *IEEE Photonics J.*, vol. 7, no. 3, pp. 1–8, Jun. 2015.
[92] J. L. Brooks, G. S. Maurer, and R. A. Becker, “Implementation and evaluation of a dual parallel linearization system for AM-SCM video transmission,” *J. Light. Technol.*, vol. 11, no. 1, pp. 34–41, Jan. 1993.
[93] E. I. Ackerman, “Broad-band linearization of a Mach-Zehnder electrooptic modulator,” *IEEE Trans. Microw. Theory Tech.*, vol. 47, no. 12, pp. 2271–2279, Dec. 1999.
[94] E. I. Ackerman, G. E. Betts, and C. H. Cox, “Inherently broadband linearized modulator for high-SFDR, low-NF microwave photonic links,” in *2016 IEEE International Topical Meeting on Microwave Photonics (MWP)*, 2016, pp. 265–268.
[95] B. M. Haas, V. J. Urick, J. D. McKinney, and T. E. Murphy, “Dual-Wavelength Linearization of Optically Phase-Modulated Analog Microwave Signals,” *J. Light. Technol.*, vol. 26, no. 15, pp. 2748–2753, Aug. 2008.
[96] T. Jiang, R. Wu, S. Yu, D. Wang, and W. Gu, “A Novel High-Linearity Microwave Photonic Link Based on the Strategy of Adding a Compensation Path

Using a Bidirectional Phase Modulator," *IEEE Photonics J.*, vol. 8, no. 5, pp. 1–7, Oct. 2016.
[97] J. Perez and R. Llorente, "On the performance of a linearized dual parallel Mach–Zehnder electro-optic modulator," *Opt. Commun.*, vol. 318, pp. 212–215, May 2014.
[98] B. Masella, B. Hraimel, and X. Zhang, "Enhanced Spurious-Free Dynamic Range Using Mixed Polarization in Optical Single Sideband Mach–Zehnder Modulator," *J. Light. Technol.*, vol. 27, no. 15, pp. 3034–3041, Aug. 2009.
[99] S. Li, X. Zheng, H. Zhang, and B. Zhou, "Highly Linear Radio-Over-Fiber System Incorporating a Single-Drive Dual-Parallel Mach–Zehnder Modulator," *IEEE Photonics Technol. Lett.*, vol. 22, no. 24, pp. 1775–1777, Dec. 2010.
[100] J. Li, Y.-C. Zhang, S. Yu, T. Jiang, Q. Xie, and W. Gu, "Third-order intermodulation distortion elimination of microwave photonics link based on integrated dual-drive dual-parallel Mach–Zehnder modulator," *Opt. Lett.*, vol. 38, no. 21, pp. 4285–4287, Nov. 2013.
[101] Z. Li, H. Pan, H. Chen, A. Beling, and J. C. Campbell, "High-Saturation-Current Modified Uni-Traveling-Carrier Photodiode With Cliff Layer," *IEEE J. Quantum Electron.*, vol. 46, no. 5, pp. 626–632, May 2010.
[102] T. Jiang, R. Wu, S. Yu, D. Wang, and W. Gu, "A Novel High-Linearity Microwave Photonic Link Based on the Strategy of Adding a Compensation Path Using a Bidirectional Phase Modulator," *IEEE Photonics J.*, vol. 8, no. 5, pp. 1–7, Oct. 2016.
[103] B. M. Haas and T. E. Murphy, "A Simple, Linearized, Phase-Modulated Analog Optical Transmission System," *IEEE Photonics Technol. Lett.*, vol. 19, no. 10, pp. 729–731, May 2007.
[104] B. Masella and X. Zhang, "Linearized Optical Single-Sideband Mach–Zehnder Modulator for Radio-Over-Fiber Systems," *IEEE Photonics Technol. Lett.*, vol. 19, no. 24, pp. 2024–2026, Dec. 2007.
[105] Z. Zhu, S. Zhao, X. Li, K. Qu, T. Lin, and B. Lin, "Dynamic Range Improvement for an Analog Photonic Link Using an Integrated Electro-Optic Dual-Polarization Modulator," *IEEE Photonics J.*, vol. 8, no. 2, pp. 1–10, Apr. 2016.
[106] F. Wang, S. Shi, and D. W. Prather, "LTE Signal Transmission Over a Linearized Analog Photonic Link with High Fidelity," *IEEE Photonics J.*, pp. 1–1, 2019.
[107] Vincent J. Urick Jr., Jason D. Mckinney, Keith J. Williams, "External Intensity Modulation with Direct Detection," in *FUNDAMENTALS OF MICROWAVE PHOTONICS*, John Wiley & Sons, Ltd, 2015, pp. 212–272.
[108] E. I. Ackerman *et al.*, "Signal-to-Noise Performance of Two Analog Photonic Links Using Different Noise Reduction Techniques," in *2007 IEEE/MTT-S International Microwave Symposium*, 2007, pp. 51–54.
[109] "The FCC's 5G FAST Plan," *Federal Communications Commission*, 15-Sep-2016. [Online]. Available: https://www.fcc.gov/5G. [Accessed: 14-Jul-2019].

[110] T. Ozeki and E. H. Hara, “Measurement of nonlinear distortion in photodiodes,” *Electron. Lett.*, vol. 12, no. 3, pp. 80–81, Feb. 1976.
[111] T. Ohno, H. Fukano, Y. Muramoto, T. Ishibashi, T. Yoshimatsu, and Y. Doi, “Measurement of intermodulation distortion in a unitraveling-carrier refracting-facet photodiode and a p-i-n refracting-facet photodiode,” *IEEE Photonics Technol. Lett.*, vol. 14, no. 3, pp. 375–377, Mar. 2002.
[112] R. D. Esman and K. J. Williams, “Measurement of harmonic distortion in microwave photodetectors,” *IEEE Photonics Technol. Lett.*, vol. 2, no. 7, pp. 502–504, Jul. 1990.
[113] A. Ramaswamy *et al.*, “Experimental analysis of two measurement techniques to characterize photodiode linearity,” in *2009 International Topical Meeting on Microwave Photonics*, 2009, pp. 1–4.
[114] H. Pan, Z. Li, A. Beling, and J. C. Campbell, “Characterization of High-Linearity Modified Uni-Traveling Carrier Photodiodes Using Three-Tone and Bias Modulation Techniques,” *J. Light. Technol.*, vol. 28, no. 9, pp. 1316–1322, May 2010.
[115] Z. Li *et al.*, “High-power high-linearity flip-chip bonded modified uni-traveling carrier photodiode,” *Opt. Express*, vol. 19, no. 26, pp. B385–B390, Dec. 2011.
[116] Y. Fu, H. Pan, Z. Li, A. Beling, and J. C. Campbell, “Characterizing and Modeling Nonlinear Intermodulation Distortions in Modified Uni-Traveling Carrier Photodiodes,” *IEEE J. Quantum Electron.*, vol. 47, no. 10, pp. 1312–1319, Oct. 2011.
[117] A. Beling *et al.*, “Impact of voltage-dependent responsivity on photodiode non-linearity,” in *LEOS 2008 - 21st Annual Meeting of the IEEE Lasers and Electro-Optics Society*, 2008, pp. 157–158.

APPENDIX

PERMISSION

Title: Photonic Generation of High Fidelity RF Sources for Mobile Communications
Author: Fuquan Wang
Publication: Lightwave Technology, IEEE/OSA Journal of
Publisher: IEEE
Date: 15 Sept.15, 2017
Copyright © 2017, IEEE

LOGIN
If you're a copyright.com user, you can login to RightsLink using your copyright.com credentials.
Already **a RightsLink user** or want to learn more?

Thesis / Dissertation Reuse

The IEEE does not require individuals working on a thesis to obtain a formal reuse license, however, you may print out this statement to be used as a permission grant:

Requirements to be followed when using any portion (e.g., figure, graph, table, or textual material) of an IEEE copyrighted paper in a thesis:

1) In the case of textual material (e.g., using short quotes or referring to the work within these papers) users must give full credit to the original source (author, paper, publication) followed by the IEEE copyright line © 2011 IEEE.
2) In the case of illustrations or tabular material, we require that the copyright line © [Year of original publication] IEEE appear prominently with each reprinted figure and/or table.
3) If a substantial portion of the original paper is to be used, and if you are not the senior author, also obtain the senior author's approval.

Requirements to be followed when using an entire IEEE copyrighted paper in a thesis:

1) The following IEEE copyright/ credit notice should be placed prominently in the references: © [year of original publication] IEEE. Reprinted, with permission, from [author names, paper title, IEEE publication title, and month/year of publication]
2) Only the accepted version of an IEEE copyrighted paper can be used when posting the paper or your thesis on-line.
3) In placing the thesis on the author's university website, please display the following message in a prominent place on the website: In reference to IEEE copyrighted material which is used with permission in this thesis, the IEEE does not endorse any of [university/educational entity's name goes here]'s products or services. Internal or personal use of this material is permitted. If interested in reprinting/republishing IEEE copyrighted material for advertising or promotional purposes or for creating new collective works for resale or redistribution, please go to http://www.ieee.org/publications_standards/publications/rights/rights_link.html to learn how to obtain a License from RightsLink.

If applicable, University Microfilms and/or ProQuest Library, or the Archives of Canada may supply single copies of the dissertation.

BACK CLOSE WINDOW